Microscopic and Macroscopic Insights into Second Order Nonlinear Optics through Computational and Experimental Routes

by

Shyam Parshotam

A thesis submitted in partial fulfillment of the requirements for the degree of

Doctor of Philosophy

Department of Chemistry

University of Alberta

Abstract

The challenge with obtaining physical insights into physiochemical phenomena is connecting the macroscopic observables with the microscopic processes in a system. In second-order nonlinear optical spectroscopy, experimental techniques such as vibrational sum frequency generation (vSFG) and second harmonic generation (SHG) give a macroscopic picture of environmentally relevant interfaces such as the silica/water interface. Theory-based computations of the microscopic properties can provide valuable insights into the underlying characteristics giving rise to the macroscopic observations. However, when utilizing experimental and computational approaches, the challenge is that factors inherent to the system or measurement can influence the final results. Hence, this thesis focuses on understanding the influence of the excitation wavelength of light in computations of hyperpolarizabilities, the Fermi resonance in vSFG measurements, and the macroscopic and microscopic silica response in SHG studies.

On a microscopic scale, the first molecular hyperpolarizability strongly correlates to the intramolecular charge transfer in donor-acceptor systems. While numerous studies have highlighted the importance of modifying the system and solvation in computations, studying the excitation wavelength dependence is challenging due to the limited number of experimental studies. As such, by utilizing the charge transfer-dependent hyperpolarizability trend of the para, meta, and ortho nitroaniline isomers (pNA>oNA>mNA), the influence of the excitation wavelength can be elucidated. In non-resonant regions, with reference to CCSD/aug-cc-pVDZ and experimental studies, we find that some computational approaches do not consistently reproduce the nitroanilines' trend at specific excitation wavelengths. For example, range-separated hybrid functionals require optimal gap tuning to reproduce the trend. In resonant regions, we find that damped response theory predicts that the trend is maintained at the two-photon absorption but

breaks down near the one-photon pole. Compared to the two-state model, the undermined charge transfer characteristics at the one-photon pole can be due to the influence of other electronic states. Furthermore, the utility of optimal gap tuning of range-separated hybrid functionals is also dependent on the excitation wavelength.

On a macroscopic scale, vibrational sum frequency generation (vSFG) spectroscopy can provide information on the local hydrogen-bonding environment at the environmentally relevant silica/water interface. However, the inter and intramolecular vibrational coupling in water makes it difficult to decipher the environment from vibrational spectroscopy. As such, vSFG, electrokinetic measurements, and the maximum entropy method are used on isotopically diluted water (HOD) at the silica/aqueous interface to reveal the effects of vibrational coupling at the silica/water interface. In the Stern layer spectra, the frequency centers between H_2O and HOD shift at pH 2, signifying the presence of intermolecular coupling in the former that can be related to the double-donor hydrogen-bonded structure of water. Furthermore, the presence of intramolecular coupling in H_2O distorts the spectral response, as there are apparent differences in the evolution of the Stern layer. This behavior is further supported by the evolution of the HOD Stern layer spectra closely matching the pKa of the out-of-plane silanols predicted by previous ab initio molecular dynamic simulations.

Connecting the dots between the macroscopic observables to microscopic properties is a valuable approach to rationalizing experimental measurements. The challenge with second harmonic generation measurements at the silica/water interface is the contribution of both silica and water. As such, the silica contribution can be elucidated by combining SHG with previously measured zeta potential and vibrational sum frequency generation (vSFG) intensity measurements under conditions that promote charge inversion. The zeta potential and the vSFG measurements

follow a similar trend in these conditions, but SHG yields the opposite behaviour. This observation shows that silica exhibits a pH-dependent response to the SHG measurement, and interference between the silica and water responses can either be constructive or destructive depending on the net orientation of water molecules in the aqueous phase. On a microscopic level, the molecular hyperpolarizability of neutral and deprotonated silica clusters is computed with density functional theory (CAM-B3LYP/6-31+G(d,p)). We reveal a significant increase in hyperpolarizabilities upon the deprotonation of silanol sites. This change suggests that one potential source of the silica contribution to the SHG measurement is the deprotonation of surface silanol sites.

Preface

This thesis is an original work by Shyam Parshotam. All the research conducted in this thesis was done in the Brown and Gibbs research groups (Chemistry Department, University of Alberta).

Chapter 2 has been prepared for submission. I ran all the computations, analyzed the data, and am the primary author of the manuscript. Dr. Alex Brown and Dr. Julianne M. Gibbs are the supervisory authors.

A version of Chapter 3 is adapted from work published as S. Parshotam, B. Rehl, F. Busse, A. Brown, and J.M. Gibbs. *J. Phys. Chem. C*, 2022. Dr. Benjamin Rehl and Franziska Busse aided with the sum frequency generation and zeta potential measurements. Dr. Julianne M. Gibbs and Dr. Alex Brown are the supervisory authors.

Chapter 4 has been prepared for submission to *J. Phys. Chem. C.* Second harmonic generation measurements were done in collaboration with Dr. Wentong Zhang and are based on initial measurements by Dr. Akemi Darlington and Dr. Md Delwar Sikder. I ran all the computations, analyzed the data, and am the primary author of the manuscript. Dr. Wentong Zhang and Dr. Benjamin Rehl contributed editorially to this work. Dr. Julianne M. Gibbs and Dr. Alex Brown are the supervisory authors.

Not included in this thesis is collaborative work published as S. Parshotam, M. Joy, M. Rossano-Tapia, V. A. Mora-Gomez, and A. Brown. “The thermochemical, structural, and spectroscopic analyses of the tautomers of sulfur and selenium modified emissive nucleobases.” in *Canadian Journal of Chemistry,* 99(4), 390-396.

Acknowledgements

I have many people to thank for their support through graduate school. Firstly, I would like to thank my supervisors, Dr. Alex Brown and Dr. Julianne M. Gibbs, for their patience, mentorship, and guidance. I am also grateful to my supervisory committee, Dr. Arthur Mar and Dr. Wolfgang Jaeger, for all the advice through the years. I would also like to thank Dr. Yunjie Xu and Dr. Sylvie Roke for taking the time to review this thesis. I would also like to thank Dr. Mariusz Klobukowski and Dr. Gabriel Hanna.

I want to thank all my collaborators and mentors on the experimental and computational sides over the years. I am incredibly grateful to Ben and Mokhtar for showing me the right and wrong ways of laser spectroscopy. Hopefully, I can transfer this knowledge to Nathaniel. I am very much indebted to Maria and Arturo for the fantastic opportunity to work together and be Megan's WISEST mentor. I am grateful for the opportunity to work with Hansol, Franziska, and Eiman. Lastly, I would also like to thank Wentong, who braved the pandemic to work with us for a year. I am also grateful to all past and present (under) graduate students for their support, openness, and friendship. I would like to thank all the past and present Brown and Gibbs group members: Ryan, Nathanael, Ismael, Minh, Cuthbert, Mac, Ian, Nahida, Anantha, Tianli, Marlee, Santi, Anyeld, Sarah, Saf, Yuning, Melis, Yusuf, Antoine, Labanya, Zhibo, and Cat. A big thank you to the rec league soccer teams, most of all, Kwami (for roping me in), Trevor, and Mohammad. We made it to 2 finals and lost – the third time is a charm! I would also like to thank Craig, Guojie, Octavio, Arsh, Moe, Madhu, Vidyanshu, Dundappa, Felix, and Alex Gzyl for all the support. Last and most importantly, I would like to thank my family for all the continuous support and belief throughout the years.

Table of Contents

Abstract ii

Preface v

Acknowledgements vi

Table of Contents vii

List of Figures xii

List of Tables xx

List of Abbreviations and Acronyms xxi

List of Symbols xxiii

Chapter 1 1

1.1 Importance of the Silica/Water Interface 2

1.2 Studying the Silica/Water Interface 2

1.3 Nonlinear Optics 3

  1.3.1 Origins 4

  1.3.2 Second Order Process 6

  1.3.3 Microscopic and Macroscopic Relationship 8

1.4 Macroscopic Picture 9

  1.4.1 Charged Aqueous Interfaces 9

  1.4.2 Electrical Double Layer 10

  1.4.3 Characterizing the Electrical Double Layer 11

1.4.4 Polarization-Dependent Nonlinear Optical Spectroscopy 12
1.4.5 Nonresonant Second Harmonic Generation 14
1.4.6 Vibrational Sum Frequency Generation 23
1.5 Microscopic Picture 28
1.5.1 Importance of the Molecular Hyperpolarizability 28
1.5.2 Hyperpolarizability and Charge Transfer 29
1.5.3 Experimental Approaches for Determining the Hyperpolarizability 31
1.5.4 Computational Approaches 32
1.5.5 Density Functional Theory 35
1.5.6 Optimal Gap Tuning 37
1.6 Thesis Scope and Motivation 38
Chapter 2 40
2.1 Introduction 41
2.2 Methods 44
2.3 Results and Discussion 47
2.4 Conclusions 58
Chapter 3 59
3.1 Introduction 60
3.2 Methods 63
3.2.1 Materials 63
3.2.2 Sample Preparation 63

3.2.3 Laser Assembly 64

3.2.4 vSFG Experiments 65

3.2.5 Zeta Potential Experiments 66

3.2.6 Maximum Entropy Method Analysis 67

3.3 Results and Discussion 68

3.3.1 Homodyne vSFG and Zeta Potentials 68

3.3.2 Complex vSFG Spectra of HOD 75

3.3.3 Stern and Diffuse Layer Spectra 83

3.4 Conclusions 89

Chapter 4 91

4.1 Introduction 92

4.2 Methods 96

4.2.1 Materials 96

4.2.2 Sample Preparation 96

4.2.3 Second Harmonic Generation Set Up 96

4.2.4 Second Harmonic Generation Experiments 97

4.2.5 Computational Details 98

4.3 Results and Discussion 98

4.4 Conclusions 113

Chapter 5 115

5.1 Summary of Thesis 116

5.2 Future Work 118

References 122

Appendix A. 144

A1. Experimental Studies on Nitroaniline Isomers 145

A2. Optimal Gap Tuning of RSH Functionals 146

A3. Variation of the Hyperpolarizability for the Tuned RSH Functionals. 147

A4. TD-DFT Computations 148

A5. Damped Two State Model Versus Damped Response Theory 149

A6. Variation of the Hyperpolarizabilities of pNA and mNA with Respect to the Range Separation Parameter in the Gas Phase 150

A7. Variation of the Hyperpolarizabilities of pNA, oNA, and mNA with Respect to the Range Separation Parameter in 1,4 dioxane 151

A8. Coordinates of Ground State Geometries 152

Appendix B. 154

B1. Correction for Local Field Effects at the Silica/HOD Interface 155

B2. Ionic strength Dependent PPP spectra of H_2O and HOD 156

B3. Electrokinetic Charge Densities 156

B4. Error and True Phase from Phase Sensitive vSFG spectra 157

B5. Prediction of the Complex Spectra of HOD Over the Ionic Strength. 158

B6. Real Component of HOD Determined by MEM Analysis 160

B7. Determination of the Diffuse and Stern Layer Spectra 160

Appendix C. 163

C1. pH Dependent vSFG Measurements and Spectral Fits 164

C2. Constant Silica Response Scenarios 164

C3. Coordinates for Ground State Geometries for the Models 165

C4. Hyperpolarizability Computations 166

List of Figures

Figure 1.1: Illustration of the hyperpolarizability or second-order nonlinear optical susceptibility tensor. Both properties are rank three tensors with 27 elements. 7

Figure 1.2: Transformation of the molecular hyperpolarizability determined in the molecular frame (*abc*) to the laboratory frame (*ijk*). 8

Figure 1.3: The electrical double layer model at a negatively charged silica/water interface, where OHP refers to the outer Helmholtz plane. Image adapted from Gibbs and coworkers.[44] Copyright 2022, American Chemical Society. 10

Figure 1.4: (a) Polarization combinations in the reflective experimental geometry and (b) indicating the SSP polarization. The axis system is arbitrarily drawn. 13

Figure 1.5: (a) Energy level diagram and (b) experimental setup for SHG measurements......... 14

Figure 1.6: SHG measurements done at the silica/water interface in the presence of 500 mM NaCl. The solid line is used to guide the eye. Data was reproduced from Eisenthal and coworkers.[41] Copyright 1992, with permission from Elsevier. 16

Figure 1.7: (a) Wavevectors at the silica/water interface (note: reflected beams not shown). Figure adapted from Roke and coworkers.[63] Copyright 2016 American Chemical Society........ 17

Figure 1.8: Previous SHG measurements at the alumina/water interfaces, with intensity normalized to the value at the point of zero charge reported. Dashed lines indicate the pH of the point of zero charge reported in each of these studies. The solid lines represent the values predicted by the model proposed by Eisenthal and coworkers.[41] Copyright 1992, with permission from Elsevier. 19

Figure 1.9: (a) Energy level diagram and (b) experimental setup for vibrational sum frequency generation.. 23

Figure 1.10: (a) vSFG spectra indicating the presence and absence of the Fermi resonance at the silica/water and silica/HOD interfaces, respectively. (b) Energy level diagram depicting the Fermi resonance process. Here ν_1 and δ_2 refer to the symmetric stretch and bend modes respectively. 27

Figure 1.11: Structures of para, ortho, and meta-nitroaniline along with their corresponding resonance structures. Parts of the figure are adapted from Levine.[113] Copyright 1976, with permission from Elsevier. 30

Figure 1.12: Six permutations of the excitations accounted by the sum over states approach. Figure adapted from Boyd.[12] Copyright 2020, with permission from Elsevier........ 33

Figure 2.1: Structures of the nitroaniline isomers: para-nitroaniline (pNA), ortho-nitroaniline (oNA), and meta-nitroaniline (mNA). 44

Figure 2.2: (a) Variation of the hyperpolarizability of pNA as a function of the excitation wavelength for all RSH functionals in comparison to experimental values.[179] Computations were done in 1,4 dioxane. Gas phase (b-d) logarithmic hyperpolarizability values of all isomers in a broader wavelength range from 1907 nm to the static limit. Additional gas phase CCSD/aug-cc-pVDZ computations on pNA from Sałek et al.[183] are presented too. 52

Figure 2.3: Hyperpolarizabilities determined using the (a) damped two-state model (TSM) and (b) damped response theory (RT). The value of the relaxation parameter is set to 500 cm^{-1} for both approaches. All computations are done with CAM-B3LYP/6-311+G(d,p) in the gas phase. 54

Figure 2.4: Variation of the hyperpolarizabilities of oNA with respect to the range separation parameter for RSH functionals at (a) the static limit (b) 1064 nm, and (c) 1907 nm in the gas phase. All computations used the 6-311+G(d,p) basis set. 57

Figure 3.1: Overview of the optical set up for the measurement of vibrational sum frequency generation spectra at silica/aqueous interface. 65

Figure 3.2: Representative SSP vSFG intensity spectra corrected for local field effects from 2850 to 3750 cm^{-1} at the (a) silica/HOD and (b) silica/H_2O interfaces[44] as the pH was varied from 10 to 2 with under a 50 mM NaCl background electrolyte. Representative PPP vSFG intensity spectra without local field corrections at the (c) silica/HOD and (d) silica/H_2O interfaces. To allow for comparison to previous work,[92] we also separately measured the SSP and PPP spectra at the pH 12 silica/HOD interface. 70

Figure 3.3: The square root of the average values of the integrated SSP (local field-corrected) and PPP spectra from 2850 to 3750 cm^{-1} (blue), normalized to the value at pH 10, and the corresponding zeta potentials (red) at the (a) silica/HOD and (b) silica/H_2O[44] interfaces collected from pH 10 to 2 with a background of 50 mM NaCl. Error bars are the standard deviation from replicate measurements. 72

Figure 3.4: Representative SSP vSFG intensity spectra corrected for local field effects from 2850 to 3750 cm^{-1} and the accompanying average square root of the integrated spectral areas (blue squares) and average zeta potentials (red circles) at the (a-b) silica/HOD and (c-d) silica/H_2O interfaces collected from the neat (no added salt) solution to an ionic strength of 50 mM NaCl. Error bars are from the standard deviation of replicate measurements. 74

Figure 3.5: Complex spectra of the HOD-D_2O system. (a) The wave-number dependent error phase was extracted from Myalitsin et al.[78] (bold lines) and interpolated values at intermittent pH (dashed). (b) Comparison of the imaginary spectra at pH 2 and pH 12 measured by Myalitsin et al.[78] and those determined by the maximum entropy method analysis of our HOD-D_2O SF

intensity spectra. (c) The imaginary spectra using the interpolated error phases and MEM analysis of our intensity spectra are presented in Figure 3.2(a). 78

Figure 3.6: (a) The MEM phase of Myalitsin et al.[78] (green triangles) determined from the MEM analysis of their corresponding intensity spectrum. The red squares show the 3 predicted values of the absolute phase derived from the MEM phase of Myalitsin et al.[78] (b)The absolute phase (red line) determined from the linear fit of the 3 predicted values (red squares) in comparison to that of Myalitsin et al.[78] (peach circles). (c) Comparison of the predicted complex spectrum using the absolute phase linear fit to that reported by Myalitsin et al.[78] 80

Figure 3.7: (a) The absolute phase determined from the reference complex spectrum of Myalitsin et al.[78] (peach line) and that determined from the MEM phase of our measured intensity spectrum (red squares). The linear fit of the three data points (red squares) was used as the wavenumber-dependent error phase in our analysis for this set of experimental conditions. (b) The real (red) and imaginary (blue) spectra of 10 mM NaCl HOD at natural pH, which are similar to the HD-SFG measurements of the silica/HOD interface with 10 mM phosphate buffer at pH 7. (c) Imaginary spectra over the ionic strength range of neat HOD to 50 mM NaCl using the calculated frequency-dependent error phase for each salt concentration and MEM analysis of the corresponding intensity spectra. 82

Figure 3.8: The complex $\chi^{(3)}$ spectrum of the silica/HOD interface. The reported complex spectrum is the average from analyzing replicate SFG measurements. Shaded areas represent the error bars propagated from the zeta potential measurements. 83

Figure 3.9: (a) Diffuse layer and (b) Stern layer spectra of HOD and H_2O over the pH range of 10 to 2 at 50 mM NaCl. The H_2O spectra were reported in our previous work (Rehl et al.[44]). An additional measurement at pH 12 is also included to allow for comparison with rescaled

measurements at pH 12 and 2 M by Urashima et al.[92] Shaded areas represent the uncertainty propagated from the zeta potential measurements. 85

Figure 4.1: Optical set up for the measurement of second harmonic generation at the silica/water interface... 97

Figure 4.2: (a) Diagram of the electric potential decay in the electrical double layer in the presence of 100 mM NaCl.[45,83] (b) Representative zeta potential performed at the silica interface in the presence of 100 mM NaCl. (c) The square root of the integrated ppp-SFG intensities from 2900 to 3600 cm^{-1} from a representative experiment at the silica interface in the presence of 100 mM NaCl. (d) The square root of SHG intensity of a representative experiment at the silica interface in the presence of 100 mM NaCl. Both vSFG and SHG intensities are normalized to the initial point. Standard deviations are represented by the shaded region in (b) and (d).............. 100

Figure 4.3: (a) Diagram of the electric potential decay in the electrical double layer in the presence of 100 mM $CaCl_2$ under conditions of overcharging (> pH 10).[45,83] (b) Representative zeta potential (ζ) performed at the silica interface in the presence of 100 mM $CaCl_2$ with 10 mM NaCl as background electrolyte. (c) The square root of the integrated ppp-SFG intensities from 2900 to 3600 cm^{-1} from a representative experiment at the silica interface in the presence of 100 mM $CaCl_2$ with 10 mM NaCl. (d) The square root of SHG intensity of a representative experiment at the silica interface in the presence of 100 mM $CaCl_2$ with 10 mM NaCl. Both vSFG and SHG intensities are normalized to the initial point. Standard deviations are represented by the shaded region in (b) and (d). 103

Figure 4.4: Two scenarios illustrating (a) constructive or (b) destructive interference between the total second nonlinear susceptibility contributions in the aqueous phase (green) and silica (yellow) from neutral to high pH in the presence of 100 mM NaCl. The total (red) is the sum of

these two contributions, where the magnitude is proportional to the square root of the SHG intensity. The direction of the arrow is drawn arbitrarily to a relative scale, and they represent instances where there is constructive (same arrow direction) or destructive (opposite arrow direction) interference. A water molecule is drawn to indicate the average orientation based on spectral fitting.[275] 105

Figure 4.5: Possible scenarios moving from (a) constructive to destructive or (b) destructive to constructive interference of the total second nonlinear susceptibility contributions in the aqueous phase (green), silica (yellow), and the total (red) from neutral to high pH in the presence of 100 mM $CaCl_2$. The measured square root of the SHG intensity is consistent with the scenario in (a). 108

Figure 4.6: Protonated (neutral) and deprotonated (anionic) silica models, (a) orthosilicic acid structure (Model 1), (b) model based on Hassanali and Singer (Model 2),[285] and (c) truncated structure from the surface model proposed by Ugliengo et al.(Model 3).[277] The blue arrow from the center of mass indicates the direction of the dipole moment, while the black arrow indicates the z-axis. 111

Figure A1: Absolute differences of J^2, see Equation 1 in the main text, against the range separation parameter used to determine the optimized ω values. All results were determined in the gas phase with the 6-311+G (d,p) basis set. 147

Figure A2: Variation of hyperpolarizabilities with respect to the excitation wavelengths for tuned RSH functionals (a) at excitation wavelengths and 1,4 dioxane,[179] and (b)-(d) over a broader excitation wavelength window in the gas phase. All results were determined with the 6-311+G (d,p) basis set. Previous CCSD/aug-cc-pVDZ computations on pNA are also presented.[183] 147

Figure A3: Hyperpolarizabilities of nitroaniline isomers computed with damped two-state model and damped response theory (damping parameter= 500 cm^{-1}). All results were determined with the CAM-B3LYP/6-311+G (d,p) in the gas phase. Dashed lines indicate pole positions.......... 149

Figure A4: Variation of hyperpolarizabilities, of pNA and mNA with respect to the range separation parameter for RSH functionals at (a) the static limit (b) 1064 nm, and (c) 1907 nm computed in the gas phase. All results were determined in the gas phase with the 6-311+G (d,p) basis set. 150

Figure A5: Variation of the hyperpolarizabilities of the nitroaniline isomers with respect to the range separation parameter for RSH functionals at (a-c) the static limit (d-f) 1064 nm, and (g-i) 1907 nm in 1,4 dioxane. All results were determined with the 6-311+G (d,p) basis set........... 151

Figure B1: Representative vSFG spectra of the silica/HOD interface with varying (a and c) ionic strength and (b and d) pH: (a and b) before and (c and d) after local field corrections. The spectra are normalized to the intensity at 3200 cm^{-1} measured at the silica/10 mM NaCl water interface for the same sample on the same day.. 156

Figure B2: Representative PPP intensity spectra of (a) H_2O and (b) HOD in D_2O collected as the ionic strength was varied. 156

Figure B3: Electrokinetic charge densities computed with the Grahame equation for the silica/H_2O and HOD as a function of (a) ionic strength and (b) pH with a background salt concentration of 50 mM NaCl. The asterisk (*) in (a) indicates the electrokinetic charge density in the presence of 50 mM NaCl, where we observed intrinsic differences in the natural pH. Specifically, we measured a pH of ~7.12 (after the 0.32 adjustment) for HOD with 50 mM NaCl and a pH of ~5.7 for H_2O with 50 mM NaCl. We tentatively attribute this difference to the differences in all the equilibrium constants that influence the pH (Henry's constant of CO_2 in H_2O vs D_2O, formation of carbonic acid in H_2O vs D_2O, K_{a1} and K_{a2} of H_2CO_3 and D_2CO_3). . 156

Figure B4: (a) Error and (b) true or absolute phase (φ) derived from the phase sensitive vSFG spectra reported by Myalitsin et al.[78] at natural pH (neat~pH 7.5) and pH 7 (10 mM phosphate buffer solution). The error phase was determined by performing MEM analysis on their corresponding intensity spectra and subtracting the resultant MEM phase from the absolute phase (φ) determined from their complex spectra. 157

Figure B5: Representative MEM phase and predicted absolute phase over a varied ionic strength range. 158

Figure B6: Representative (a) intercept (b) slope (c) predicted absolute phase (φ) (d) error phase over the ionic strength range. 159

Figure B7: The representative real spectra over the (a) ionic strength and (b) pH ranges covered in this work. 160

Figure B8: Comparison of the imaginary component of the (a) diffuse and (b) Stern layer resulting from our total complex spectra and our $\chi^{(3)}$ complex spectra at pH 12 compared with the HOD and H_2O spectra reported by Urashima et al.[92] 161

Figure C1: (a) Spectra presented by Rashwan et al.[275] and (b) the corresponding amplitude determined by spectral fitting. 164

Figure C2: Two scenarios (a) Constructive interference and (b) destructive interference when considering a constant silica contribution in the presence of 100 mM $CaCl_2$ in the aqueous phase. Both scenarios cannot account for the pH-dependent trends observed in the presence of 100 mM $CaCl_2$. 165

List of Tables

Table 1.1: Different types of linear and nonlinear optical processes along with their orders with respect to the electric fields, and frequencies (ω) of the incident and nonlinear light generated... 4

Table 1.2: Elements of the second order nonlinear susceptibility probed by the different experimental polarization configurations. 13

Table 2.1: Gas phase static and dynamic hyperpolarizabilities (in au) of the nitroaniline isomers computed with DFT functionals and wave function theory-based methods with 6-311+G(d,p) and aug-cc-pVDZ basis sets, respectively. Optimally tuned RSH functionals are distinguished by an asterisk (*). 48

Table 2.2: Dynamic hyperpolarizabilities (in au) with excitation wavelength = 1064 nm and 1907 nm of the nitroaniline isomers computed with the default DFT functionals and optimally tuned functionals (distinguished by an asterisk (*)). 50

Table A1: Experimental hyperpolarizability values of the nitroaniline isomers at various excitation wavelengths (in nm) and in different solvents. 145

Table A2: Energies (E) in nm with values in parenthesis given in eV and oscillator strengths (f) for the first three excited states of the nitroaniline isomers calculated with different functionals and the 6-311+G(d,p) basis set in the gas phase. Values correspond to the untuned RSH functionals. 148

Table A3: Energies, transition dipole moment, excited and ground state dipole moments in au, computed with CAM-B3LYP/6-311+G(d,p) in the gas phase. 148

Table C1: Hyperpolarizability parameters (in atomic units) computed with CAM-B3LYP/6-31+G(d,p) in the gas phase for the neutral and anionic species shown in Figure 4.6. The hyperpolarizability ratio of anion/neutral is also given. 166

List of Abbreviations and Acronyms

a.u.	Arbitrary units
AFM	Atomic force microscopy
AU	Atomic units
B3LYP	Becke, three-parameter, Lee-Yang-Parr hybrid functional
CAM-B3LYP	Coulomb-attenuating method with the B3LYP functional
CAS	Complete active space
CC2	Second-order coupled cluster
CCS	Coupled cluster with singles excitation
CCSD	Coupled cluster with singles and doubles excitation
DFT	Density functional theory
DZP	Double zeta with polarization functions basis set
EDL	Electrical double layer
EFISH	Electric field induced second harmonic generation
GGA	Generalized gradient approximation
HD-SFG	Heterodyne sum frequency generation
HD-SHG	Heterodyne second harmonic generation
HF	Hartree Fock theory
HOMO	Highest occupied molecular orbital
HRS	Hyper Rayleigh scattering
IEF-PCM	Integral equation formalism variant of PCM
Iops	Internal options
LC-BLYP	Long-range corrected Becke Lee Yang Parr functional

LUMO	Lowest unoccupied molecular orbital
MD-DFT	Ab initio molecular dynamics based on DFT
MEM	Maximum entropy method
mNA	Meta nitroaniline
MP2	Second-order Møller Plesset perturbation theory
Nd-YAG	Neodymium-doped yttrium aluminium garnet
NLO	Nonlinear optics
OHP	Outer Helmholtz plane
oNA	Ortho nitroaniline
PCM	Polarizable continuum model
pNA	para nitroaniline
PPP	Polarization geometry of SF(P), visible(P), and IR(P)
RSH	Range separated hybrid functional
RT	Response Theory
SHG	Second harmonic generation
SOS	Sum over states
SSP	Polarization geometry of SF(S), visible(S), and IR(P)
Ti: Sapphire	Titanium sapphire oscillator
TDDFT	Time-dependent DFT
TSM	Two state model
vSFG	Vibrational sum frequency generation
ωB97XD	Range-separated version of Becke's 97 functional with dispersion correction
ωB97	Range-separated version of Becke's 97 functional

List of Symbols

J^2	Absolute error
A	Cross-sectional area of the channel
γ	Damping parameter
ε	Dielectric constant
E	Electric field
ω_{SHG}	Excitation wavelength
L	Length of channel
β	Molecular hyperpolarizability
μ_o	Permanent dipole moment
α	Polarizability
ω	Range separation parameter
γ_{ijkl}	Second hyperpolarizability
$\chi^{(n)}$	Nth-order nonlinear susceptibility
h	Spectral entropy
φ	True or actual phase
ε_o	Vacuum of permittivity
η	Viscosity
ζ	Zeta potential

Chapter 1

Introduction

1.1 Importance of the Silica/Water Interface

Silica or silicon dioxide is one of the most abundant mineral oxides on the planet, with almost 90% of all minerals in the Earth's crust being silicates.[1,2] This abundance of silica intertwines it with many aspects of technology,[3] biology,[4] and the environment.[5] In these settings, the interactions between silica and water play a crucial role in modulating the underlying geological, chemical, and physical processes such as weathering, dissolution, and ion adsorption. Understanding such processes through studying the silica/water interface is critical in creating new technologies and sustainable solutions.

An example where studies on the silica/water interface would be valuable can be found in the case of the oil-sand mining operations in Alberta, Canada. These operations involve surface mining that generates a waste mixture of water, silica, bitumen, and clay minerals.[6] The treatment of this waste involves the separation of water from this mixture. However, the separation will take decades to occur naturally, leading to the accumulation of waste and the risk of contamination. The challenge of developing a sustainable solution arises due to the complexity associated with the surface chemistry of the different components in the mixture.[7] As such, studying two of the principal components (silica and water) can aid in developing an understanding of the surface chemistry involved in this waste and thereby lead to sustainable treatment solutions.

1.2 Studying the Silica/Water Interface

Several computational and experimental approaches can be used to study the silica/water interface. Some experimental techniques include atomic force microscopy,[8] X-ray photoelectron and reflectivity spectroscopies,[9,10] and electrokinetic measurements.[11] Each technique probes different properties, which can give a macroscopic picture of the silica/water interface and be the basis of a molecular or microscopic interpretation. However, obtaining such interpretations can be non-trivial in complex systems with numerous forces at play. In such cases, computational approaches such as classical or ab initio molecular dynamics and electronic structure computations can aid in developing a microscopic (molecular) picture of the processes taking place. Such computations can give properties such as the radial distribution function, molecular polarizabilities, and transition dipole moments among others. These molecular properties can then be used to rationalize the macroscopic measurements.

In this context, nonlinear optical spectroscopy is a unique technique that can provide a macroscopic and microscopic picture. Experimentally, in nonlinear optical spectroscopy, there is a high degree of sensitivity to both the structure and electrostatics at the silica/water interface. On the other hand, the development and implementation of the theory behind the nonlinear processes permit the use of computational approaches to give a microscopic picture of the origin of the nonlinear optical response.

1.3 Nonlinear Optics

Before examining how nonlinear optical processes are applied at the macroscopic and microscopic scale, one must consider why these processes exist. Light with relatively weak electric fields can interact linearly with a molecule or medium. For example, in absorption or emission, input (incident) and output are the same frequency of light (ω). However, in nonlinear optics, sufficiently intense light with relatively strong electric fields interacts with a molecule or medium, bringing about optical nonlinearity.[12,13] These processes result in the generation of output light with a different frequency.

While the possibility of nonlinear optical phenomena was predicted by early theoretical studies by Maria Goeppert-Mayer, with two-photon absorption,[14] the experimental evidence of this phenomenon was only observed after the discovery and development of the first laser in the 1960s.[15] Specifically, the work of Franken et al.[16] found that the inclusion of sufficiently strong electric fields with a frequency of ω could induce remarkable frequency doubling (2ω) in quartz (referred to as second harmonic generation). Indeed, following this initial experiment, other nonlinear optical processes were discovered with different numbers of incident electric fields of light. Some examples of these processes are presented in Table 1.1.

Table 1.1: Different types of linear and nonlinear optical processes along with their orders with respect to the electric fields and frequencies (ω) of the incident and nonlinear light generated.

Process	**Order**	$-\boldsymbol{\omega_i}; \boldsymbol{\omega_1}, \ldots, \boldsymbol{\omega_n}$
Linear absorption/emission and refractive index	1	$-\omega; \omega$
Second harmonic generation (SHG)	2	$-2\omega_1; \omega_1, \omega_1$
Sum frequency generation (SFG)	2	$-\omega_3; \omega_2, \omega_1$
Third harmonic generation (THG)	3	$-3\omega_1; \omega_1, \omega_1, \omega_1$
dc-field-induced-second harmonic generation (EFISH)	3	$-\omega_3; \omega_2, \omega_1, 0$
Two-photon absorption	3	$-\omega_4; -\omega_3, \omega_2, \omega_1$

Depending on the number of electric fields of light involved, an order can be assigned to the nonlinear optical process. For example, second harmonic generation is a second order process due to two electric fields, whereas third harmonic generation is a third-order process since there are three electric fields.

1.3.1 Origins

To understand how these nonlinear optical processes arise, we must consider the interaction of the electric field of light and matter. A simplified picture would involve the incident light waves' oscillating electric field interacting with the molecule's electron density or the dipole moments in a medium. As the electric field varies sinusoidally, this results in the electron density and hence electric dipoles oscillating in response to the electric field of light. The oscillation frequency depends on the order of the nonlinear optical process. For example, in second-order processes, the polarization will oscillate at the sum of the frequencies of the two-incident oscillating electric fields ($\omega_3 = \omega_1 + \omega_2$).

The polarization of the electron density by the electric field (E) can be expressed as a Taylor series expansion under the electric dipole approximation. Within this approximation, polarized electron density can be represented by the induced dipole moment, μ_i, which can be expressed as

$$\mu_i = \mu_i^0 + \sum_j \alpha_{ij} E_j + \sum_{jk} \beta_{ijk} E_j E_k + \sum_{jkl} \gamma_{ijkl} E_j E_k E_l + \ldots \quad . \tag{1.1}$$

Here, μ_i^0 is the permanent static dipole moment and represents the scenario where the molecule is not interacting with the electric field of light (E). However, when the molecule begins to interact with the electric field of light, different processes begin to take place, and the first-order polarizability tensor characterizes the efficiency of these processes (α_{ij}), hyperpolarizability tensor (β_{ijk}), and second hyperpolarizability tensor (γ_{ijkl}). On a physical level, each of these terms represents the degree to which the molecule's electron density will oscillate when it interacts with the electric field of light. Since the oscillation of the electron density will be based on the molecule's axis, the indices '$ijkl$' represent the axes in the molecular principal axis frame.

On the other hand, in a macroscopic medium, one needs to account for the interaction of the light with electric dipoles per unit volume, i.e., the polarization of dipole moments that the electric field induces. The polarization (P) induced by the interaction of the electric field (E) of the incident light[12] is written as the following

$$P = \epsilon_o(\chi_i^{(1)}E_j + \sum_{jk}\chi_{ijk}^{(2)}E_jE_k + \sum_{jkl}\chi_{ijkl}^{(3)}E_jE_kE_l + \ldots) \tag{1.2}$$

In Equation 1.2, $\chi_i^{(1)}$ is the linear susceptibility of the medium, and $\chi_{ijk}^{(2)}$ and $\chi_{ijkl}^{(3)}$ are nonlinear susceptibilities of the medium. Similar to the microscopic representation, the nonlinear susceptibilities govern the efficiency of the process and can be thought of as the degree to which the dipole moments per unit volume (polarization) oscillate in response to the electric field.

As noted in Equations 1.1 and 1.2, the strength of the incident electric field of light plays a vital role in the medium displaying nonlinear behavior. The strength of the field needs to be sufficient to disturb the internal electric field generated by charged particles in the medium (~3×10^{10} Vm^{-1}).[13] Such field strengths can only be obtained from a laser source, hence the experimental observations after developing the first laser.

1.3.2 Second Order Process

While several techniques are based on higher-order nonlinear optical processes such as two-photon absorption[17] or third harmonic generation,[18] second-order nonlinear optical processes are attractive to use in different applications due to their symmetry restrictions.[19,20] These symmetry restrictions are the result of the nature of the nonlinear optical properties, i.e., molecular hyperpolarizability (β) in the microscopic frame and second-order nonlinear susceptibility ($\chi^{(2)}$) in the macroscopic frame. Both properties are rank three tensors with 27 independent elements or components in a 9×3 matrix. A rank three tensor can be visualized as a cube, as shown in Figure 1.1.

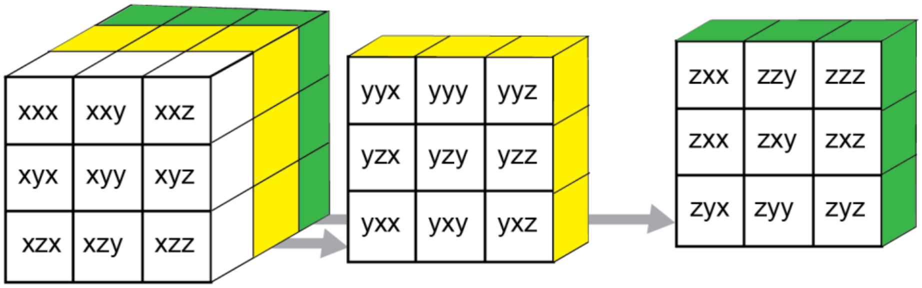

Figure 1.1: Illustration of the hyperpolarizability or second-order nonlinear optical susceptibility tensor. Both properties are rank three tensors with 27 elements.

Symmetry restrictions govern the number of independent elements. There are three symmetry restrictions: intrinsic permutational symmetry, time reversal, and spatial symmetry, with the first two being underlying aspects of the β_{ijk} and $\chi^{(2)}$ terms, whereas the last is dependent on the system. Intrinsic permutation symmetry requires the second-order properties to be unchanged when the last two Cartesian indices and incident frequencies are interchanged. For example, this symmetry requires:

$$\beta_{ijk} = \beta_{ikj}. \tag{1.3}$$

Moreover, as such, the number of independent elements is reduced to 18. The time-reversal symmetry, also known as Kleinman symmetry[21] arises in off-resonance studies and results in the interchangeability of all the Cartesian indices, i.e.,

$$\beta_{ijk} = \beta_{jki}. \tag{1.4}$$

The symmetry results in the reduction of the tensor elements from 18 to 10. The last symmetry to consider is the spatial symmetry of the system. The symmetry of the microscopic or macroscopic system dictates the number of independent components of the second-order properties that will be present. The most important outcome of spatial symmetry is that second-order processes do not occur in centrosymmetric environments. Such restrictions give second-order processes extremely high selectivity and sensitivity to noncentrosymmetric environments like those presented at an interface.

1.3.3 Microscopic and Macroscopic Relationship

Connecting the dots from the microscopic to the macroscopic view permits using computations in conjunction with experiments. The molecular hyperpolarizability computed can be related to the second-order nonlinear susceptibility by projecting the molecular axes (*abc*) onto the laboratory axes' frame (*ijk*).[22] In such a scenario, one needs to consider the tilt angle (θ), in-plane rotation (ϕ), and twist (ψ) angles as shown in Figure 1.2.

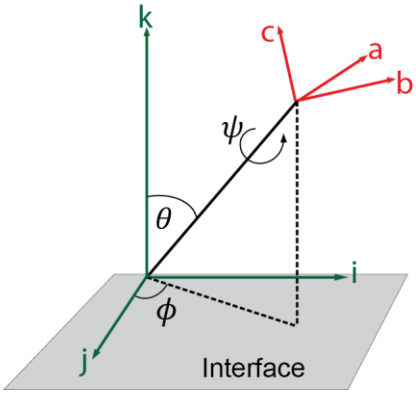

Figure 1.2: Transformation of the molecular hyperpolarizability determined in the molecular frame (*abc*) to the laboratory frame (*ijk*).

By using the rotation matrix, D, the hyperpolarizability in the molecular axes (*abc*) can be projected onto the laboratory axes (*ijk*),

$$\beta_{ijk}^{(2)}(\theta,\phi,\psi) \;=\; \sum_a \sum_b \sum_c D_{ia}(\theta,\phi,\psi) D_{jb}(\theta,\phi,) D_{kc}(\theta,\phi,\psi)\, \beta_{abc}^{(2)}. \tag{1.5}$$

Even though the hyperpolarizability is projected in the laboratory frame, one needs to consider the average response over an orientational distribution since multiple molecules will be per unit volume. The latter is determined from an orientation distribution function $f(\theta,\phi,\psi)$, such that average orientational hyperpolarizability $\langle\beta_{ijk}\rangle$ is given by

$$\langle \beta_{ijk} \rangle = \int_0^{2\pi} \int_0^{2\pi} \int_0^{\pi} f(\theta, \phi, \psi)\, \beta_{ijk} \sin\theta \,\partial\theta \,\partial\phi \,\partial\psi. \tag{1.6}$$

The average orientational hyperpolarizability can then be related to the second-order nonlinear susceptibility by considering the response over N molecules and the dielectric constant of the medium (ε_0), resulting in

$$\chi_{ijk}^{(2)} = \frac{N}{\varepsilon_0} \langle \beta_{ijk} \rangle. \tag{1.7}$$

1.4 Macroscopic Picture

Second order nonlinear optical spectroscopy provides valuable insights into various phenomena at interfaces due to the unique symmetry properties that make it highly surface sensitive. Since the first observations on a calcite surface,[23] these approaches have extended to various surfaces yielding powerful physical insights into the properties and behaviour of the processes.[24–30] Before going into detail on how nonlinear optical spectroscopy can be used, it is essential to understand how charged interfaces such as the silica/water interface are modeled.

1.4.1 Charged Aqueous Interfaces

When a charged substrate comes into contact with an aqueous solution, the region formed between them is referred to as a *buried surface* or an *interfacial region.* Various significant phenomena such as mineral reactivity,[31,32] dissolution,[33] pollutant transport,[34] surface defects,[35] protein folding,[36] bond formation,[37–39] and specific ion effects[8,40] all occur in the vicinity of the interfacial region.

While these phenomena occur at various charged interfaces in nature and modern technology, the silica/water interface represents one of the earliest studied and prototypical interfaces.[41,42] Owing to the natural abundance of silica in the environment, understanding the processes that occur can be of geochemical relevance.[1] Furthermore, models governing fundamental properties like structure and electrostatics can be developed and extended to predict the behaviour of other charged interfaces.

1.4.2 Electrical Double Layer

One model describing the interfacial region found at charged aqueous interfaces is the electrical double layer (EDL). When considering the silica/water interface, silica becomes negatively charged above the point of zero charge (pH 2).[43] As a result, an electric field is formed, which is characterized by the surface charge density and the surface potential (Φ_0) in the EDL. The potential linearly decays in one region (Stern layer) and exponentially decays in another region (diffuse layer). The point at which the electrical potential decays by 1/e is referred to as the Debye length ($1/\kappa$).

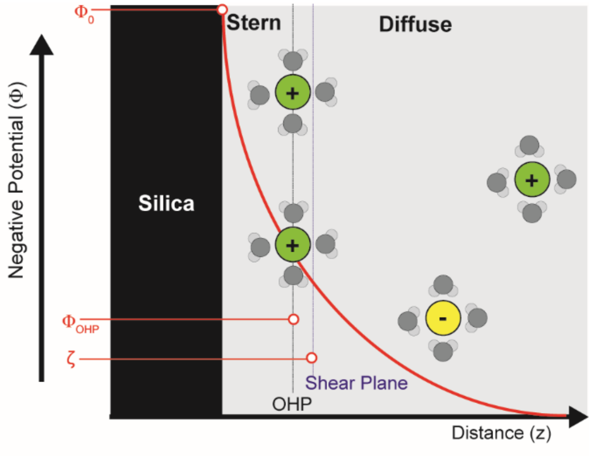

Figure 1.3: The electrical double layer model at a negatively charged silica/water interface, where OHP refers to the outer Helmholtz plane. Image adapted from Gibbs and coworkers.[44] Copyright 2022, American Chemical Society.

In the absence of direct surface binding, the positively charged ions in the aqueous phase accumulate at the outer Helmholtz plane (OHP) to counteract the surface charge. The electrical potential at the OHP is referred to as the outer Helmholtz potential (Φ_{OHP}). Near this plane is the shear plane, and the potential at the shear plane is referred to as the zeta potential (ζ), and the approximation that is often used is $\Phi_{OHP} \approx \zeta$. The zeta potential can be experimentally determined using electrophoretic or streaming current measurements.

The charge density present at the shear plane is often referred to as the electrokinetic charge density (σ_{ek}). When utilizing the zeta potential, σ_{ek} is computed with the Grahame equation[45] which is given by

$$\sigma_{ek} = \sqrt{8000RT\varepsilon\varepsilon_0 C}\, sinh\left(\frac{zF\zeta}{2RT}\right). \tag{1.8}$$

Here R is the gas constant, T is the temperature, ε is the dielectric constant, ε_0 is the permittivity of free space, C is the ionic strength, z is the charge of the counter ion, and F is Faraday's constant.

1.4.3 Characterizing the Electrical Double Layer

The challenge with characterizing the interfacial region is that conventional techniques are sensitive to contributions from the bulk solution. As a result, several techniques have been established to characterize different aspects of the electrical double layer. Information about the electrical properties of the EDL at the silica/water interface can be determined with atomic force microscopy,[8] electrokinetic measurements,[11,46] potentiometric titrations,[47] and X-ray photoelectron spectroscopy.[9,48,49] Absorption and structural information can be determined by X-ray reflectivity spectroscopy [10] and calorimetric studies.[50]

It should be noted that many of these techniques are designed to be applied to particle-based systems (silica colloids) due to the high surface areas, which in principle, can give a more significant response. Hence, studying the electrical properties and structure of substrates with smaller surface areas, such as planar silica, presents a challenge for these techniques. In this context, nonlinear optical spectroscopy can uniquely provide information on the structure and electrical properties at the planar silica/water interface.

1.4.4 Polarization-Dependent Nonlinear Optical Spectroscopy

Over the last 30 years, vibrational sum frequency generation (vSFG) and nonresonant second harmonic generation (SHG) have been developed to improve insights into the processes at various interfaces.[30,51,52] The underlying sensitivity of both techniques occurs due to the unique selection rule requiring a non-centrosymmetric (no inversion symmetry) environment that allows for the characterization of the interfaces. As noted previously, these processes are dependent on the second order nonlinear susceptibility ($\chi_{ijk}^{(2)}$),

$$P^{(2)} = \sum_{ijk} \chi_{ijk}^{(2)} E_j E_k. \tag{1.9}$$

An essential aspect of nonlinear spectroscopy is the control of the polarization of the incoming and outgoing laser beams, which allows specific tensor elements of the $\chi_{ijk}^{(2)}$ to be probed. In such a setup, the linearly polarized light is classified with respect to the surface normal or the plane of incidence of the interface (Figure 1.4), where the 'P' polarization is parallel to the surface normal. The horizontally polarized light, which is perpendicular (in the XZ plane), is called the 'S' polarization. These are derived from the German words for parallel and perpendicular, parallel and senkrecht.

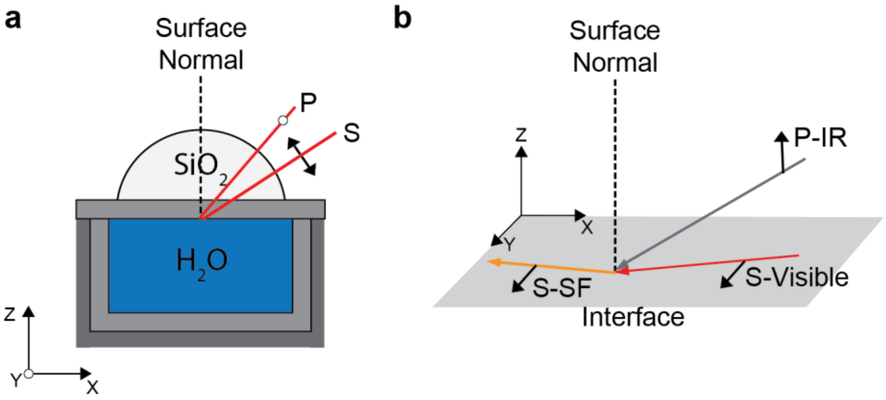

Figure 1.4: (a) Polarization combinations in the reflective experimental geometry and (b) indicating the SSP polarization. The axis system is arbitrarily drawn.

Since the silica/water interface possesses $C_{\infty v}$ symmetry, spatial symmetry results in 7 elements of the 27 tensor elements being non-zero. Furthermore, as the X and Y axes are identical, only 4 unique non-zero tensor elements exist. These are $\chi^{(2)}_{zxx} = \chi^{(2)}_{zyy}$, $\chi^{(2)}_{xxz} = \chi^{(2)}_{yyz}$, $\chi^{(2)}_{xzx} = \chi^{(2)}_{yzy}$, and $\chi^{(2)}_{zzz}$ elements. Different elements of the nonlinear susceptibility can be accessed by controlling the polarization combinations of the incident beam (Table 1.2). Here the acronyms in the polarization configurations refer to the polarizations of light in order of decreasing energy. For example, in the case of sum frequency generation, SSP refers to S-polarized sum frequency generated, S-polarized visible (800 nm), and P-polarized infra-red light.

Table 1.2: Elements of the second order nonlinear susceptibility probed by the different experimental polarization configurations.

Polarization Configuration	Elements Probed
SSP	$\chi^{(2)}_{yyz}$
PSS	$\chi^{(2)}_{zyy}$
SPS	$\chi^{(2)}_{yzy}$
PPP	$\chi^{(2)}_{zzz}, \chi^{(2)}_{zxx}, \chi^{(2)}_{xzx}, \chi^{(2)}_{xxz}$

1.4.5 Nonresonant Second Harmonic Generation

Following the first experimental demonstrated by Franken et al.[16], second harmonic generation spectroscopy was pioneered by Bloembergen[53] and found applications in catalysis,[26,54] biology,[55,56] microscopy,[57] and environmental sciences.[58–62]

In its simplest form, homodyne nonresonant second harmonic generation involves the spatial and temporal overlap of light of the same frequency to yield second harmonic generation light. This process involves the excitation to a virtual state by each photon, which leads to the generation of the second harmonic light (Figure 1.5(a)). An example of how to achieve such a process experimentally is the reflective geometry whereby laser pulses in the visible region are spatially and temporally overlapped at an interface, and a detector can measure the resultant second harmonic light (2ω) in conjunction with a photon counter. The intensity of the second harmonic light generated is measured as a function of time. Variations in the bulk pH, ionic strength, and composition of the aqueous phase result in intensity changes that can be related to the EDL's structural and electrical properties.

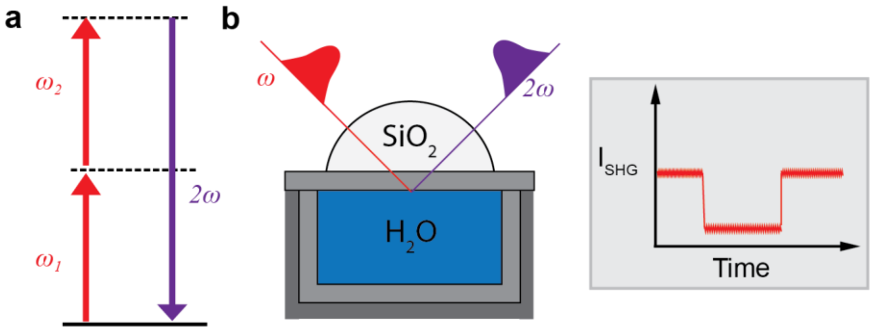

Figure 1.5: (a) Energy level diagram and (b) experimental setup for SHG measurements.

In SHG, the intensity of the measurement (I_{SHG}) is proportional to the square modulus of the electric field ($E_{2\omega}$) of the SHG light generated from the interface, which in turn is proportional to the second-order nonlinear susceptibility ($\chi^{(2)}_{total}$):

$$I_{SHG} \propto |E_{2\omega}|^2 \propto \left|\chi^{(2)}_{total}\right|^2. \tag{1.10}$$

All species with noncentrosymmetric structures can contribute to the measured response. It is important to remember that this process only accounts for the interaction of the electric fields of light with the system. However, at charged interfaces, the situation is complicated by the presence of a static electric field emanating from the negative charges on the surface. As a result, a model was required to rationalize the findings from the SHG measurements, as discussed below.

1.4.5.1 The $\chi^{(3)}$ Method

A unique model to interpret SHG is needed due to the challenge presented by charged interfaces such as mineral oxides. The seminal model referred to as the $\chi^{(3)}$ method was pioneered by Eisenthal and coworkers.[41] In this study, SHG measurements were done at the silica/water interface over a pH range of 2 to 14 in the presence of 500 mM NaCl (Figure 1.6). The magnitude of the SHG intensity was found to be the smallest at pH 2. However, as the pH was increased, a significant growth in the SHG intensity was observed.

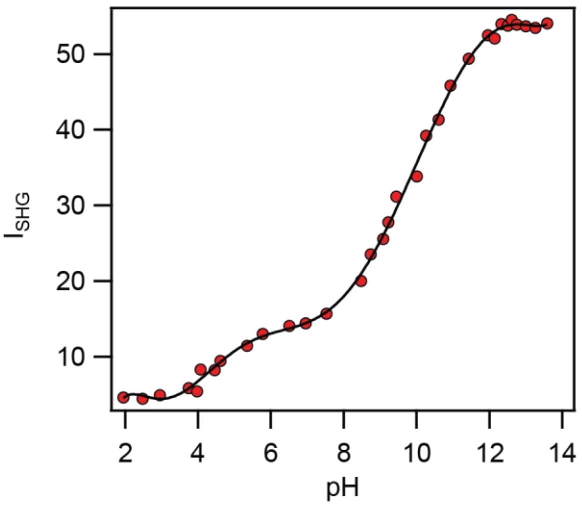

Figure 1.6: SHG measurements done at the silica/water interface in the presence of 500 mM NaCl. The solid line is used to guide the eye. Data was reproduced from Eisenthal and coworkers.[41] Copyright 1992, with permission from Elsevier.

To rationalize these findings, the authors considered that pH 2 would correspond to the expected point of zero charge (pzc) of silica, and above this pH deprotonation of the silanol sites to siloxides would lead to an increase in the surface charge density and hence the interfacial potential. As a result, the core proposal of the $\chi^{(3)}$ model is that the non-resonant second harmonic signal intensity can be explained by the alignment or polarization of water molecules interacting with an interfacial potential (Φ_0) originating from the charged silica surface. The intensity of SHG could be related both to the second-order nonlinear susceptibility $\chi^{(2)}$ accounting for the electric fields of light (E) and the product of the third-order susceptibility $\chi^{(3)}$ and the surface potential of the silica surface Φ_0, which accounts for the interaction of electric field of light with the electric field originating from the surface. This relationship is given by:

$$\sqrt{I_{SHG}} \propto E_{SHG} \propto |\chi^{(2)} E_j E_k + \chi^{(3)} \Phi_0 E_j E_k|. \tag{1.11}$$

Theoretically, $\chi^{(2)}$ contains contributions from every molecular species composing the interface, while $\chi^{(3)}$ describes only the contribution of water based on the interaction with the interfacial potential (Φ_0). This contribution is given by Equation 1.11. Therefore, the authors proposed that at pH 2 the contribution from the $\chi^{(3)}\Phi_0$ was zero, and the signal stemmed from $\chi^{(2)}$, which was assumed to be independent of potential.[41]

1.4.5.2 Phase Matching in the $\chi^{(3)}$ Method

In any second-order nonlinear optical process, phase matching of the laser beams involved plays a critical role in determining the efficiency of the process.[13] Phase matching originates from the induced dipoles in the medium coherently oscillating with a definite phase relationship between them. This process can result in constructive or destructive interference between them, thus resulting in larger or smaller observed intensity. Phase matching depends on the properties of the medium and the angles of incidence or reflection of the laser beams.

When utilizing SHG or vSFG at charged interfaces, Roke[63] and Tian[64] illustrated how interference can contribute to the measurements. This determination involves considering the wavevector of the laser beams ($\vec{k}_{iz}$) with respect to the surface normal of the interface (Figure 1.7).

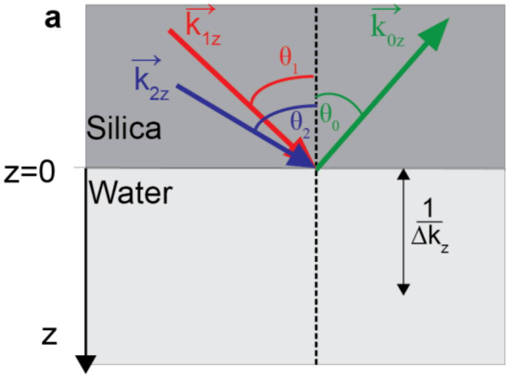

Figure 1.7: (a) Wavevectors at the silica/water interface (note: reflected beams not shown). Figure adapted from Roke and coworkers.[63] Copyright 2016 American Chemical Society.

To quantify the phase matching, the wavevector mismatch factor (Δk_z) is determined along the surface normal (z-direction) by,[63,65]

$$\Delta k_z = |\vec{k}_{2z} + \vec{k}_{1z} - \vec{k}_{0z}| = k_{2z} + k_{1z} + k_{0z}, \tag{1.12}$$

$$k_{iz} = \omega_i / c\sqrt{n(\omega_i)^2 - \sin(\theta_i)^2}. \tag{1.13}$$

Here, ω_i refers to the frequency, n is the frequency-dependent refractive index, and θ_i is the angle of incidence or reflection. For vSFG, Equation 1.12 is suitable as it involves IR and visible beams, however, in the case of collinear SHG, as described above, the equation is modified as $k_{2z} = k_{1z}$. Nonetheless, the distance along the surface normal that phase matching takes place is known as the coherence length (1/ Δk_z).

Over the last 10 years, the original additive model has been reformulated to include the phase mismatch term, Δk_z, to account for the interference occurring at the interface.[63,64,66] For high ionic strengths and low surface potentials, this gives

$$\sqrt{I_{SHG}} \propto E_{SHG} \propto |\chi^{(2)} E_j E_k + \chi^{(3)} E_j E_k \Phi_0 f_3|, \tag{1.14}$$

$$f_3 = \frac{\kappa}{\kappa - i\Delta k_z}. \tag{1.15}$$

However, at low ionic strengths and high potentials, Hore and Tyrode[67] showed that the full solution of the Poisson-Boltzmann equation is required, and the diffuse layer is modeled by

$$E_{SHG} \propto |\chi^{(2)} E_j E_k + \chi^{(3)} g_3 E_j E_k|, \tag{1.16}$$

$$g_3 = \left[\Phi_0 - \frac{4ik_B T\Delta k_z}{e}\sum_{n=1}^{\infty}\frac{\xi^{2n-1}}{(2n-1)[i\Delta k_z - \kappa(2n-1)]}\right]. \tag{1.17}$$

Here, k_B is the Boltzmann constant, e is the electron charge, and T is the temperature. As a result, the measured second harmonic signal depends on Debye and coherence lengths. This interference between the nonlinear response within and beyond the coherence length results in destructive interference. Circumventing this interference can be achieved by varying the incident angles,[57] frequency,[58] or by increasing the concentration of counterions in the solution.[63,68–71]

The inclusion of phase matching was significant as it accounted for the screening factor that is a function of both the wavevector mismatch and Debye length. It led to the schemes which allowed the determination of the surface potential from non-resonant nonlinear optical approaches.[72] Finally, as discussed later, the updated model was successfully extended to vibrational sum frequency generation studies, which could separate the responses of the Stern and diffuse layers.[64,67–69]

1.4.5.3 Shortfalls of the $\chi^{(3)}$ Method

Discrepancies in the $\chi^{(3)}$ method can be found when adopting it at oxide interfaces other than silica and comparing it to complementary techniques such as vSFG[73,74] and streaming potential.[11] To illustrate the inconsistencies of the $\chi^{(3)}$ method at different interfaces, we utilize the example of the alumina (Al_2O_3)/water interface. In Figure 1.8, we present the previous SHG measurements done on different types of alumina substrates.[11,75,76] The dashed vertical lines indicate the point of zero charge reported in these studies. Above this pH, the surface becomes negatively charged, whereas, below this point, the surface becomes positively charged.

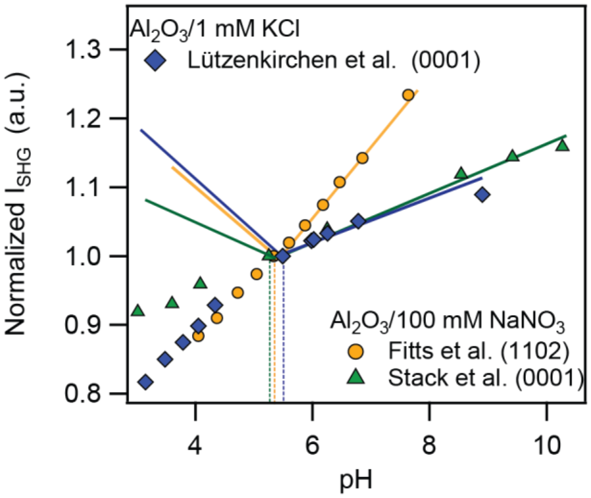

Figure 1.8: Previous SHG measurements at the alumina/water interfaces, with intensity normalized to the value at the point of zero charge reported. Dashed lines indicate the pH of the

point of zero charge reported in these studies. The solid lines represent the values predicted by the model proposed by Eisenthal and coworkers.[41] Copyright 1992, with permission from Elsevier.

While the conditions (electrolyte, polarization conditions, flow vs. no flow, geometry) in these studies are different, it is evident that all the studies observe a decrease in the SHG intensity observed as the pH is lowered. Such findings were also observed at the TiO_2/water interface too.[77] This is contrary to the estimation of the $\chi^{(3)}$ method (solid lines), assuming the contribution of $\chi^{(2)}$ is minimal, which predicts that the SHG intensity would increase below the point of zero charge due to the growth of the positive potential ($\Phi(z)$).

1.4.5.4 Rethinking the $\chi^{(3)}$ Method

To tackle the inadequacies of the $\chi^{(3)}$ method, Bonn and coworkers[74] compared the SHG and vSFG measurements at the air/membrane monolayer/ aqueous interface. In this study, they varied the composition of the monolayer to yield a net positive, neutral, and negative surface. The vSFG measurements indicate that the spectral area would be the least at the neutral monolayer composition. When the monolayer becomes negatively or positively charged, the area increases in magnitude (in agreement with the $\chi^{(3)}$ method). However, the SHG measurements decreased as the monolayer composition was changed from positive to negative.

To account for the difference between the vSFG and SHG measurements, they proposed that SHG measurement originated from three primary sources: (i) constant hyper-Rayleigh scattering contribution, (ii) water molecules, and (iii) the monolayer (substrate in this work). They hypothesized that the change in the water orientation, as observed in the vSFG spectra, would constructively and destructively interfere with the monolayer. While this work highlighted the possibility of interference between the monolayer and water, it is unclear how these findings can be used to rationalize the work at the silica/water interface.

Work by Rehl et al.[73] revisited Eisenthal and coworkers' experiments at the silica/water interface at 500 mM NaCl, with a comparison between the SHG and vSFG responses. Both techniques displayed similar behavior in the high pH (7 -12) region, increasing in magnitude with increasing pH, but a different trend at low pH (7-2). This difference at low pH was attributed to destructive interference between the SHG response of the water molecules and the SHG response of the silica. The change from constructive to destructive interference from high to low pH was attributed to the reorientation (i.e., flipping) of the water molecules in the aqueous phase, which would change the sign of their SHG response while the sign of the silica SHG response remained unchanged.[44,78]

These studies served as vital benchmarks as the contribution of the substrate to the second harmonic signal was not considered previously. Such constructive or destructive interference could be used to rationalize the SHG observations at other mineral oxide interfaces, as discussed above. However, it is unclear how this will manifest in the nonlinear susceptibilities and hence the $\chi^{(3)}$ method.

1.4.5.5 Revising the $\chi^{(3)}$ Method

The shortcomings of the $\chi^{(3)}$ method highlighted in these studies prompted the need to revise the model. The development of phase-sensitive or heterodyne second harmonic generation (HD-SHG) by the Geiger lab[72] permitted the determination of both the phase and amplitude. Determining these properties provided the complex values of the nonlinear susceptibilities and, more importantly, the surface potential.[70,71,79,80]

In relation to the $\chi^{(3)}$ method, Geiger and coworkers[81] found the existence of a new third-order term under conditions similar to those used by Eisenthal and coworkers.[41] They showed that the phase changes taking place within this pH range could be related to a new third-order term which they labeled $\chi_{\mathrm{x}}^{(3)}$. The inclusion of this term gives point estimates for interfacial potential (Φ_0) and $\chi^{(2)}$ terms in comparison to second harmonic scattering measurements.[82]

To determine the origin of this term, the authors considered three possibilities: (i) the substrate itself (silica), (ii) the surface roughness, and (iii) multipole moments contributing to the nonlinear response. Based on modeling the electric decay linearly in the silica and AFM measurements, they ruled out the first two possibilities and suggested that the likely source could potentially be multipolar contributions. While the inclusion of the term provides comparable surface potentials, the origin of the $\chi_{\mathrm{x}}^{(3)}$ remains uncertain.

To add to the discussion, Wang and coworkers[83] rigorously modeled the contribution of silica in the $\chi^{(3)}$ method. Like Geiger and coworkers, they proposed that silica contribution originates from an additional $\chi^{(3)}$ term. Their model considered the charge image screening and phase mismatching in the silica and water phases. Furthermore, by utilizing Gauss' theorem, they related the interfacial potential in water to that of silica, giving the expression:

$$\chi_{tot}^{(2)} = \chi^{(2)} + \left(-\chi_s^{(3)} \frac{\kappa_s}{\kappa_s - i\Delta k_z^s} \frac{\varepsilon_r^w \kappa_w}{\varepsilon_r^s \kappa_s} + \chi_w^{(3)} \frac{\kappa_w}{\kappa_w - i\Delta k_z^w}\right) \Phi_w(0). \tag{1.18}$$

Here, the subscript '*s*' refers to silica, while '*w*' refers to water. Based on this model, the third-order terms for silica and water will be in opposite sign (phase) and destructively interfering. When considering image charge screening and expressing the Debye length ($1/\kappa_s$) in silica in terms of water, this results in:

$$\chi^{(2)}_{tot} = \chi^{(2)} + \left(-50.7\frac{\kappa_w}{\kappa_w - i2.33\Delta k_z^s} + \frac{\kappa_w}{\kappa_w - i\Delta k_z^w}\right)\chi^{(3)}_w \Phi_w(0). \tag{1.19}$$

As is evident from Equation 1.19, the contribution of silica is more significant than water. At 100 mM NaCl, the authors showed that the contribution of silica would be 50 times greater than that of water. Furthermore, the values will be complex with both real and imaginary components, which does not agree with the findings of Geiger and coworkers.[81]

1.4.6 Vibrational Sum Frequency Generation

A closely related method of measuring the nonlinear response is vibrational sum frequency generation (vSFG). Pioneered by Shen and coworkers in the late 1980s,[48,49] the technique succeeded due to the high selectivity invoked by probing specific vibrational modes.

The vibrational resonance results in vibrational sum frequency generation (vSFG). In this process, an infrared (IR) laser pulse and visible pulse are combined in space and time to yield sum frequency light. One approach of vSFG is the combination of a broad IR pulse overlapping with a narrower visible pulse (Figure 1.9). This approach results in the IR light giving a resonant vibrational excitation, whereas the visible light would upconvert the process to the virtual state (dashed line), leading to an anti-Stokes shift.

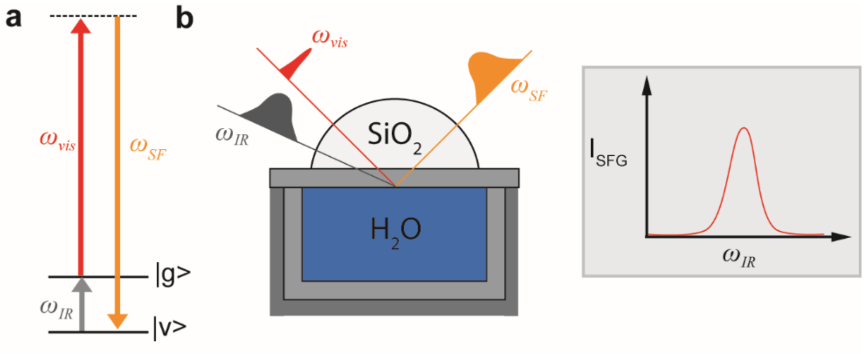

Figure 1.9: (a) Energy level diagram and (b) experimental setup for vibrational sum frequency generation.

The resultant sum-frequency light generated from this process is detected and reported as the vSFG spectrum. This intensity of the vibrational mode in the vSFG spectrum (I_{SFG}) is related to the complex total second-order nonlinear susceptibility by:

$$I_{SFG} = \left|\chi_{total}^{(2)}\right|^2 . \tag{1.20}$$

The second-order nonlinear susceptibility is modeled by considering the resonant ($\chi_R^{(2)}$) and nonresonant ($\chi_{NR}^{(2)}$) contributions to this term:

$$\chi_{total}^{(2)} = \chi_{NR}^{(2)} + \chi_R^{(2)}, \tag{1.21}$$

$$\chi_R^{(2)} = \sum_i \frac{A}{\omega-\omega_0+i\Gamma} . \tag{1.22}$$

Here A is the amplitude, Γ is the line width, and ω_0 is the frequency center of the vibrational mode. For dielectric surfaces such as silica, the contribution of the nonresonant term is much smaller than the resonant term. It is important to note that when the resonant term dominates, highly selective information can be obtained. This selectivity is due to the amplitude being directly proportional to the change in both the polarizability and dipole moment with a change in the normal mode.

1.2.6.1 Stern and Diffuse Layers vSFG Response

Despite the high interfacial sensitivity of vSFG, obtaining a detailed microscopic picture from the spectral analysis can be a challenge at a charged interface. This challenge stems from the difficulty of separating the Stern layer, the first layer(s) of water interacting with the surface, from the diffuse layer, which resembles the liquid structure modulated by the electric field. The need to obtain the Stern layer stems from the fact that it provides more direct information such as the specific ion effects,[86,87] charge transfer in reactions,[88] and acid-base chemistry[89,90] of the surfaces.

In the context of vSFG, a description of the Stern and diffuse layers can be modeled using the $\chi^{(3)}$ method,

$$\chi_{tot}^{(2)} = \chi_s^{(2)} + \chi_{DL}^{(2)}, \tag{1.23}$$

$$\chi_{DL}^{(2)} \equiv \int_0^{\infty} \chi^{(3)} E_0(z) e^{i\Delta k_z(z)} dz. \tag{1.24}$$

Here, $E_0(z)$ is the electric field, and the Stern and diffuse layers are represented by $\chi_s^{(2)}$ and $\chi_{DL}^{(2)}$, respectively. Depending on the ionic strength and the surface potentials, the terms f_3 or g_3 can be invoked to express the diffuse layer contribution in terms of the electric potential, i.e., the integral in Equation 1.24.

Several schemes have been used to isolate the Stern layer spectra. A well-received approach was that proposed by Tian and coworkers.[64] They showed that the Stern layer spectra could be acquired by assuming that the change in the complex vSFG spectra is minimal over two different pH or ionic strength points. As a result, the change is entirely due to the diffuse layer contribution, and with the knowledge of the potentials, the diffuse layer vSFG spectrum can be extracted from the total complex spectra. As a result, the diffuse layer spectra could be predicted over the salt or pH range since they are independent of the surface and are mediated by the surface potential.[66] Hence subtracting this contribution from the total complex spectra would yield the Stern layer[44], also known as bonded interfacial,[91] or topmost,[92] or surface bound.[69] This approach was the basis for several vSFG,[67,93,94] SHG,[70–72,79], and SHS[82] studies at the silica/water interface.

1.2.6.2 Interpretation of the vSFG Spectra

Obtaining the Stern layer spectra permits the prediction of the hydrogen bonding structure of water, where the molecules can be hydrogen bond donors or acceptors to each other.[95] However, the interactions with surface sites lead to a change in the water-water hydrogen bond interactions.

Furthermore, changes to the surface sites directly result in changes to these structures. Analysis of the vSFG Stern layer spectra can elucidate the orientation and the hydrogen bonding strength of the population of water molecules.

The orientation of the structures can be elucidated with vSFG due to the sensitivity to the change in the dipole moment with respect to the vibrational mode. For water, the orientation with respect to the surface normal can be related to the sign of the peaks in the imaginary SSP spectra.[96] For positive peaks, the hydrogen atoms in water will point towards the surface, while negative peaks indicate the opposite, i.e., hydrogen pointing towards the bulk solution.

The hydrogen bonding strength can be inferred based on the position of the peaks. The assignment of the vSFG spectra originates from work by Shen and coworkers[42], who attributed the 3200 cm^{-1} mode to the symmetric stretch of strongly coordinated water molecules, and the 3400 cm^{-1} mode symmetric stretches of weakly coordinated waters and the asymmetric stretches. While this assignment was later refined, it is generally agreed that the lower wavenumber mode corresponds to strongly hydrogen-bonded water molecules.[96–98] From this contribution, the 3200 cm^{-1} and 3400 cm^{-1} modes were often referred to as the 'ice-like' and 'liquid-like' peaks, respectively.[99–102] However, this assignment remains contentious as vibrational coupling strongly influences water's vSFG spectra.

1.2.6.3 Vibrational Coupling

The spectral interference between different resonant vibrational modes can lead to spectral misinterpretations. Chief amongst these effects is the influence of intramolecular coupling or Fermi resonance on the spectrum. Figure 1.10(a) shows the influence of the Fermi resonance on the vSFG spectrum of the silica/water interface. The overtone of the bend (δ_2) appears in the O-H stretching spectral region of water (2800-3700 cm^{-1}) and is approximately the same energy and symmetry as the stretching mode. This results in the weaker overtone of the bend gaining intensity and the O-H stretch becoming blue-shifted relative to its original position. This phenomenon is referred to as a Fermi resonance, and in the intensity vSFG spectrum of silica/water (blue spectrum Figure 1.10(a)), the mode at 3200 cm^{-1} is assigned to it.[103,104] This Fermi resonance results in spectral interference with the signal originating from the water molecules and thereby misleading interpretations of experimental measurements.[105,106]

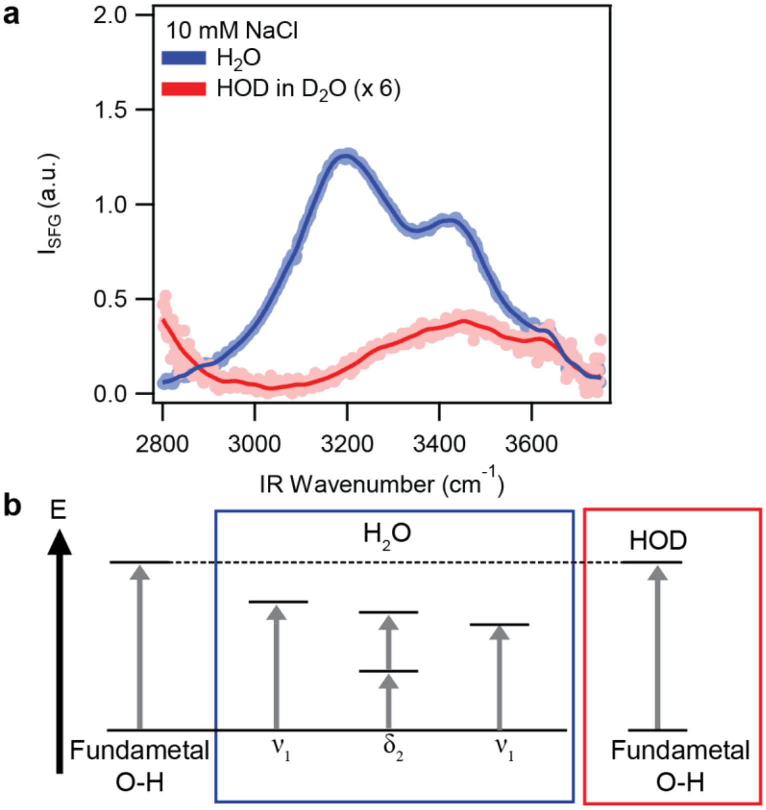

Figure 1.10: (a) vSFG spectra indicating the presence and absence of the Fermi resonance at the silica/water and silica/HOD interfaces, respectively. (b) Energy level diagram depicting the Fermi resonance process. Here ν_1 and δ_2 refer to the symmetric stretch and bend modes, respectively.

The Fermi resonance also masks intermolecular vibrational coupling between water molecules. This form of coupling originates from the ability of water to dissipate energy through the hydrogen bonding network. Raman or IR spectroscopy is associated with the redshift and broadening of vibrational modes. The dependence on the hydrogen bonding environment hints that the orientation of the water molecules in the hydrogen bonding environment plays a crucial role in modulating the extent of intermolecular coupling. Indeed, molecular dynamic simulations have shown that the presence of different conformations of hydrogen bonding structures of water influences the extent of intermolecular coupling at the air/water interface.[107]

Both forms of coupling can be circumvented using isotopic dilution with mixtures of heavy water (D_2O) and water (H_2O). The Fermi resonance is mitigated by the change in the symmetry and energy associated with the bend vibration. Intermolecular coupling is mitigated as the O-H stretch cannot dissipate energy to the surrounding D2O molecules resonantly. This results in the fundamental O-H stretch only becoming visible in the vibrational spectrum (Figure 1.10(a)). Furthermore, since the O-H stretch is isolated, it directly reports on hydrogen bonding in a localized environment.

1.5 Microscopic Picture

1.5.1 Importance of the Molecular Hyperpolarizability

While using electronic structure computations has provided insights at interfaces, applying nonlinear optics in material science,[108,109] optical telecommunications,[110] 3D data storage,[111] spectroscopy,[30] and biological imaging[57] has motivated the need to develop high-performance materials. As a result, several experimental and computational studies have been centered on predicting the second-order properties of systems that can be suitable for the applications described above.[20] As noted previously, the proportional relationship between the second-order nonlinear susceptibility and the hyperpolarizability allows the macroscopic properties of the materials to be directly related to the microscopic level. As a result, determining molecular hyperpolarizability is important to understand the response of the materials.

1.5.2 Hyperpolarizability and Charge Transfer

An important relationship discovered early on is that the hyperpolarizability can be related to the intramolecular and intermolecular charge transfer interactions on a microscopic level.[112–116] This sensitivity to charge transfer interactions was proposed to originate from the unique acentric symmetry properties of the hyperpolarizability.[114] In general, it is found that systems capable of large charge transfer exhibit high hyperpolarizability values.

Early work[112–115,117] highlighted that conjugated systems such as substituted benzenes can have increased hyperpolarizabilities due to the interaction of individual substituents with the conjugated π ring. However, the hyperpolarizabilities significantly increase when more dominant charge transfer interactions between donor and acceptor groups are included. This behaviour is exemplified in donor-acceptor or push-pull π-conjugated systems such as the nitroaniline isomers. In such systems, a dominant transition exists between the HOMO, which is localized in the donor group, and LUMO, which is localized in the acceptor group.[112] As shown in Figure 1.11, different charge transfer characteristics occur due to the difference in resonance structures and spatial separation between the donor (NH2) and acceptor (NO2) groups in these isomers.[113] As shown, para and ortho isomers have resonance structures involving a significant extra delocalization of π-electrons compared to the meta isomer.

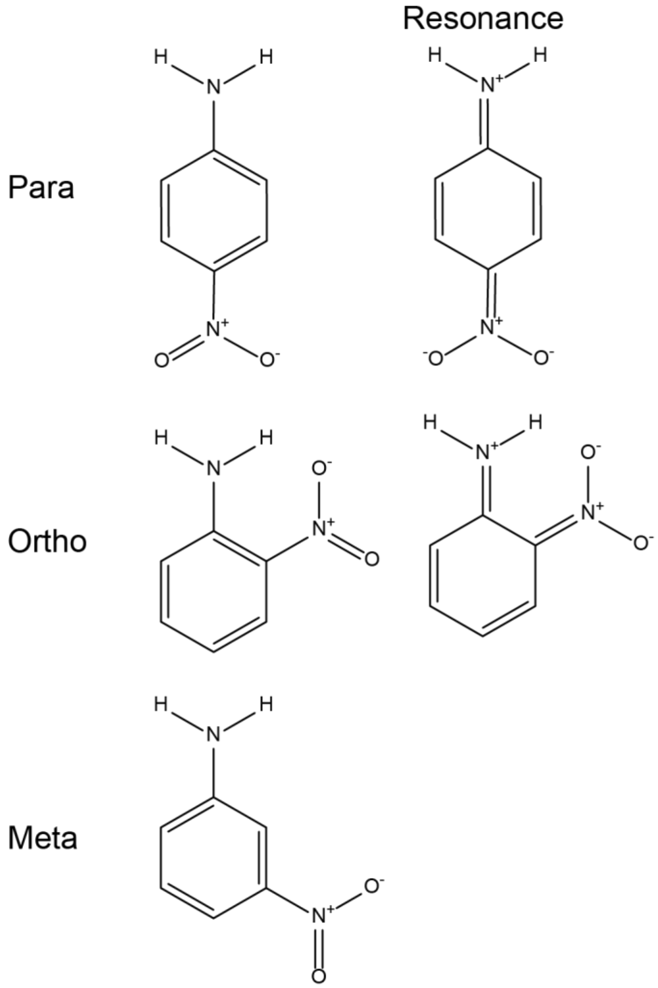

Figure 1.11: Para, ortho, and meta-nitroaniline structures along with their corresponding resonance structures. Parts of the figure are adapted from Levine.[113] Copyright 1976, with permission from Elsevier.

Oudar and Chemla quantified this relationship between the charge transfer and hyperpolarizability in donor-acceptor chromophores.[112,117] They utilized the two-state model (discussed later) to highlight that the low-lying charge transfer transitions dictated the NLO response. As a result, the total response measured was the sum of the additive and donor-acceptor charge transfer characteristics (β_{ct}), i.e.,

$$\beta = \beta_{add} + \beta_{ct} \,. \tag{1.25}$$

Here the additive portion accounts for the interaction of an individual substituent and the benzene ring.

1.5.3 Experimental Approaches for Determining the Hyperpolarizability

Determining the molecular hyperpolarizability in liquids requires experimental measurements from electric field-induced second harmonic generation (EFISH) and hyper Rayleigh scattering (HRS). In EFISH experiments, a dc-electric field is applied to polarize the liquid in addition to the two incident beams. The presence of three fields results in third-order nonlinear susceptibility ($\chi^{(3)}$) being measured. This measurement can be related to the thermally averaged microscopic hyperpolarizability (Γ) via

$$\chi^{(3)}(-2\omega;\omega,\omega,0) \ = \frac{1}{4}L_0L_\omega L_{2\omega}N\Gamma. \tag{1.26}$$

Here, L_ω represents the local field factor at a frequency (ω), and N is the molecular number density. For a polar molecule in electric fields with parallel polarizations, the thermally averaged hyperpolarizability can be related to the hyperpolarizability in the direction of the dipole moment ($\beta_{||}$),[118]

$$\Gamma \ = \gamma + \frac{\mu_o\beta_{||}}{3kT}. \tag{1.27}$$

Here, γ is the second hyperpolarizability, k is the Boltzmann constant, T is the temperature, and μ_o is the static dipole moment.

Hyper-Rayleigh scattering is a nonlinear elastic scattering technique where the microscopic orientational fluctuations give rise to incoherent scattered second harmonic light [$I(2\omega)$].[119,120] The observed scattered harmonic light can then be utilized to determine the hyperpolarizability. It is common in these experimental set ups[118,121] that the hyperpolarizability is dominated by the β_{zzz}:

$$I(2\omega) \propto \beta_{HRS}^2 = \langle \beta_{zzz}^2 \rangle = \frac{1}{35}(5\beta_{zzz}^2 + 12\beta_{zzz}\beta_{zxx} + 24\beta_{zxx}^2). \quad (1.28)$$

Although these techniques are routinely used to measure hyperpolarizabilities, they are not without problems. As noted in Equation 1.27, EFISH studies require complementary third harmonic generation, dipole moment, dielectric constant, and refractive indices measurements at the excitation frequencies utilized.[122] HRS can be influenced by multiphoton absorption and requires sensitive detection due to a broad background signal which may contribute.[123]

1.5.4 Computational Approaches

Hyperpolarizabilities can be computed using quantum chemical methods, providing a microscopic understanding of the underlying fundamental properties leading to large (or small) hyperpolarizabilities.[20,124] Tuning these properties can develop systems with excellent nonlinear optical properties. The common approaches used to determine the hyperpolarizability are (i) sum over states (SOS), (ii) response theory (RT), and (iii) finite field (FF). Here the focus is placed on the first two approaches employed in this thesis. More details on the finite field approach, which has not been used here, can be found in the literature.[125,126]

1.5.4.1 Sum Over States

The sum over states (SOS) approach describes the magnitude of the hyperpolarizability based on the summation over all the excited states of the molecule.[127–129] The approach is derived from time-dependent perturbation theory, and a detailed description can be found in the book by Boyd titled "Nonlinear optics".[12] The expression utilized to compute a hyperpolarizability element (β_{ijk}) with the excitation frequencies (ω_p and ω_q) is given by:

$$\beta_{ijk}(-\omega_\sigma, \omega_p\,, \omega_q) = \mathcal{P}_I \sum_{m,n} \left[\frac{\langle g|\,\mu_i\,|n\rangle\langle n|\,\mu_j\,|m\rangle\langle m|\,\mu_k\,|g\rangle}{(\omega_{ng}-\omega_\sigma)(\omega_{mg}-\omega_p)} + \frac{\langle g|\,\mu_j\,|n\rangle\langle n|\,\mu_i\,|m\rangle\langle m|\,\mu_k\,|g\rangle}{(\omega_{ng}^{*}+\omega_q)(\omega_{mg}-\omega_p)} + \frac{\langle g|\,\mu_j\,|n\rangle\langle n|\,\mu_k\,|m\rangle\langle m|\,\mu_i\,|g\rangle}{(\omega_{ng}^{*}+\omega_q)(\omega_{mg}^{*}+\omega_\sigma)} \right]. \tag{1.29}$$

Here, $\omega_\sigma = \omega_p + \omega_q$, while ω_{ng} and ω_{mg} are the energy separation between the ground (g) and excited states, n and m, respectively. The asterisk on the energy separation terms indicates the terms contain complex damping, where $\omega_{mg}^{*} = (E_m - E_g)/\hbar - i\gamma/2$, and γ is the damping parameter. $\mathcal{P}_I$ is the full permutation operator, which results in the summation of all the input and output frequencies permutations. Here, the six different permutations representing the excitations between the states n, m, and g are considered (Figure 1.12).

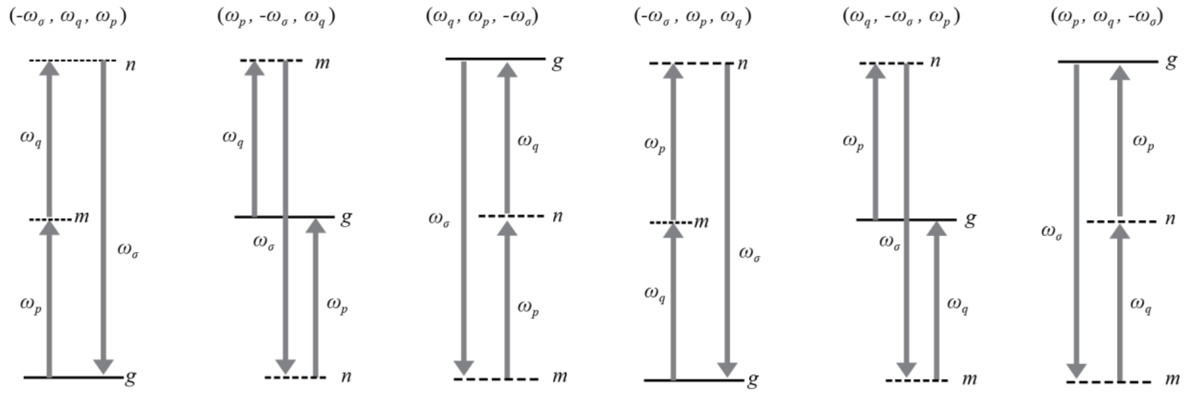

Figure 1.12: Six excitation permutations accounted for by the sum over states approach. Figure adapted from Boyd.[12] Copyright 2020, with permission from Elsevier

The hyperpolarizability can be determined by computing the transition dipole moments and the permanent dipole moment difference between ground and excited states. However, the computation of a set of excitation energies, transition dipole moments, and permanent dipoles of the excited states is computationally expensive,[130], and suffers from increased inaccuracies in the determination of higher-lying excited states. Furthermore, adding states usually results in poor convergence of the hyperpolarizability values.[131]

The sum over states approach can be simplified by only including a few states contributing strongly to the nonlinear optical response. The most straightforward scheme for achieving this is the two-state model (TSM), which sums over the ground (*g*) and a single excited (*e*) state. This model describes the relationship between hyperpolarizabilities and intramolecular charge transfer in donor-acceptor molecules.[112] In this model, the non-resonant hyperpolarizabilities computed are determined as

$$\beta_{||} = \frac{3}{5}\beta_z^T = \frac{\beta^{Static}}{(1 - \omega_p\omega_q/\omega_{eg}^2)(1 - 4\omega_p\omega_q/\omega_{eg}^2)}, \tag{1.30}$$

$$\beta^{Static} = \frac{6\mu_{eg}^2(\mu_e - \mu_g)}{\omega_{eg}^2}, \tag{1.31}$$

where β^{Static} is the static hyperpolarizability, μ_{eg} is the transition dipole moment, and μ_g, μ_e are the permanent dipole moments of the ground and excited states.[132]

1.5.4.2 Response theory

Response theory models the response of a molecular system to an external field, such as the electric field of electromagnetic radiation. This approach involves determining the change in the wave function due to the interaction of the electric field with the molecule. In quantum mechanics, when the wave function interacts with a field, the electronic ground state becomes a superposition of many electronic states.[133] As a result, determining the electronic ground state response permits the resolution of properties associated with transitions from the ground state to excited states induced by one or more photons. The electronic ground state can be computed with standard methods such as Hartree-Fock theory (HF), density functional theory (DFT), or coupled cluster (CC) theory.

In response theory, the expectation value of an operator **P** is expanded with perturbations **P**, **Q, R,** etc, where[134]

$$\langle \mathbf{P}\rangle(t) = \langle \mathbf{P}\rangle(0) + \sum_a e^{-i\omega_a t}\, \langle\langle \mathbf{P}; \mathbf{Q}\rangle\rangle_{\omega_a} \mathbf{F}_a + \frac{1}{2}\sum_k e^{-i(\omega_a+\omega_b)t}\, \langle\langle \mathbf{P}; \mathbf{Q}, \mathbf{R}\rangle\rangle_{\omega_a,\omega_b} \mathbf{F}_a \mathbf{F}_b + \ldots \quad (1.32)$$

The linear, quadratic, and cubic responses can be interpreted as the change in the property P due to the perturbations **P** and **Q**. For the determination of the first-order hyperpolarizabilities, the quadratic response function (for the dipole operator) needs to be considered, i.e.,

$$\beta_{ijk}(\omega_\sigma; \omega_a, \omega_b) = -\langle\langle \mu_i; \mu_j, \mu_k\rangle\rangle_{\omega_a,\omega_b}. \quad (1.33)$$

It is important to note that this formalism only extends to off-resonant scenarios. In on-resonance cases, the finite lifetime of the excited electronic states (damping factor) must be considered. This method for dealing with on-resonant scenarios is called damped response theory.[135]

1.5.5 Density Functional Theory

Determining the molecular hyperpolarizability inherently depends on the level of theory utilized (i.e., method and basis set). While the ideal route is to utilize gold standard approaches such as coupled cluster with large basis sets, these approaches are restricted due to their high computational cost. The more common approach to compute the hyperpolarizabilities is with density functional theory (DFT). A simplified expression of DFT breaks down the total ground state energy (E_0) as follows,[134]

$$E_0[\rho(r)] = E_{KE}[\rho(r)] + E_J[\rho(r)] + E_{XC}[\rho(r)], \quad (1.34)$$

where the terms represent the kinetic energy, Coulombic energy, and exchange-correlation energy, respectively. The total ground state energy can be determined if the exact form of the functional $E_{XC}[\rho(r)]$ is known,. However, $E_{XC}[\rho(r)]$ is unknown and, as a result, is approximated with various DFT functionals. In these functionals, the $E_{XC}[\rho(r)]$ term is (often) separated into the pure exchange ($E_X[\rho(r)]$) and pure correlation ($E_C[\rho(r)]$),

$$E_{XC}[\rho(r)] = E_X[\rho(r)] + E_C[\rho(r)]. \tag{1.35}$$

The treatment of these two terms gives rise to different functionals. Perdew presented a "Jacob's ladder" approach, where the functionals can be classified according to the fundamental variables governing the exchange-correlation functional.[136,137] These functionals can be classified as local density approximation (LDA), which assumes that the density can be treated as a uniform electron gas. Generalized gradient approximation (GGA) includes the derivative of the density. Meta-GGA includes the second derivatives of the density. Hybrids include exact (Hartree Fock) exchange, and generalized random phase methods include virtual orbitals (e.g., double hybrids).

Early DFT computations of hyperpolarizabilities mainly focused on using GGA and hybrid functionals.[138–140] Compared to Hartree-Fock[141] and semi-empirical methods,[142,143] the approaches improved the hyperpolarizabilities. However, the accuracy was still poor compared to the experimental values and high-level approaches.[139,144] Indeed, such deficiencies have been linked to the wrong asymptotic exchange potential behaviour in these functionals which leads to the poor description of charge transfer excitations.[145–150] To overcome this limitation, a new set of functionals known as range-separated hybrid (RSH) functionals (also referred to as long-range corrected functionals) was proposed.[151–153] Range-separated hybrid (RSH) functionals split the repulsive inter-electron Coulomb potential operator into long- and short-range parts, typically with an error function (*erf*),

$$\frac{1}{r} = \frac{\alpha+\beta erf(\omega r)}{r} + \frac{1-[\alpha+\beta erf(\omega r)]}{r}. \tag{1.36}$$

Here r is the inter-electronic distance and ω is the range separation parameter. In the exchange term, the long-range component is determined with Hartree Fock theory while the short-range part is treated with the DFT (usually GGA) exchange, giving

$$E_{xc} = \alpha E_{x,HF}^{SR} + (1-\alpha)E_{x,GGA}^{SR} + (\alpha+\beta)E_{x,HF}^{LR} + (1-\alpha+\beta)E_{x,GGA}^{LR} + E_{c,GGA}. \tag{1.37}$$

Here, α and $\alpha+\beta$ control the fraction of short- and long-range exchange from the GGA and HF. Differences in the range separation functionals are based on the choice of the GGA and values of the α, β, and ω parameters. The range separation parameter, ω, is not to be confused with the incident frequency, ω.

1.5.6 Optimal Gap Tuning

Compared to the GGA and hybrid functionals, RSH functionals improved the prediction of hyperpolarizabilities and related properties as smaller errors were obtained relative to experiments and higher-level calculations.[154–160] However, there was still a lack of accuracy in describing the hyperpolarizabilities accurately with respect to experiments or high-level computations.[161] These shortcomings of RSH functionals extend to other charge transfer properties, such as charge transfer excitations and optical band gaps.[162,163] The poor accuracy can be traced back to the fundamental properties of the functionals, whereby the asymptotically correct behaviour depends on the long-range exact exchange, which is intrinsically dependent on the range separation parameter (ω).[164] A default value of the parameter is set based on benchmarking of charge transfer excitations.[165] However, the range separation parameter is system dependent.[166]

To overcome the challenges of accurately predicting the range separation parameter of the RSH functionals, Kronik and coworkers developed a procedure known as optimal gap tuning, where the range separation parameter (ω) can be determined non-empirically from first principles.[167–170] In the approach, the range separation parameter is optimally tuned such that the molecular properties obey Koopman's theorem.[171] As such, the gas phase ionization potential must be the same as the eigenvalue of the highest occupied molecular orbital (HOMO). To achieve this agreement, the value of ω is varied until this condition is met, i.e.,

$$\varepsilon_{HOMO}^{N}(\omega) = -\, IP^{N}(\omega). \tag{1.38}$$

The eigenvalue of the HOMO (ε_{HOMO}) is obtained from the neutral molecule (*N* electrons), while the ionization potential (IP) is the total electronic energy difference between the neutral and cationic forms of the molecule (*N-1*). This constraint can be further restricted by considering the electron affinity (*N+1* electrons) and ionization potential of the anion in the function defined by:

$$J^{2}(\omega) = (\varepsilon_{HOMO}^{N}(\omega) + IP^{N}(\omega))^{2} + (\varepsilon_{HOMO}^{N+1}(\omega) + IP^{N+1}(\omega))^{2}. \tag{1.39}$$

A key component of optimal gap tuning is the need to account for the solvation. Typically, in previous studies, tuning in solvent was accomplished by embedding the molecule of interest in solvent modeled by the polarizable continuum model (PCM).[155,172] However, the combination of the PCM and optimal gap tuning leads to misleading values of ω due to the use of PCM affecting the total energies and hence the ionization potential.[164] However, the use of PCM hardly affects the eigenvalues of the frontier orbitals, which are critical to optimal gap tuning. As a result, applying optimal gap tuning to the prediction of hyperpolarizabilities has had contradictory findings and mixed success.[161,166,173]

1.6 Thesis Scope and Motivation

The cornerstone of this thesis is the use of computational and experimental approaches based on nonlinear optical spectroscopy to reveal novel physical insights and address the current challenges facing these techniques. In Chapter 2, we address the challenge of the influence of the excitation wavelength on the molecular hyperpolarizability response of the nitroaniline isomers studied in both the gas phase and solvent (PCM). Furthermore, the influence of the excitation wavelength on optimal gap tuning of the range-separated hybrid functionals is highlighted.

On a macroscopic level, despite the advances in both theory and experimental measurements of vSFG, several challenges make it difficult to gain molecular structural information from spectral analysis. One such challenge in vibrational studies in the O-H stretch region is the presence of the Fermi resonance between the bend overtone and the O-H stretch. The Fermi resonance in water occurs due to the mixing of the two states resulting in the overtone of the bend gaining intensity from the fundamental mode, which has the exact symmetry and both modes shifting away from each other. The Fermi resonance can be eliminated using an isotopic dilution of water with heavy water (D_2O).

Chapter 3 highlights the use of experimental vSFG measurements at the interface between isotopically diluted water (HOD in D_2O) and silica to elucidate the inter and intra-vibrational coupling on total EDL vSFG spectra. Using the maximum entropy method and the approach proposed by Wen et al.,[64] we can isolate the Stern and diffuse layers of the electrical double layer at the interface between silica and isotopically diluted water.

While a clear picture can be obtained from vSFG, the challenge of discerning information from SHG measurements persists. In Chapter 4, the sensitivity of SHG measurements is revealed by comparing experimental vSFG, SHG, and zeta potential measurements combined with hyperpolarizability computations. By using charge inversion phenomena at the silica/water interface induced by calcium ions in the aqueous phase, the contribution of the substrate can be elucidated in SHG measurements. We show that the hyperpolarizability of surface silanol sites increases significantly upon deprotonation. This computation suggests that the SHG is sensitive to the deprotonation of the silanol sites.

Chapter 2

Influence of the Excitation Wavelength on First Order Hyperpolarizabilities and Optimal Gap Tuning of Range Separated Hybrid Functionals

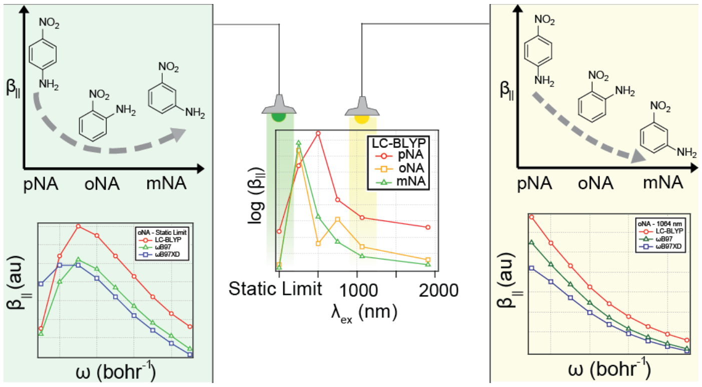

2.1 Introduction

Devices and techniques utilizing second-order nonlinear optical properties have found extensive applications in telecommunications and surface-sensitive characterization techniques.[131,174–176] Central to these applications is the magnitude of the first molecular hyperpolarizability, β_{ijk}, which is directly related to the extent of charge transfer within a system. The magnitude of the molecular hyperpolarizability can be determined via experimental routes, such as electric field-induced second harmonic generation (EFISH) and hyper-Rayleigh-scattering (HRS) experiments.[114,119,120] In these experiments, light with an excitation or fundamental wavelength (λ_{ex}) interacts with a species to yield an output with half the wavelength ($\frac{\lambda_{ex}}{2}$). Complementary to experimental measurements, over the last three decades, extensive computational work involving the use of various theoretical methods to predict the hyperpolarizability has been achieved.[121,138,177,178] The bulk of these studies have been accomplished at off-resonant excitation wavelengths. While it is known that the hyperpolarizability can be resonantly enhanced at the one-photon pole ($\lambda_{ex} = \Delta E$) and the two-photon pole ($2\lambda_{ex} = \Delta E$), it is unclear how the underlying charge transfer characteristics of a system would behave in these resonance regimes.

A commonly used reference system in previous studies is the push-pull π-conjugated molecule, para-nitroaniline (pNA), which has been thoroughly investigated experimentally and computationally.[114,130,132,135,172,179–184] Compared to meta (mNA) and ortho (oNA) nitroaniline isomers (Figure 2.1), it displays a remarkably larger hyperpolarizability as shown in both EFISH and HRS experiments at off resonant excitation wavelengths (λ_{ex} =1064 nm and 1907 nm), which consequently led to determining the hyperpolarizability trend of pNA>oNA>mNA.[112,114,117,118,185]

Early theoretical studies based on a two-state model attributed the trend to the intramolecular charge transfer between the donor (-NH_2) and acceptor (-NO_2) groups in the nitroaniline isomers, which has led to computational and experimental investigations into more push-pull type π-conjugated systems.[112,117,154,186]

The use of computational methods in the evaluation of both on and off resonant hyperpolarizabilities encounters challenges in reproducing the experimental measurements. Early computations involving the use of Hartree-Fock and semi-empirical methods were found to severely underestimate the hyperpolarizabilities relative to correlated methods based on coupled cluster and second-order Møller-Plesset perturbation theory (MP2).[141,143,144,161] Although the use of electron correlated methods has a profound effect on the accuracy of the hyperpolarizability, their practicality, computational cost, and convergence behavior, limit the widespread use of these methods in computations of hyperpolarizabilities.[187]

On the other hand, the use of density functional theory (DFT) provides an alternative route at a fraction of the computational cost. However, these methods are also susceptible to challenges in accurately predicting hyperpolarizability values, stemming from the choice of the exchange-correlation (XC) functional.[139,154] Hybrids and generalized gradient approximation (GGA) functionals poorly describe charge transfer excitations due to the wrong asymptotic behavior in the Coulomb operator.[145,146] To overcome this weakness, the concept of the range-separated hybrid functionals (RSH) was developed, where the Coulomb operator is partitioned into short- and long-range parts, using a standard error function.[153,188–190] Based on this formulation, a new variable called the range separation parameter, ω (or μ), is needed, which controls the switching between short-range and long-range behavior. An overall improvement is observed in the prediction of nonlinear optical properties of systems with RSH functionals relative to traditional

GGA functionals, however, the tendency to over or underestimate the properties relative to experimental studies persists.[191–194] An approach to improve the description of hyperpolarizabilities involves the optimization of the range separation parameter by a process known as nonempirical optimal gap tuning, which entails the enforcement of the molecule and its anion to obey Koopman's theorem.[167–169,171,195] However, due to the sensitivity to the environment, this approach has provided predictions with variable success relative to the experimental values and high-level ab initio computations.[172,193,196–198]

As such in this study, we utilize the known nitroaniline isomers' hyperpolarizability trend (pNA>oNA>mNA) as a means of qualitatively assessing the role of the excitation wavelength on the computation of hyperpolarizabilities. By computing the hyperpolarizabilities at different excitation wavelengths in addition to the static limit, we observe that the nitroanilines trend is not always maintained in on and off resonant conditions. For example, in the off-resonant and the two-photon absorption region (500-700 nm), the trend is maintained, however below this region and in the one photon region (250-350 nm) it is no longer maintained. Comparison to the damped two model suggests the resonance enhancement and possible presence of other states and false poles could dominate the charge transfer characteristics. Furthermore, we find that the previously identified pathological behavior associated with optimal gap tuning is wavelength dependent.

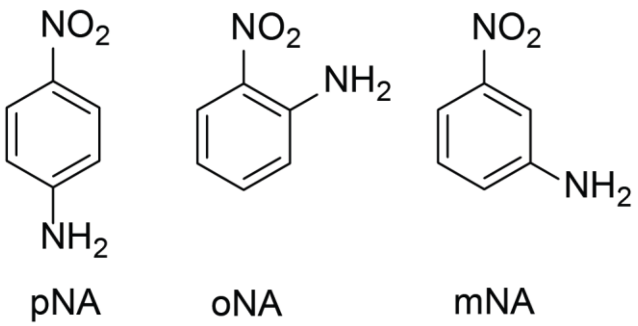

Figure 2.1: Structures of the nitroaniline isomers: para-nitroaniline (pNA), ortho-nitroaniline (oNA), and meta-nitroaniline (mNA).

2.2 Methods

Density functional theory (DFT) computations on the nitroaniline isomers (Figure 2.1) were carried out using the Gaussian 16 suite of programs,[199] while coupled cluster and time-dependent density functional theory (TDDFT) with damped response theory computations were done in Dalton 16.[200] The geometries of pNA, oNA, and mNA were optimized with CAM-B3LYP/6-31+G(d,p) using default convergence parameters.[201–207] The optimized geometries for each of the molecules are provided in the supplementary material.

First-order hyperpolarizabilities computed with DFT utilized the following functionals: B3LYP,[208] CAM-B3LYP,[201] ωB97XD,[209] ωB97,[210] and LC-BLYP[153] with the 6-311+G(d,p) basis set in both the gas and solvent phases. Additional TDDFT computations were done with the same basis set.[211] All solvent effects in DFT computations were accounted for with the polarizable continuum model (IEF-PCM).[212] Additional gas phase computations were done with second-order approximate coupled cluster (CC2), coupled cluster singles (CCS), and coupled cluster with single and doubles (CCSD), with the use of the frozen core approximation and the aug-cc-pVDZ basis set.[200,213,214] The range-separated hybrid functionals (RSH) were non-empirically tuned by setting the values of the range separation parameter (ω) with the internal options (IOps) for the anion, cation, and neutral species of the molecule in the gas phase.[167–169] Tuning was accomplished by minimizing the absolute difference (J^2) via

$$J^2(\omega) = [\epsilon_{HOMO}(N) + IP(N)]^2 + [\epsilon_{HOMO}(N+1) + IP(N+1)]^2, \qquad (2.1)$$

where IP refers to the ionization potential of the species (neutral = N electrons and anion = N+1 electrons) and ϵ_{HOMO} is the energy of the highest occupied molecular orbital of the corresponding species. To take solvation into account in optimal tuning studies, we utilize one of the approaches suggested by Kronik and Kümmel,[164] whereby optimal gap tuning is achieved in the gas phase and subsequent PCM is added using the ω value obtained in the gas phase. To avoid confusion in differentiating the range separation parameter, ω, and excitation energy (wavelength), we label the latter as λ_{ex}.

Hyperpolarizabilities are presented in the 'T' convention, which is based on the Taylor series expansion of the induced dipole moment, μ,

$$\mu(E) = \mu_i^o + \alpha_{ij}E + \beta_{ijk}EE + \gamma_{ijkl}EEE\ . \qquad (2.2)$$

In Equation 2.2, μ_i^o represents the permanent dipole moment, without the presence of the field E, α_{ij} is the polarizability, β_{ijk} is the first hyperpolarizability, and γ_{ijkl} is the second hyperpolarizability. The subscripts '*ijk*' and *'ijkl'* indicate that the hyperpolarizabilities are tensors with components defined in the molecular principal axis frame. The reported values, in atomic units (au), are the vector components of the hyperpolarizability which are parallel to the permanent dipole moment, $\beta_{||}$. This value is related to tensor components by

$$\beta_{||} = \frac{1}{5}\sum_i(\beta_{zii} + \beta_{izi} + \beta_{iiz})\ . \qquad (2.3)$$

For computations where the coordinate system does not align with the dipole moment, the value is given by[131]

$$\beta_{||} = \frac{1}{5}(\beta_x^2 + \beta_y^2 + \beta_z^2)^{1/2} \ , \tag{2.4}$$

where the components β_j are

$$\beta_j = \frac{1}{5}\sum_i(\beta_{jii} + \beta_{iji} + \beta_{iij}) \ . \tag{2.5}$$

For excitation energies near an electronic resonance, it has been shown that the hyperpolarizabilities should be determined through a damped two-state model (TSM). [127,128,135,215–218] In this model, the hyperpolarizability is given by

$$\beta_{ijk}(-2\omega;\omega_1,\omega_2) = P\ \sum_{m\neq 0}\sum_{n\neq 0}\left\{\frac{\langle 0|\mu_i|m\rangle\langle m|\overline{\mu_j}|n\rangle\langle n|\mu_k|0\rangle}{(\omega_{m0} + 2\omega - i\gamma)(\omega_{n0} - \omega_1 - i\gamma)} + \frac{\langle 0|\mu_k|m\rangle\langle m|\overline{\mu_j}|n\rangle\langle n|\mu_k|0\rangle}{(\omega_{m0} + \omega_2 + i\gamma)(\omega_{n0} - 2\omega + i\gamma)} + \frac{\langle 0|\mu_k|m\rangle\langle m|\overline{\mu_j}|n\rangle\langle n|\mu_j|0\rangle}{(\omega_{m0} + \omega_2 + i\gamma)(\omega_{n0} - \omega_1 - i\gamma)}\right\}, \tag{2.6}$$

where the term $\langle m|\bar{\mu}|n\rangle = \langle m|\mu|n\rangle - \langle 0|\mu|0\rangle$. In Equation 2.6, P is a permutation operator taking all the combinations into account, ω_{m0} is the excitation energy between the ground and *m*th state, $\langle n|\mu_k|0\rangle$ is the transition dipole moment between the ground and *n*th excited state, and γ is the damping parameter.

In the damped response theory, we compute the isotropic average hyperpolarizability based on the previous work,[135]

$$\bar{\beta} = \frac{1}{5}\sum_i(\beta_{zii} + 2\beta_{izi}) \ . \tag{2.7}$$

The inclusion of the relaxation results in complex hyperpolarizability values. Therefore, we present the absolute values. To facilitate a comparison between the computed and experimental values, experimental calibration and conversion factors were considered.[180,219] Details are provided in the supplementary material.

2.3 Results and Discussion

We begin the discussion by commenting on the influence of optimal gap tuning on the value of the range separation parameter (ω) of the range separated hybrid (RSH) functionals. The values were optimized in the gas phase, with $\pm$ 0.02 Bohr^{-1} accuracy, as shown in the plots of the absolute errors (J^2) versus ω in the supplementary material (Figure A1). Relative to the default values of the range separation parameter, optimal gap tuning significantly affects ωB97XD (ω = 0.33 to 0.20) as compared to LC-BLYP and ωB97 (ω = 0.33 to 0.28) for all the nitroaniline isomers. The values of ω for pNA closely match those predicted by the previous work done with different basis sets.[172,173]

With the tuned RSH functionals in hand, the gas phase hyperpolarizabilities at the static limit ($\lambda_{ex} = \infty$) and dynamic (λ_{ex}= 1064 nm) were computed, along with computations with B3LYP, CAM-B3LYP, CCS, CC2, and CCSD as presented in Table 2.1. Assessing the dynamic hyperpolarizabilities ($\beta_{||}^{1064nm}$) with the experimental hyperpolarizability trend (pNA > oNA > mNA), we find that the RSH functionals can reproduce the dynamic hyperpolarizability trend without optimal gap tuning being required. When assessing the hyperpolarizability trend predicted by the other methods, we find that B3LYP, CCS, and CAS/DZP,[184] are unable to reproduce the experimental trend. Although B3LYP provides a good approximation of pNA relative to the CCSD computation, it performs poorly for the other isomers. The tendency of B3LYP to predict well the hyperpolarizability of pNA, but under or over-estimate for other systems is well documented.[183] The failure of CCS is not surprising too, as previous studies done on pNA in the gas phase indicate that it will underestimate the static hyperpolarizabilities relative to CCSD computations, whereas CC2 will do the opposite.[183,187] As we show here, these behaviors associated with CCS and CC2 extend to the dynamic hyperpolarizabilities (λ_{ex} = 1064 nm) and the other nitroaniline isomers studied here.

Table 2.1: Gas phase static and dynamic hyperpolarizabilities (in au) of the nitroaniline isomers computed with DFT functionals and wave function theory-based methods with 6-311+G(d,p) and aug-cc-pVDZ basis sets, respectively. Optimally tuned RSH functionals are distinguished by an asterisk (*).

	pNA		**oNA**		**mNA**	
Method	$\beta_{\|\|}^{Static}$	$\beta_{\|\|}^{1064nm}$	$\beta_{\|\|}^{Static}$	$\beta_{\|\|}^{1064nm}$	$\beta_{\|\|}^{Static}$	$\beta_{\|\|}^{1064nm}$
B3LYP	908	1646	252	604	342	635
CAM-B3LYP	791	1274	271	543	285	437
ωB97XD	803	1271	279	526	298	449
ωB97XD*	789	1230	280	518	291	432
ωB97	725	1082	277	473	257	358
ωB97*	778	1230	280	539	282	419
LC-BLYP	739	1095	288	482	261	360
LC-BLYP*	827	1330	297	588	302	457
HF	518	710	197	287	168	222
CC2	1255	2025	325	586	359	533
CCS	581	779	185	247	204	272
CCSD	987	1495	291	476	311	438
CAS^{a}	805	1097	231	267	241	321
PM3^{b}	729	NR	116	NR	231	NR

^{a}*Static and dynamic hyperpolarizabilities ($\beta_{||}$) based on the use of complete active space and double zeta valence (DZV) basis set with polarization functions on all atoms from Ref.* [184]. *$\beta_{||}$ for the isomers are calculated using the individual tensor components provided and Equation 2.4.*

^{b}*Static hyperpolarizabilities from Ref.* [142]. *Dynamic hyperpolarizabilities not reported (NR).*

On the other hand, assessing the static hyperpolarizabilities, ($\beta_{||}^{Static}$), of the nitroaniline isomers, we find that CCSD/aug-cc-pVDZ computations indicate that the trend of the isomers does not follow the one predicted by experiments (pNA > oNA > mNA) instead the hyperpolarizability of mNA is greater than oNA where the trend becomes pNA > mNA > oNA. As a result, CC2, CCS, B3LYP, CAM-B3LYP, the previous CAS/DZP, PM3, and B3LYP/aug-cc-pVDZ computations done on the isomers follow this trend in the hyperpolarizabilities at the static limit.[130,142,184] The change in the hyperpolarizability trend suggests that the excitation wavelength plays a role in the computation of hyperpolarizabilities in off resonant conditions. This is surprising as it suggests that the underlying charge transfer characteristics of the nitroaniline isomers do not always persist.

The effect of optimal gap tuning becomes apparent at the static limit too, where the untuned RSH functionals ωB97 and LC-BLYP do not follow the static hyperpolarizability trend being predicted by the CCSD/aug-cc-pVDZ computations. However, after tuning the range separation parameter as described before, the functionals follow the trend predicted by the CCSD/aug-cc-pVDZ computation. We do note that tuning has a minimal influence on oNA at the static limit as compared to at 1064 nm, where for example ωB97XD changes by 1 au at the static limit compared to 7 au at 1064 nm. Nevertheless, this shows that optimal gap tuning is necessary to improve the description of static hyperpolarizabilities relative to CCSD/aug-cc-pVDZ computations.

To determine whether these changes in the hyperpolarizability trend persist in the presence of a solvent, we compare the computed hyperpolarizability trend to experimental studies determined at two excitation wavelengths ($\beta_{||}^{1064nm}$ & $\beta_{||}^{1907nm}$) which are in the presence of different media (Table 2.2).[112,114,185] The significant shift in the experimental hyperpolarizabilities at the different excitation wavelengths cannot be solely attributed to the change in the excitation wavelength. Previous work has highlighted the vibrational contributions, solvent effects and systematic errors associated with the experimental measurements can lead to different hyperpolarizabilities.[118,180,216,219,220] Nonetheless, all experiments show that the hyperpolarizability trend (pNA>oNA>mNA) persists at these off-resonant frequencies.

Table 2.2: Dynamic hyperpolarizabilities (in au) with excitation wavelength = 1064 nm and 1907 nm of the nitroaniline isomers computed with the default DFT functionals and optimally tuned functionals (distinguished by an asterisk (*)).

	pNA		**oNA**		**mNA**	
Method	$\beta_{\|\|}^{1064nm}$	$\beta_{\|\|}^{1907nm}$	$\beta_{\|\|}^{1064nm}$	$\beta_{\|\|}^{1907nm}$	$\beta_{\|\|}^{1064nm}$	$\beta_{\|\|}^{1907nm}$
Ref. [114a]	6112	-	1333	-	874	-
Ref. [112a]	5750	-	1417	-	833	-
Ref. [185b]	-	2162	-	521	-	396
B3LYP	4070	2131	1310	600	1959	801
CAM-B3LYP	3160	1785	1150	610	1035	616
ωB97XD	2919	1683	1106	591	971	592
ωB97XD*	2830	1645	1089	590	925	574
ωB97	2450	1476	991	568	727	487
ωB97*	2814	1629	1112	600	890	558
LC-BLYP	2508	1503	1018	586	731	490
LC-BLYP*	3111	1751	1220	639	986	601
HF	1594	1023	617	383	499	346

[a] *Experimental values of Levine and Bethea*[114] *as well as Oudar and Chemla*[112] *which measured pNA in methanol, and oNA/ mNA in acetone at* λ_{ex}*= 1064 nm.*

[b] *Experimental values were derived from Cheng et al.*[185] *where pNA was measured in acetone whereas mNA and oNA were measured in 1,4-dioxane at* λ_{ex} *= 1907 nm.*

At λ_{ex} = 1064 nm, several similarities to the gas phase computations of $\beta_{||}^{1064nm}$ can be found, where the traditional GGA functional B3LYP is the only functional unable to reproduce this trend as it overestimates the hyperpolarizability of mNA. Likewise, the need for optimal gap tuning is unnecessary at this excitation wavelength. On the other hand, at λ_{ex} = 1907 nm, B3LYP, CAM-B3LYP, and ωB97XD fail to reproduce the experimental trend. Although it is not surprising for B3LYP to fail to reproduce the experimental trend, it is surprising for CAM-

B3LYP and ωB97XD as they can do so at 1064 nm. Indeed, similar to the gas phase static hyperpolarizabilities, optimal gap tuning corrects the behavior of ωB97XD. Furthermore, tuning ωB97XD has a minimal effect on oNA at 1907 nm where the hyperpolarizability changes by 1 au as compared to a change of 17 au observed at 1064 nm.

The difference in the behavior of functionals at different excitation wavelengths indicates the role the excitation wavelength plays in both the prediction of hyperpolarizabilities and optimal gap tuning. To further investigate the first connection, the hyperpolarizabilities were computed at excitation wavelengths utilized by Ref. [179] in their experimental EFISH study conducted on pNA in 1,4 dioxane (experimental excitation wavelength dependent hyperpolarizabilities of mNA and oNA have not been determined). Adopting their excitation wavelengths, we evaluate the performance of the functionals with solvent effects of 1,4 dioxane (PCM) being considered. Figure 2.2(a) compares the $\beta_{||}$ of pNA computed at the wavelengths employed in the EFISH experiment. All the RSH functionals can reproduce the increment seen in the experimental hyperpolarizability of pNA with varying degrees of accuracy relative to the experiment. CAM-B3LYP and ωB97XD provide a closer approximation to the experimental values than ωB97 and LC-BLYP. The accuracy relative to the experiment is dependent on the excitation wavelength as the error significantly increases at shorter excitation wavelengths (higher energies).

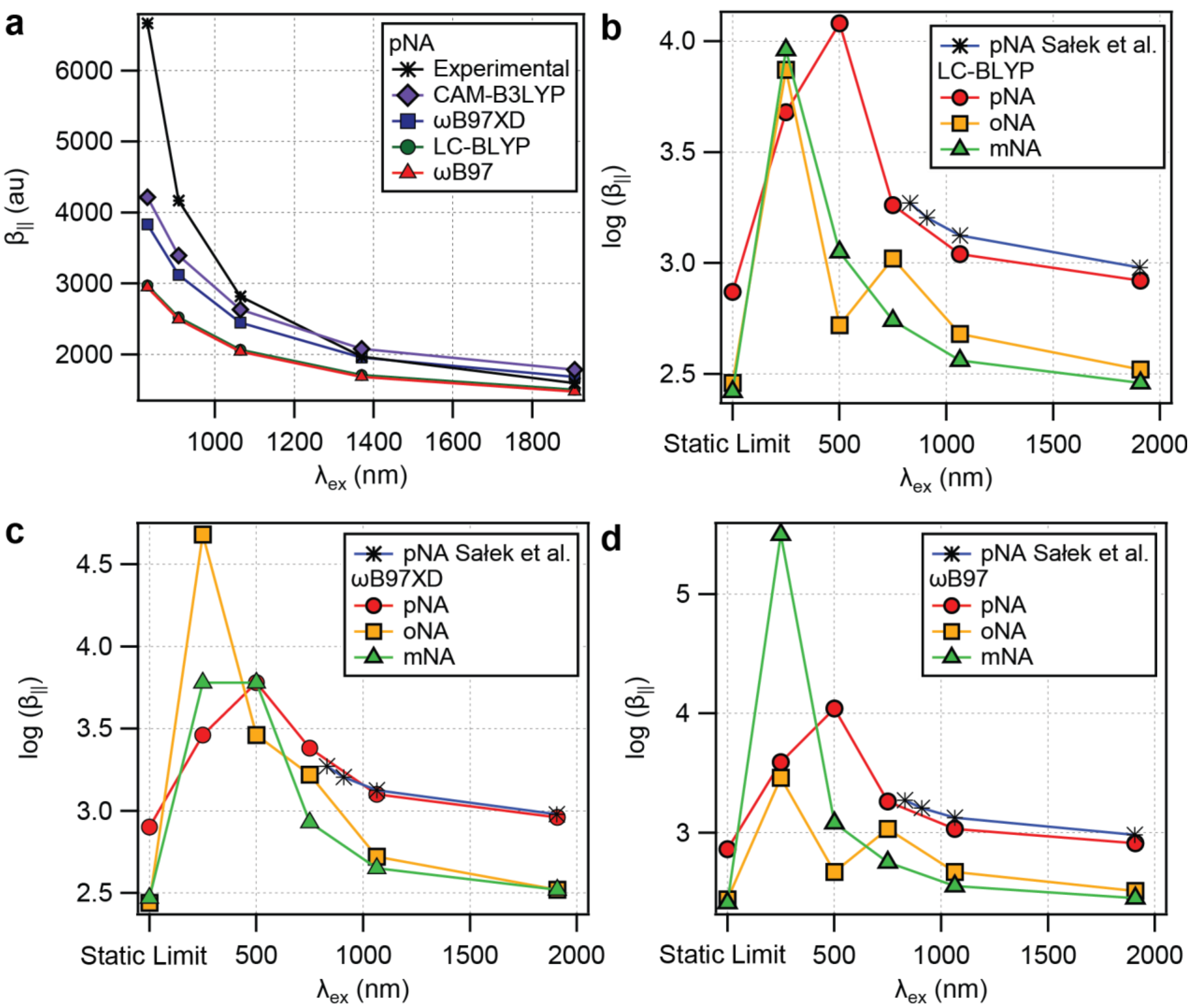

Figure 2.2: (a) Variation of the hyperpolarizability of pNA as a function of the excitation wavelength for all RSH functionals in comparison to experimental values.[179] Computations were done in 1,4 dioxane. Gas phase (b-d) logarithmic hyperpolarizability values of all isomers in a broader wavelength range from 1907 nm to the static limit. Additional gas phase CCSD/aug-cc-pVDZ computations on pNA from Sałek et al.[183] are presented too.

To obtain a qualitative picture of the excitation wavelength dependence, the gas phase hyperpolarizabilities were computed with RSH functionals over a wider excitation wavelength window (Figure 2.2(b-d)). Additional previous CCSD/aug-cc-pVDZ computations done by Sałek et al. are also included.[183] The hyperpolarizabilities of all the nitroaniline isomers significantly increase as the wavelength is lowered from 1907 nm to 750 nm. From 830 - 1907 nm, notably, the ωB97XD results provide a closer approximation to the previous CCSD/aug-cc-pVDZ values of pNA than ωB97 and LC-BLYP. In this region, all the default RSH functionals can reproduce the experimental hyperpolarizability trend. However, between 500 nm and the static limit, there is no consistency between the RSH functionals, as each gives different nitroaniline hyperpolarizability trends. We tentatively assign this enhancement of the hyperpolarizabilities to the presence of electronic resonances for all isomers. Indeed, TDDFT computations summarized in Table A2 confirm that the electronic resonances for the isomers lie between 250 - 350 nm. Moreover, the presence of the electronic resonance can explain the different nitroaniline trend predicted by the gas phase CCSD/aug-cc-pVDZ computations at the static limit. This change in the hyperpolarizability trend highlights the effect an electronic resonance can have on the computation of the hyperpolarizabilities.

We can shed light on the influence of electronic resonances by evaluating the hyperpolarizability in greater resolution by using the damped two-state model (TSM) in the near and on resonance regions. The damping parameter is set to 500 cm^{-1} based on previous work on pNA.[135] As shown in Figure 2.3(a), the damped two-state model predicts that all isomers show two distinct resonant centers or pole positions when the excitation energy is near a resonant contribution. The first region between 250-350 nm (labelled '(i)') is the one-photon resonance regime whereby the excitation energy is at resonance, while the second region between 500 – 700 nm (labelled '(ii)') is the two-photon resonance regime whereby the second harmonic energy overlaps with the resonant energy.[12,215]For pNA, these regions are in agreement with previous experimental and computational work.[221,222] We find that for both one and two photon resonance, and the region between them, the nitroanilines' hyperpolarizability trend is reproduced by the damped two-state model suggesting that the underlying donor-acceptor charge transfer characteristics significantly contribute to the hyperpolarizabilities.[112]

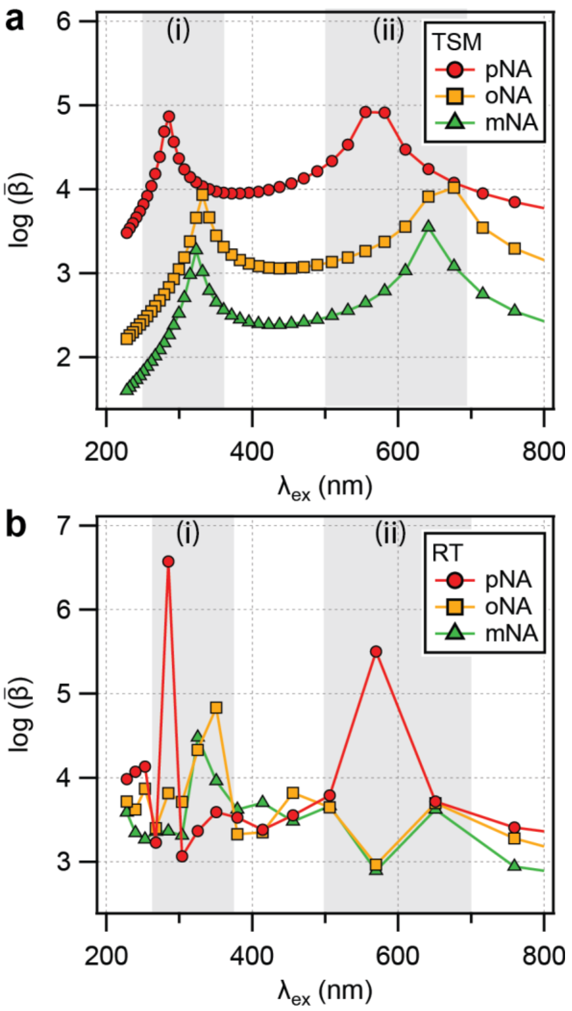

Figure 2.3: Hyperpolarizabilities determined using the (a) damped two-state model (TSM) and (b) damped response theory (RT). The value of the relaxation parameter is set to 500 cm^{-1} for both approaches. All computations are done with CAM-B3LYP/6-311+G(d,p) in the gas phase.

In Figure 2.3(b), we show the hyperpolarizabilities computed with damped response theory (RT). Similar to the TSM, the damping parameter (γ) is set to 500 cm^{-1}. In the two-photon resonance region (ii), we find that the hyperpolarizability trend is maintained. However, in two areas below this region (< 500 nm) the hyperpolarizability trend is not always maintained. Firstly, in the region between the one and two photon resonances, the trend is also broken, likely due to the damped two-state model (even with damping) not accounting for the additional electronic or vibronic states that can contribute to the hyperpolarizabilities in these regions.[216,223,224]

Secondly, in the one photon resonance region, a direct comparison of RT to the TSM (Figure A3), shows that while good agreement can be found in the prediction of one-photon pole positions for pNA and mNA, this is not the case for oNA. Such a shift in the pole positions between the RT and TSM has been identified for LiH. [218] This was linked to the prediction of an additional false pole by RT due to the shortcomings of the adiabatic approximation. Indeed, the variations in the occurrence of the shifts in the isomers suggest the presence of additional poles is highly system dependent, and thus the comparison to the damped two state model can serve as a good reference.

Next, we investigate the role the excitation wavelength plays in optimal gap tuning. The hyperpolarizabilities were computed over the experimental excitation wavelength range (830-1907 nm) with the tuned RSH functionals (Figure A2(a)). In comparison to the experimental values, tuning the RSH functionals over this wavelength range has a variable effect on the accuracy of the predicted hyperpolarizabilities in 1,4 dioxane.[179] The accuracy improves for LC-BLYP and ωB97 at 803, 909, and 1064 nm, however, reduces at 1907nm. In comparison to the gas phase CCSD/aug-cc-pVDZ computations done by Sałek et al.[183] on pNA, optimal gap tuning improves the prediction of the hyperpolarizabilities by ωB97 and LC-BLYP (Figure A2(b-d)). On the other hand, the opposite behavior takes place for ωB97XD, where the prediction improves at 1907 nm while becoming worse at the lower excitation wavelengths. For all the RSH functionals at the static limit and 1907 nm, tuning the functionals has a minimal effect on the hyperpolarizabilities of oNA.

The small change due to optimal gap tuning is interesting to note as this indicates that optimal gap tuning has a minimal influence on the hyperpolarizabilities of oNA. To explore these changes in oNA, we utilized the diagnostic test proposed by Scuseria and coworkers.[172] In this test, optimal gap tuning is effective when $\beta_{||}$ decays as the value of the range separation parameter (ω) increases. However, when this behavior is not followed, optimal gap tuning becomes less likely to improve the computed hyperpolarizabilities relative to experimental measurements. This approach was developed on pyrrole derivatives which displayed an increase in the $\beta_{||}$ values followed by a decrease as the value of ω was increased. Optimal gap tuning was found to have a minimal influence on the hyperpolarizabilities of these derivatives in comparison to that of pNA. Indeed, such behavior has been observed in other charge transfer systems.[198]

As a result, we present the plots of the $\beta_{||}$ of oNA as a function of ω at different excitation wavelengths in Figure 2.4. At the static limit and 1907 nm, all RSH functionals show that the $\beta_{||}$ rises initially followed by a decline as the value of ω increases (Figure 2.4 (a & c)). This behavior is similar to that found with the pyrrole derivatives and suggests that oNA represents a pathological case at the static limit and 1907 nm.[172] However, as shown in Figure 2.4(b), at 1064 nm a typical decay curve is observed indicating that the molecule is not the only contributing factor to this pathological behavior, but the choice of the excitation wavelength can also contribute and results in optimal gap tuning having a minimal effect on the hyperpolarizabilities. We do note that pNA and mNA exhibit typical behavior as the $\beta_{||}$ decays as ω increases for all the excitation wavelengths (Figure A4). Furthermore, the behavior of all the nitroaniline isomers observed in the gas phase extends to computations done in the solvent phase (1,4 dioxane) as well (Figure A5). Hence, setting the correct excitation wavelength is an important parameter when gauging the efficacy of optimal gap tuning in the prediction of hyperpolarizabilities.

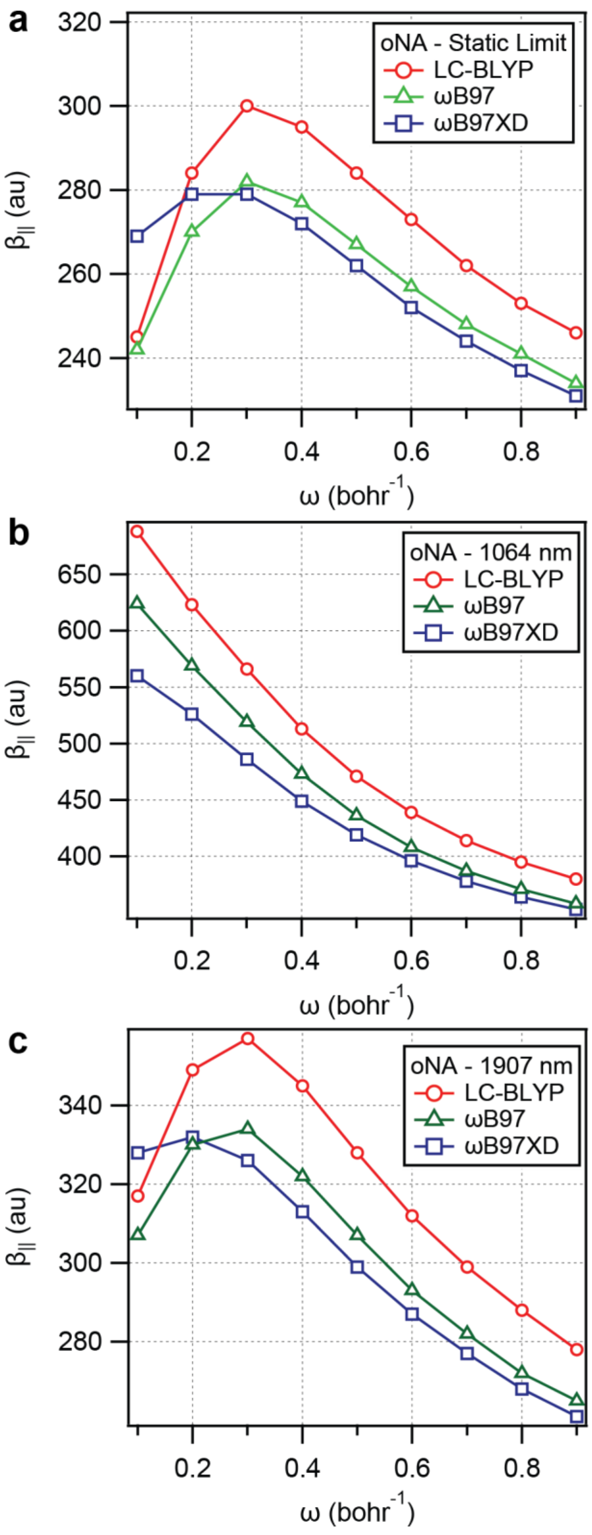

Figure 2.4: Variation of the hyperpolarizabilities of oNA with respect to the range separation parameter for RSH functionals at (a) the static limit (b) 1064 nm, and (c) 1907 nm in the gas phase. All computations used the 6-311+G(d,p) basis set.

2.4 Conclusions

In conclusion, the hyperpolarizabilities of para, ortho, and meta-nitroaniline were evaluated using DFT, including with optimally tuned range separated functionals, and coupled cluster calculations utilizing the charge transfer based hyperpolarizability trend (pNA > oNA > mNA) as a qualitative measure of accuracy. The excitation wavelength plays a pivotal role in the prediction of the hyperpolarizability trend as it is not always maintained, for example, CCSD/aug-cc-pVDZ computations at the static limit. Monitoring the hyperpolarizabilities over a wider excitation wavelength range with damped response theory indicates near the one-photon resonance region the trend is broken. Comparison to the damped two-state model reveals that the underlying charge transfer characteristics of the isomers are compromised by the presence of additional states or false poles in the one photon resonance region. The role of the excitation wavelength is also apparent in the optimal gap tuning process, where oNA exhibits pathological behavior which makes optimal gap tuning ineffective at 1907 nm and the static limit, but it reverts to the typical behavior at 1064 nm. These findings highlight that the excitation wavelength is an important factor to consider in both gas phase and solvent phase computations of hyperpolarizabilities and optimal gap tuning of RSH functionals.

Chapter 3

Influence of the Hydrogen Bonding Environment on Vibrational Coupling in the Electrical Double Layer at the Silica/Aqueous Interface

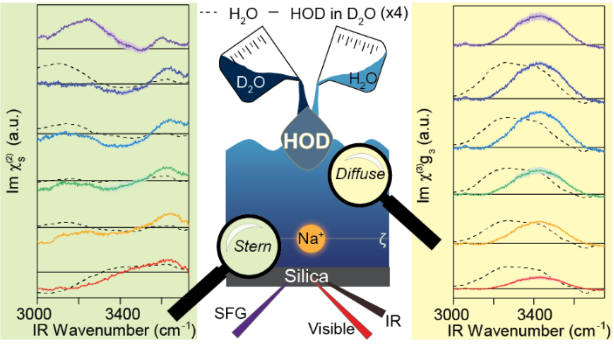

Portions of this chapter are reproduced with permission from the American Chemical Society (ACS)

"Influence of the Hydrogen Bonding Environment on Vibrational Coupling in the Electrical Double Layer at the Silica/Aqueous Interface" **Parshotam, S.**; Rehl, B.; Busse, F.; Brown, A.; Gibbs, J.M. *J. Phys. Chem. C* **2022**, 126, 51, 21734-21744

3.1 Introduction

The electrical double layer (EDL) represents a fundamental model of the interaction between a charged surface and the aqueous phase and, accordingly, is of central relevance to modeling both natural and engineered systems.[51] Information on the electrical double layer has been obtained using a wide variety of methods such as atomic force measurements (AFM),[225] X-ray spectroscopies using synchrotron light sources,[9,226] electrokinetic measurements,[11] and nonlinear optical techniques.[28,30] The underlying features determined from these measurements are strongly influenced by the sensitivity of the technique to the constituents of the EDL. For example, electrokinetic measurements give valuable information on the electric potential at the slipping plane of the EDL. However, the dominant constituent in the EDL is H_2O molecules, and their interactions with each other, ions, and the charged surface play critical roles in modulating the EDL structure and dynamics.

Vibrational sum frequency generation (vSFG) is an ideal technique to probe H_2O molecules in the EDL, as it is intrinsically sensitive to the number and order of the molecules at the surface allowing information such as the hydrogen bonding environment to be characterized.[27,30] However, for charged surfaces, such as the silica/H_2O interface, constructing a molecular picture is hindered by the presence of the electric field generated by the presence of charges due to deprotonation of silanol groups at pH values above ~2,[1,43] which align bulk water molecules. As vSFG is sensitive to the entire EDL, it is difficult to determine the contributions of H_2O molecules near the surface (i.e., in the Stern,[44,227] bonded interfacial,[64,91,93] or topmost layer[92]) and those contributing further away in the diffuse layer.

Several strategies have been applied to access the Stern layer spectral contributions at aqueous mineral oxide interfaces, such as suppressing the diffuse layer by employing a gate-controlled semiconductor/oxide/water junction[93] or by raising the ionic strength.[92,97] Most relevant to this work, Wen et al.[64] presented a route for separating the diffuse layer spectrum from the total EDL spectrum for water molecules interacting with a Langmuir-Blodget film without diffuse layer suppression by taking the difference between two vSFG complex spectra with similar surface charge densities and accounting for changes in electric potential. By uncovering the diffuse layer complex spectrum, the imaginary component of the Stern layer complex spectrum could be predicted, which is primarily of interest when constructing a molecular description of the interface. In our previous work, we modified this approach by utilizing zeta (ζ) potentials from either streaming current or potential measurements in combination with the maximum entropy method to deconvolute the Stern and diffuse layer spectra as the ionic strength and pH were varied at the silica/H_2O interface.[44,69]

However, for the silica/H_2O interface, the Stern and diffuse layer spectra are intricately tied to the intra- and inter-molecular vibrational coupling of H_2O. Intramolecular coupling between the bending overtone with the fundamental O-H stretch mode leads to a Fermi resonance characterized by the 3200 cm^{-1} mode in the vSFG spectrum.[78,103,104] This Fermi resonance significantly complicates the spectral interpretation making it difficult to relate spectral changes to changes in the intermolecular resonant coupling (i.e., structural changes) between neighboring H_2O molecules. Moreover, the strength of the hydrogen bonding interactions of the H_2O (manifested in the position of the resonant frequency) is also obscured. Both of these forms of coupling can be minimized by using isotopically diluted H_2O (HOD in D_2O).[105,228,229] Removing intramolecular coupling results in the absence of the Fermi resonance and hence its contribution to the spectrum at 3200 cm^{-1}. Meanwhile, the absence of intermolecular resonant coupling leads to the narrowing and blue shift of the OH stretch. [228,230]

Isotopically diluted H_2O has been extensively utilized in vSFG studies at several interfaces.[78,92,103,104,231–236] In particular, Tahara and co-workers[92] used it in their phase-sensitive vSFG experiments where they suppressed the diffuse layer contribution by increasing the ionic strength up to 5 M at a single pH of 12 at the silica/H_2O and silica/HOD interfaces. This work allowed them to identify Stern and diffuse layer spectra (labeled as the $\chi^{(2)}_{\mathrm{topmost}}$ and $\chi^{(2)}_{\mathrm{EDL}}$ spectra, respectively) at pH 12. They found a remarkable similarity between the Stern layer spectra of HOD and H_2O at pH 12 and high ionic strength indicating that H_2O molecules at the silica interface were vibrationally decoupled under these conditions. However, owing to the nature of these experiments, the influence of the ions and pH on the EDL could not be deconvoluted although both are known to strongly influence the structure of H_2O in the EDL.[44,48,69,86,237,238] Furthermore, as we have shown previously, the structure of H_2O in the Stern layer changes significantly as the pH is lowered below 12.[69]

We now expand our previous studies at the silica/H_2O interface by studying the silica/HOD (HOD in D_2O) interface in a bid to uncover the role vibrational coupling plays in the H_2O spectra of the Stern layer over varied surface charge densities beyond the measurements reported in Urashima et al.[92] We achieve this objective by measuring the vSFG spectra and zeta potentials at the silica/HOD interface with varying pH at constant ionic strength and varying ionic strength at constant pH. Using the maximum entropy method and Wen et al.'s approach, we can deconvolute the responses of the Stern and diffuse layers. We find strong similarities in the Stern layer spectral shape between HOD and H_2O at the silica interface at all pH values. However, we find that the evolution of the Stern layer of HOD as the pH is varied closely matches the pKa of out-of-plane silanols predicted by molecular dynamic simulations.[89,239] This is in contrast to water, suggesting that the presence of intramolecular coupling in the Stern layer spectra of water may distort the spectral response. Furthermore, at pH 2, the resonant frequencies of HOD in the Stern layer are blue-shifted with respect to those observed for H_2O. These differences in the frequency centers suggest that intermolecular resonant coupling becomes prominent at lower pH values. The source of the coupling could potentially be the change in the hydrogen bonding environment of H_2O from a singly hydrogen bond donating structure (asymmetric) to a doubly hydrogen bond donating structure with other H_2O molecules owing to a flip in the H_2O orientation near the silica surface as the pH is lowered.

3.2 Methods

3.2.1 Materials

IR-grade fused silica hemispheres (Almaz optics, KI, 1 inch diameter) were used for vSFG experiments. IR-grade fused silica windows (Almaz optics, KI, 2.5 inch diameter, 8 mm thickness) were used for zeta potential measurements. Silica substrates were cleaned with HPLC grade methanol (Fisher Chemical), sulfuric acid (95-98 %, Caledon Laboratories), and hydrogen peroxide (30 % w/w in H_2O, Sigma-Aldrich). Solutions were made with NaCl (99.99%, trace metal basis, Alfa Aesar), KCl (99.999%, trace metal basis, Acros Organics), NaOH (99.99%, trace metal basis, Sigma Aldrich), and HCl (34-37%, trace metal grade, Fisher Chemicals). Ultrapure deionized H_2O (18.2 MΩcm) was used during all experiments. Deuterium oxide (99.9% D, Sigma Aldrich) was utilized in conjunction with H_2O in the ratio of 4:1 (D_2O: H_2O) to yield mixtures in the ratio of 1:8:16 (H_2O: HOD: D_2O).

3.2.2 Sample Preparation

Before vSFG or zeta potential measurements, silica substrates were rinsed and sonicated for 5 min each in deionized H_2O, HPLC grade methanol, and then with deionized H_2O again before being immersed in piranha solution (3:1 H_2SO_4:H_2O_2) for 1 hr. The substrate was rinsed and sonicated in the same manner as before followed by drying in an oven (>100°C) for 15 min. For vSFG experiments, an in-house Teflon sample cell was rinsed and sonicated in deionized H_2O, MeOH, and deionized H_2O. The cell was then allowed to sit open to the atmosphere. HOD solutions were prepared using a ratio of 1:4 (H_2O: D_2O). To convert the measured pH values of HOD in D_2O to pD values we add 0.32 to the measured pH. However, for convenience sake, we refer to pD for D_2O as pH as we directly compare the pD and pH values between HOD in D_2O and H_2O, respectively.[78,240,241]

Caution: Piranha solution reacts violently with organic material. Ensure there is no residual methanol on the substrate before immersion in piranha.

3.2.3 Laser Assembly

A regeneratively amplified laser (Spectra-Physics, Spitfire Pro, 1 kHz, 94 fs, 3.3 W) was seeded and pumped by a Ti-sapphire oscillator (Spectra-Physics, MaiTai, 80 MHz) and Nd-YLF laser (Spectra-Physics, Empower 30), respectively, to generate 800 nm pulses. A 65% beam splitter (Newport) directed the 800-nm pulse to a noncollinear optical parametric amplifier (TOPAS-C/nDFG, Light Conversion) to produce tunable broadband IR pulses. The IR light was passed through a long pass filter (Edmund Optics, 2.40 m, 68-653), polarizer (Thorlabs), a zero-order, tunable half waveplate (Alphalas), and then a CaF_2 focusing lens (Thorlabs, f= 500 mm) focused the IR light to the sample. The remaining 800 nm light from the Spitfire Pro was passed through an air-spaced Fabry Perot Etalon (TecOptics), polarizer (Thorlabs), zero-order half waveplate (Thorlabs), and then a focusing lens (Thorlabs, f=500 mm) which directs the light to the sample. Both the visible and IR beams were spatially and temporally overlapped at the sample interface to generate sum frequency (SF) light. The SF light went through a BK7 recollimating lens (Thorlabs, f = 400 mm), a half-wave plate (Thorlabs), a Glan-Thompson calcite polarizer (Thorlabs), a focusing lens (Thorlabs), and a filter (Thorlabs) before entering a spectrograph (Princeton Instruments, Acton SP-2556, 600 grooves/mm grating) connected to a thermoelectrically cooled (-75 °C) charge-coupled device camera (Princeton Instruments, PIXIS 100B). A scheme of the setup is given below.

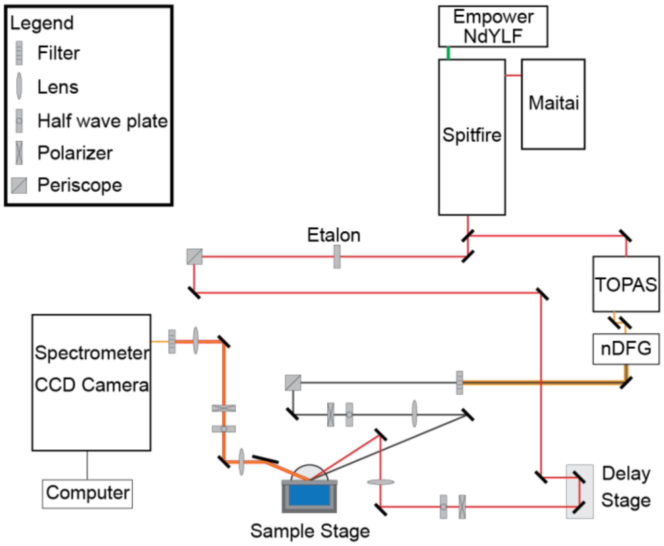

Figure 3.1: Overview of the optical setup for the measurement of vibrational sum frequency generation spectra at silica/aqueous interface.

3.2.4 vSFG Experiments

The laser was aligned and optimized using the sum frequency light generated from the silica/gold interface. A polystyrene calibration film (International Crystal Laboratories) was utilized to calibrate the detected frequencies. The gold coated hemisphere was replaced with the cleaned silica hemisphere. Before any measurement, the cell was thoroughly rinsed with the solution to be measured. For pH titrations, each solution was allowed to equilibrate before the spectral acquisition. The order of the solutions was H_2O (30 mins equilibration), 10 mM NaCl/water, and 50 mM NaCl/HOD. The pH of the 50 mM NaCl/HOD solution was adjusted using NaOH to reach pH ~10 and HCl was used to titrate from pH 10 to 2. For measurements involving the variation of the ionic strength, an initial volume of HOD solution was placed into the clean cell. By adding specific volumes of concentrated NaCl stock solutions, the desired concentration was achieved. Spectra obtained were divided by that from the silica/gold interface which was utilized as the reference. To facilitate a comparison between H_2O and HOD, the (S-polarized SFG, S-polarized visible, and P-polarized IR) spectra were normalized to the 3200 cm^{-1} mode intensity measurement at the silica/10 mM NaCl water interface. Details on the local field corrections are provided in Appendix B, with the resultant spectra presented in Figure B1.

3.2.5 Zeta Potential Experiments

Electrokinetic measurements were performed on a SurPASS Electrokinetic Analyzer (Anton Paar) using a clamping cell with spacers and sealing foil. The conductivity probe (Anton Paar, 18116) and pH probe (Anton Paar) were calibrated with 0.1 M KCl solution, and pH 4, 7, and 10 buffer solutions before every experiment. Prior to the clamping cell being mounted, the instrument was cleaned with deionized H_2O 5 times (300 s for each cleaning cycle). The clamping cell was mounted with two fused silica windows, with one of the plates with 2 holes to allow a channel to be formed between the 2 fused silica windows. The instrument was filled with deionized H_2O (200s) and a flow check was performed (500 mBar) to ensure no leakages in the channel. The instrument was then rinsed with deionized H_2O (500 mBar for 500 s), allowed to equilibrate for at least 30 mins, and then the zeta potential of H_2O was determined. The H_2O was then removed, and air passed through the instrument several times. HOD was then passed through the instrument with similar equilibration times as H_2O. Higher salt concentrations were used to dilute the HOD to obtain the zeta potential as a function of the ionic strength. Measurements were performed under streaming current mode with a rinse pressure of 500 mBar for 180s and ramp pressure of 400 mBar for 20s. For the pH titration, 50 mM NaCl/HOD solution was allowed to equilibrate, the pH was adjusted to 10 with NaOH diluted in 50 mM HOD, and then HCl was used to adjust the pH of the solution. The zeta potential was determined using the Helmholtz-Smoluchowski equation given by

$$\boldsymbol{\zeta = \frac{dI}{dP} \times \frac{\eta}{\varepsilon_o \varepsilon} \times \frac{L}{A}}. \tag{3.1}$$

where $\frac{dI}{dP}$ denotes the streaming current, η is the viscosity, ε is the dielectric constant, L is the length of the channel, and A is the area.[46]

To account for the differences in the viscosity and dielectric constant between HOD and H_2O, the values of 0.99 mPas and 78.23 were used for HOD while 0.89 mPas and 78.4 were used for H_2O.[242–244] A weighted average of D_2O and H_2O was used for HOD at 25°C.

3.2.6 Maximum Entropy Method Analysis

A more detailed version of the maximum entropy method (MEM) analysis can be found in previous vSFG work.[245–247] In brief, the maximum entropy method approximates the complex spectra from the intensity spectra. The spectral entropy, h, is given by

$$h \propto \int_0^1 log I(v) dv \,. \tag{3.2}$$

where $I(v)$ is the intensity spectrum and v is the rescaled frequency range from 0 to 1. Constraining the entropy to maximum and forbidding the growth of resonances over time, Lagrange multipliers give

$$I(v) = \frac{|b|^2}{\left|1+\sum_{m=1}^{M} \quad a_m e^{i2\pi m v}\right|^2} \,. \tag{3.3}$$

where the coefficients a_m and b can be determined from the Toeplitz system of equations for 2M+1 data points. The Toeplitz system of equations is

$$\begin{bmatrix} R(0) & \cdots & R(-M) \\ \vdots & \ddots & \vdots \\ R(M) & \cdots & R(0) \end{bmatrix} \begin{pmatrix} 1 \\ a_1 \\ \vdots \\ a_M \end{pmatrix} = \begin{pmatrix} |b|^2 \\ 0 \\ \vdots \\ 0 \end{pmatrix}. \tag{3.4}$$

where *R(m)* is the autocorrelation function given by

$$R(m) = \int_0^1 I(v) e^{-i2\pi m v}\, dv\ . \tag{3.5}$$

The complex-valued $\chi^{(2)}$ can be determined by

$$\chi^{(2)}(v) = \frac{b e^{i\varphi(v)}}{1+\sum_{m=1}^{M} \ a_m e^{i2\pi m v}}\ . \tag{3.6}$$

In Equation 3.6, the numerator is the frequency-dependent error phase, while the inverse of the denominator is the MEM complex spectrum. The unknown error phase is required to determine the actual phase (i.e., $\chi^{(2)}$ phase) of the vSFG spectrum ($\varphi(v)$) from the MEM phase, whereby

$$\chi^{(2)}\, phase \ = \ Error\, phase \ + \ MEM\, phase. \tag{3.7}$$

3.3 Results and Discussion

3.3.1 Homodyne vSFG and Zeta Potentials

Broadband vibrational sum frequency generation (vSFG) involves the spatial and temporal overlap of a broadband IR light field and a narrow visible light field, which generates an intensity spectrum at the sum of the incident field frequencies. Owing to resonant enhancement, the spectra are sensitive to the molecules with vibrational modes that are vSFG active and excited by the incident IR.[248] Moreover, within the electric dipole approximation these molecules must be assembled non-centrosymmetrically to contribute to vSFG. The observed changes in the intensity of the sum frequency light can be described by the following equation:

$$I_{SF} \propto \left|\chi^{(2)}_{\text{total}}\right|^2 = \left|\chi_s^{(2)} + \chi^{(3)} g_3\right|^2. \tag{3.8}$$

Here $\chi_s^{(2)}$ is the second-order susceptibility that reports on molecules in the Stern layer,[91] and $\chi^{(3)}$ is the third-order nonlinear susceptibility which describes the SFG response of water in a bulk-like environment. The value of g_3 is determined from the interfacial potential, which we approximate by the zeta potential, and accounts for optical interference in the diffuse layer that occurs at low ionic strength.[65,67] This $\chi^{(3)}g_3$ term represents the contribution of H_2O or HOD molecules aligned or polarized by the interfacial potential, which is analogous to the diffuse layer component of the EDL.

To evaluate the vSFG responses of HOD and H_2O at the silica interface, we measured the SSP (S-polarized SFG, S-polarized visible, and P-polarized IR) and PPP intensity spectra in the O-H stretching region as the pH was varied and in the presence of 50 mM NaCl (Figure 3.2). Changing the pH alters the surface charge density of silica since the surface silanol groups are weak acids and become deprotonated as the pH is raised above 2, which is in the range of the point of zero charge of silica.[43] Changing the protonation state of the surface silanol sites should manifest in changes to both the Stern layer ($\chi_s^{(2)}$) and diffuse layer ($\chi^{(3)}g_3$) spectra. For example, in our previous work with H_2O at a constant ionic strength (50 mM NaCl), as the silica surface became less charged with decreasing pH from 10 to 2, the hydrogen bonding environment of the H_2O in the Stern layer evolved significantly, while the diffuse layer contribution decreased with the decreasing magnitude of the interfacial potential (g_3 term in Equation 3.8).[44]

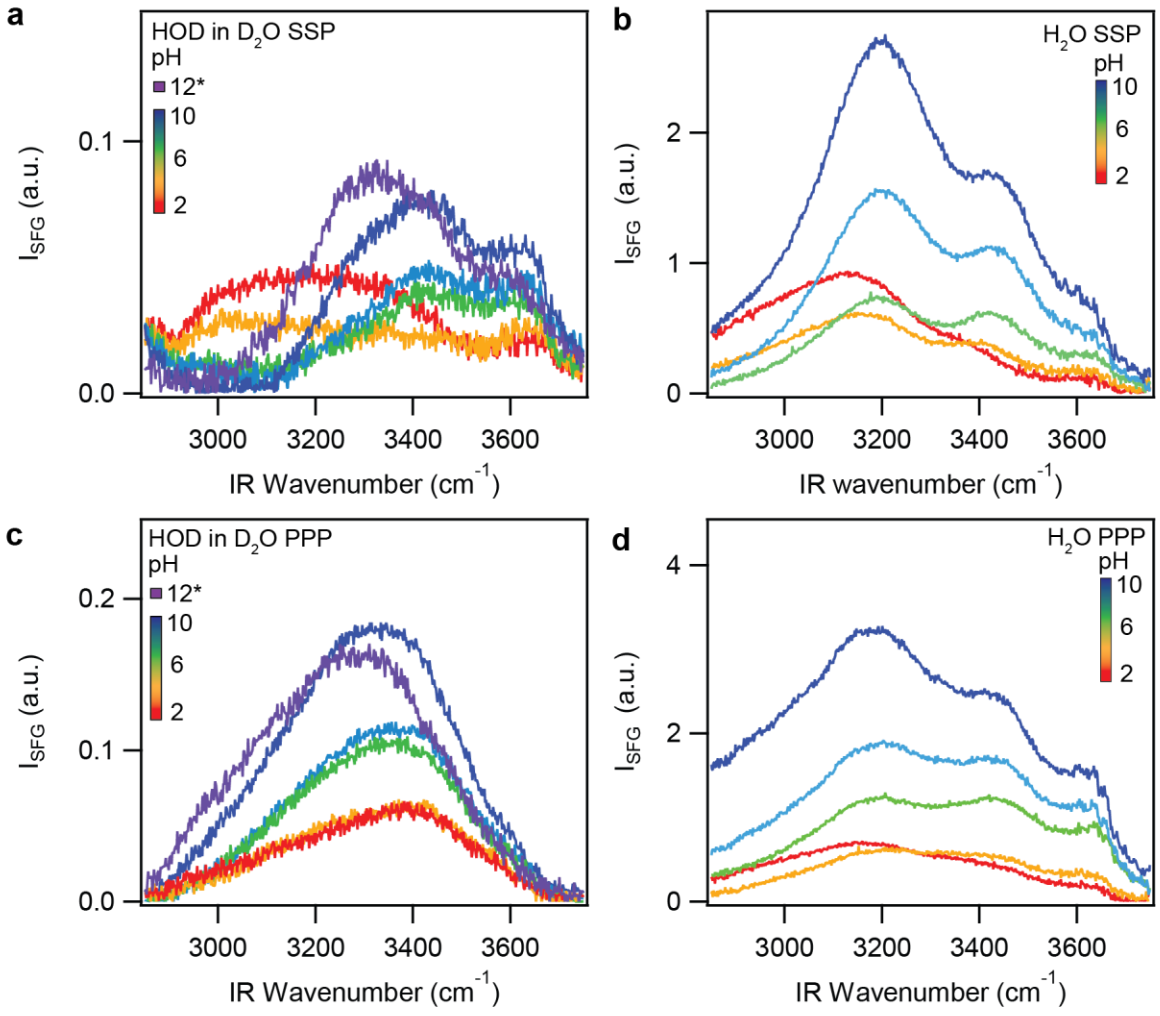

Figure 3.2: Representative SSP vSFG intensity spectra corrected for local field effects from 2850 to 3750 cm^{-1} at the (a) silica/HOD and (b) silica/H_2O interfaces[44] as the pH was varied from 10 to 2 with under a 50 mM NaCl background electrolyte. Representative PPP vSFG intensity spectra without local field corrections at the (c) silica/HOD and (d) silica/H_2O interfaces. To allow for comparison to previous work,[92] we also separately measured the SSP and PPP spectra at the pH 12 silica/HOD interface.

Consistent with previous work,[78] the SSP intensity spectra of the silica/HOD interface at natural pH (~pH 7 based on equilibrium with atmospheric CO_2) and 50 mM NaCl exhibited a broad peak at 3400 cm^{-1}, a narrower peak at 3600 cm^{-1}, and the tail of another mode below 3000 cm^{-1}. As the pH was decreased from pH 10 to pH 2, the 3400 cm^{-1} and 3600 cm^{-1} modes began to decrease while a new 3200 cm^{-1} mode increased in intensity, becoming most prominent at pH 2.

In contrast, the SSP spectra of silica/H_2O exhibited a feature in the intensity spectra at 3200 cm^{-1} over the entire pH range (Figure 3.2(b)).[44] Although there is expected to be a broad distribution of hydrogen-bonding environments at this hydrophilic interface,[103] the 3200 cm^{-1} mode for the H_2O spectra contains significant contributions from the Fermi resonance.[104] Yet the evolution of the spectral shape of H_2O based on variations in the intensity of the 3200 and 3400 cm^{-1} modes have been analyzed in previous work to obtain information on the interfacial structure of H_2O.[73,86,97,238]

The PPP spectra of the silica/HOD interface presented in Figure 3.2(c) display a vastly different spectral line shape and response to alterations in the pH than that of the SSP spectra. In this polarization combination, one symmetric broad peak centered at ~3300 cm^{-1} dominated the spectra at pH 10 and gradually became blue-shifted and asymmetric as the pH decreased. In a separate experiment, we measured the spectrum at pH 12, for comparison with the previous work[249] and found the spectral position was the most red-shifted at pH 12 consistent with the trend observed from pH 10 to 2. The variations observed at low pH in the SSP spectral shape did not appear in the PPP spectra as the pH was varied. This strong dependence on the polarization combination is in stark contrast to the SSP and PPP spectral shape from the silica/H_2O interface, presented in Figure 3.2(b & d), respectively, that exhibit the 3200 cm^{-1}, 3400 cm^{-1}, and 3600 cm^{-1} modes consistently throughout the pH range as well as the red-shift at low pH.

The difference between the polarization combinations for the HOD system is further exemplified by a comparison of the square root of the integrated area of the intensity spectra (proportional to $\chi^{(2)}_{\mathrm{total}}$) and the corresponding zeta potentials, which were determined for the same type of planar silica sample under the same experimental conditions (Figure 3.3). As shown in Figure 3.3(a), the PPP and SSP integrated areas of silica/HOD exhibit different pH-dependent trends: the integrated area of the PPP spectra follows the zeta potentials more closely than that from the SSP spectra where the former is more monotonic than the latter. Meanwhile, for the silica/H_2O system displayed in Figure 3.3(b), the integrated area exhibits a similar non-monotonic response for both PPP and SSP integrated areas over the pH range. We attribute this similarity between the PPP and SSP spectra and their pH-dependence to the contribution of the Fermi resonance to the diffuse layer spectra for the H_2O system, which contributes significantly to the spectral response at lower wavenumber (vide infra).

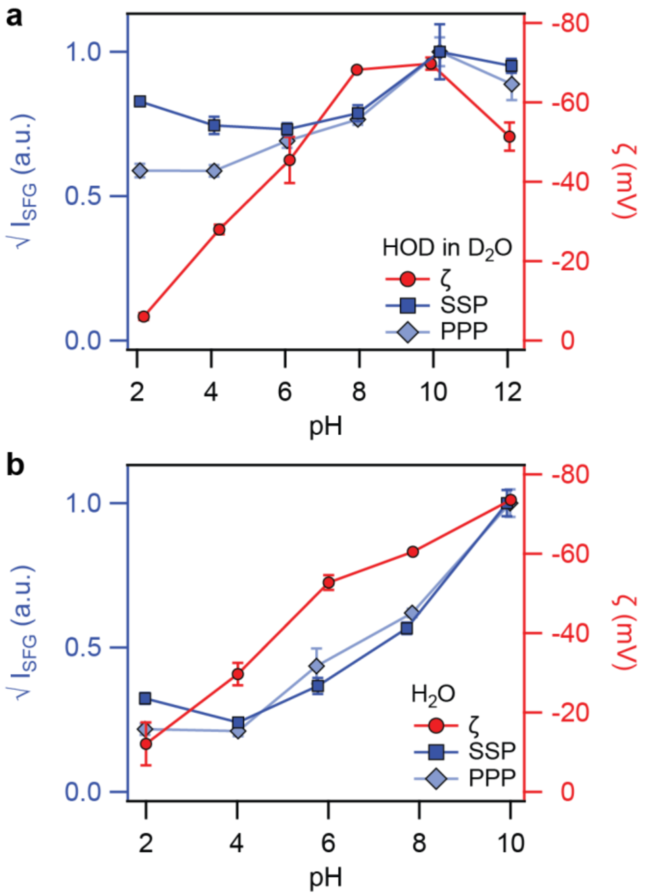

Figure 3.3: The square root of the average values of the integrated SSP (local field-corrected) and PPP spectra from 2850 to 3750 cm^{-1} (blue), normalized to the value at pH 10, and the corresponding zeta potentials (red) at the (a) silica/HOD and (b) silica/H_2O[44] interfaces collected from pH 10 to 2 with a background of 50 mM NaCl. Error bars are the standard deviation from replicate measurements.

To determine the diffuse layer component of the complex spectra, we rely on our reported methodology to determine the $\chi^{(3)}$ spectrum of HOD.[44,69] This methodology requires measuring the zeta potentials and the vSFG spectra as the ionic strength is varied at a constant pH. We present the vSFG spectra as the ionic strength was varied at the silica/HOD interface at natural pH in Figure 3.4(a). While the variation in the pH led to prominent shifts in the peak positions in the SSP spectra (Figure 3.2), particularly for the HOD interface, the influence of varying the ionic strength was less pronounced in both the H_2O and HOD spectra. Likewise, minimal changes in peak positions were observed in the PPP spectra (Figure B2). For both systems, the effect of increasing the ionic strength was most apparent in the intensities of the spectra. As the ionic strength was increased in H_2O or HOD in D_2O equilibrated with atmospheric CO_2, we observed an initial growth in intensity followed by a decrease in the SSP spectra in both systems. Such a trend has been previously reported and attributed to changes in optical interference within the diffuse layer as the ionic strength dependent Debye length approaches the coherence length followed by charge screening at higher salt concentrations.[63,67–69]

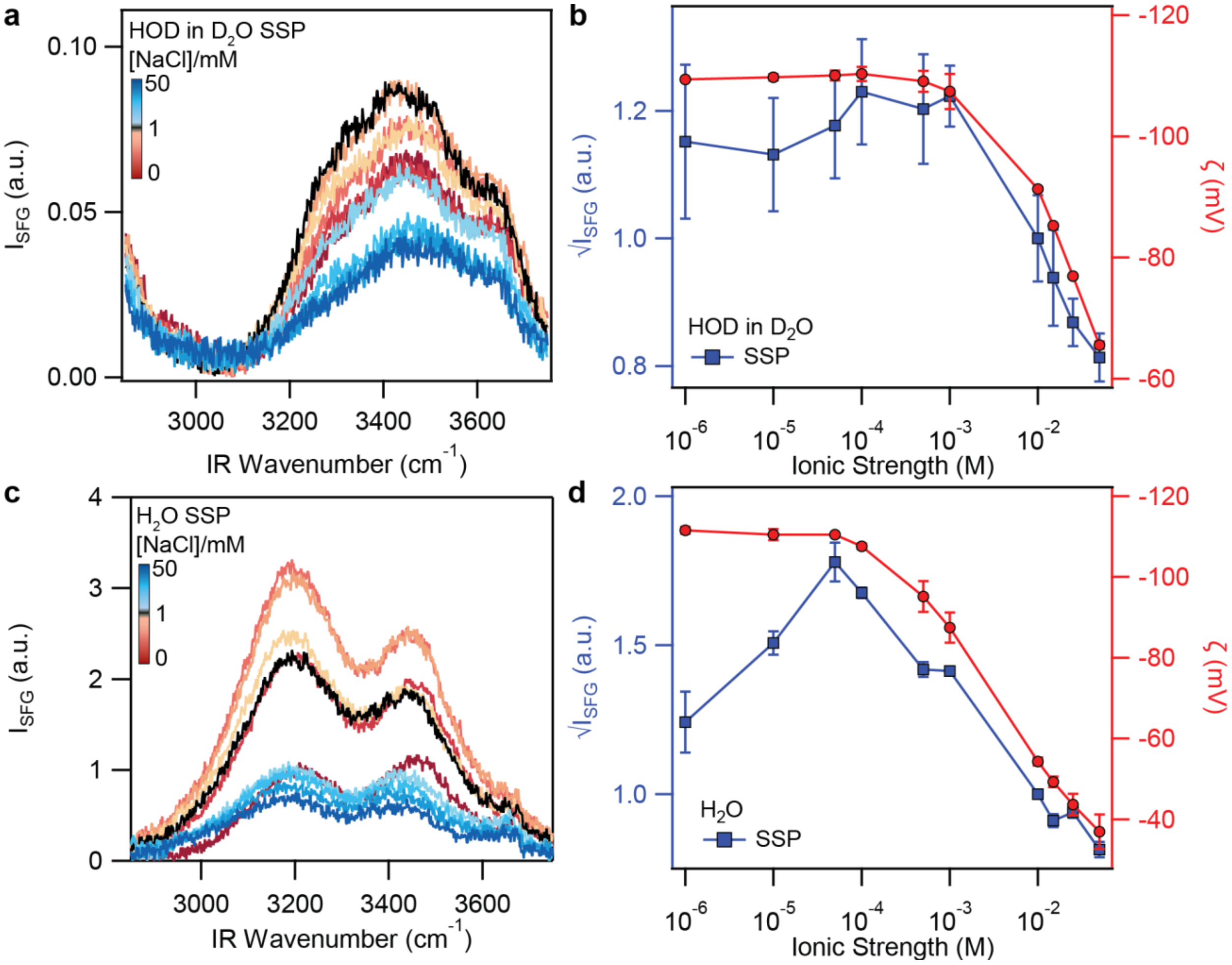

Figure 3.4: Representative SSP vSFG intensity spectra corrected for local field effects from 2850 to 3750 cm^{-1} and the accompanying average square root of the integrated spectral areas (blue squares) and average zeta potentials (red circles) at the (a-b) silica/HOD and (c-d) silica/H_2O interfaces collected from the neat (no added salt) solution to an ionic strength of 50 mM NaCl. Error bars are from the standard deviation of replicate measurements.

However, there is a difference in the salt-dependent trends of HOD and H_2O. For the silica/H_2O interface, the maximum intensity was observed at 0.05 mM NaCl, whereas for the HOD system, the maximum was observed for an ionic strength of 0.1 mM. This is also notable in the evolution of the corresponding zeta potential with ionic strength. Indeed, by computing the electrokinetic charge densities predicted by the Grahame equation,[45] we observed differences in the charge densities between HOD and H_2O with added salt (Figure B3). These differences warrant further investigations as previous work comparing D_2O and H_2O have found intrinsic variations between their properties.[250,251] For example, Roke and coworkers highlighted the changes in the affinity of ions towards silica when comparing H_2O and D_2O.[251]

3.3.2 Complex vSFG Spectra of HOD

Thus far, we have compared the intensity spectra ($\left|\chi_{total}^{(2)}\right|^2$) of the two interfaces. However, to deconvolute the contributions of the Stern ($\chi_s^{(2)}$) and diffuse ($\chi^{(3)} g_3$) layers from the overall intensity spectra, we need to determine the complex spectra, which we and others[64,91] refer to as $\chi_{\mathrm{total}}^{(2)}$. To obtain the SSP complex spectra from the intensity spectra presented in Figure 3.2 and Figure 3.4, we employ the maximum entropy method (MEM), which has been previously utilized in several vSFG studies.[245–247,252–258] The rising intensity at lower wavenumber (< 3000 cm^{-1}) in the SSP intensity spectra of HOD is attributed to the tail of the O-D stretches from D_2O. Therefore, to avoid any interferences from the O-D region, we truncate our spectra at 3000 cm^{-1} in the following analysis.

The MEM estimates the complex spectra from the intensity spectra by identifying the most probable phase under the constraint of maximizing spectral entropy and assuming no growth of resonances over time. The outcome of the analysis is the MEM complex spectra that can be separated into the amplitude and the 'MEM phase,' which is related to the actual phase (i.e., the $\chi^{(2)}$ phase) of the spectra (φ) by the so-called error phase as shown in Equation 3.7. In our previous work at the silica/neat H_2O interface,[44,69] we made use of the phase-sensitive vSFG measurements by Myalitsin et al.[78] to predict the error phase under specific conditions. Heterodyne second harmonic generation (HD-SHG)[72,81] was then used to predict changes in the error phase with varying pH or ionic strength conditions that were not previously acquired by phase-sensitive vSFG measurements. Under all these various conditions, the error phase remained linear with respect to the wavenumber.

3.3.2.1 Determination of the pH dependent complex spectra

For the HOD system, we use the complex spectra presented by Myalitsin et al.[78] and MEM analysis of their corresponding intensity spectra to determine the error phases at pH 2.1, 7.2, 12.1 and ionic strength of 10 mM phosphate buffer solution (PBS) as shown in Figure 3.5(a) (bold lines). Using MEM analysis of our intensity spectra and the error phase spectra from their data, our resulting imaginary spectra at pH 2 and pH 12 were in good agreement with their phase-sensitive vSFG measurements (Figure 3.5 (b)). Here the amplitude difference at pH 12 relative to pH 2 was likely due to the higher ionic strength in our system. However, we found that the error phase of HOD determined by Myalitsin et al.[78] is nonlinear with respect to wavenumber at pH 7 and is highly sensitive to variations in the pH. Furthermore, a shift in the error phase from HOD at natural pH with no added salt (which we estimate to be at pH 7.5) to pH 7 HOD (and 10 mM PBS) makes it difficult to decipher the influence of ions on the error phase (Figure B4). Therefore, we required new procedures to predict the error phase as the pH and ionic strength were varied. Below we describe the methodology we adopt to determine the complex spectra as a function of pH.

For the experiments performed with varying pH and a background of 50 mM NaCl, we interpolated at each wavenumber the error phase derived from the phase-sensitive vSFG measurements at pH 2.1, 7.2, and 12.1.[78] As shown by the dashed lines in Figure 3.5, this approach assumed for simplicity that the error phase with respect to each wavenumber varies linearly with the pH. The resultant complex spectra utilizing the interpolated error phases with the MEM analysis of our intensity spectra as the pH was varied are shown in Figure 3.5(c). The sign of the modes in the resulting imaginary spectra reflects the orientation of the O-H oscillators within the EDL.[96] Specifically, for the O-H oscillators, the positive sign indicates that the oscillator is pointing with the hydrogen atoms towards the silica surface, while a negative sign represents the opposite direction. The variation in the imaginary spectra of HOD mimics that of H_2O as at low pH there is a transition from negative to positive amplitude of the imaginary component of $\chi^{(2)}$ in the lower wavenumber region.[44,78]

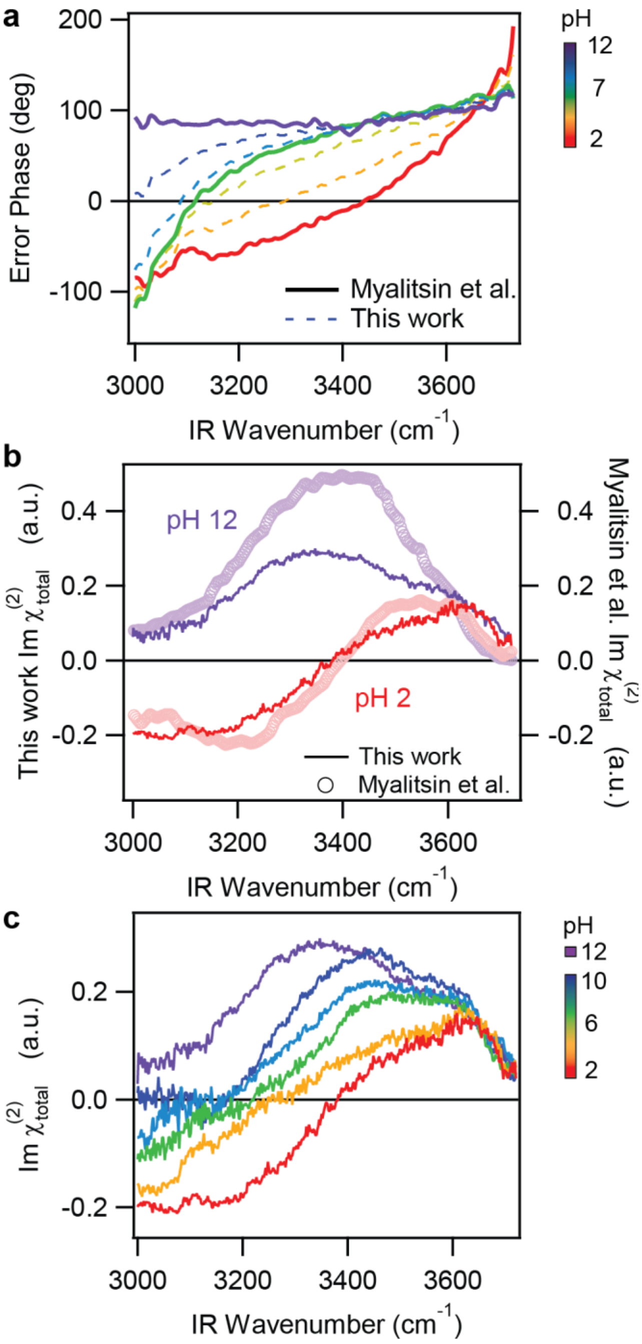

Figure 3.5: Complex spectra of the HOD-D_2O system. (a) The wave-number dependent error phase was extracted from Myalitsin et al.[78] (bold lines) and interpolated values at intermittent pH (dashed). (b) Comparison of the imaginary spectra at pH 2 and pH 12 measured by Myalitsin et al.[78] and those determined by the maximum entropy method analysis of our HOD-D_2O SF intensity spectra. (c) The imaginary spectra using the interpolated error phases and MEM analysis of our intensity spectra are presented in Figure 3.2(a).

3.3.2.2 Determination of the ionic strength dependent complex spectra

While the interpolation of the error phase shown above can be used to predict the complex spectra with varying pH and constant ionic strength. We cannot use this approach to predict the error phase as the ionic strength is varied because phase-sensitive vSFG measurements have only been reported at two different ionic strengths (neat and 10 mM PBS) at the silica/HOD interface, which does not adequately cover the range explored in our experiments (neat to 50 mM). Furthermore, as shown in Figure B4, the error phase between the two ionic strength points is nonlinear which makes it difficult to model.

However, for the phase-sensitive vSFG measurements with 10 mM PBS (pH 7) and neat HOD, we find that the $\chi^{(2)}$ phase (φ) is linear between 3000 and 3700 cm^{-1} Figure 3.6(a). Furthermore, by determining the MEM phase of these phase-sensitive measurements, we find three points where the $\chi^{(2)}$ phase could be predicted. Two of the points were when the MEM phase intersected the x-axis (i.e., MEM phase = 0). At these points, the φ phase is equal to the error phase, which we found was approximately 90° (-90° at low wavenumber and +90° at high wavenumber) as shown in Figure 3.6(a). The last point is where the slope of the MEM phase changed sign, which was observed to correspond to the point at which the φ phase was zero in these reference spectra.

If these three points are fit to a linear line, approximate values of the $\boldsymbol{\chi}^{(2)}$ phase can be predicted. As we note in Figure 3.6(b), the result of the fit is in close agreement to the $\boldsymbol{\chi}^{(2)}$ phase determined experimentally. With the fit of the $\boldsymbol{\chi}^{(2)}$ phase in hand, the real and imaginary components can be predicted too as shown in Figure 3.6(c). Likewise, the agreement to the experimentally measured complex spectrum is in good agreement.

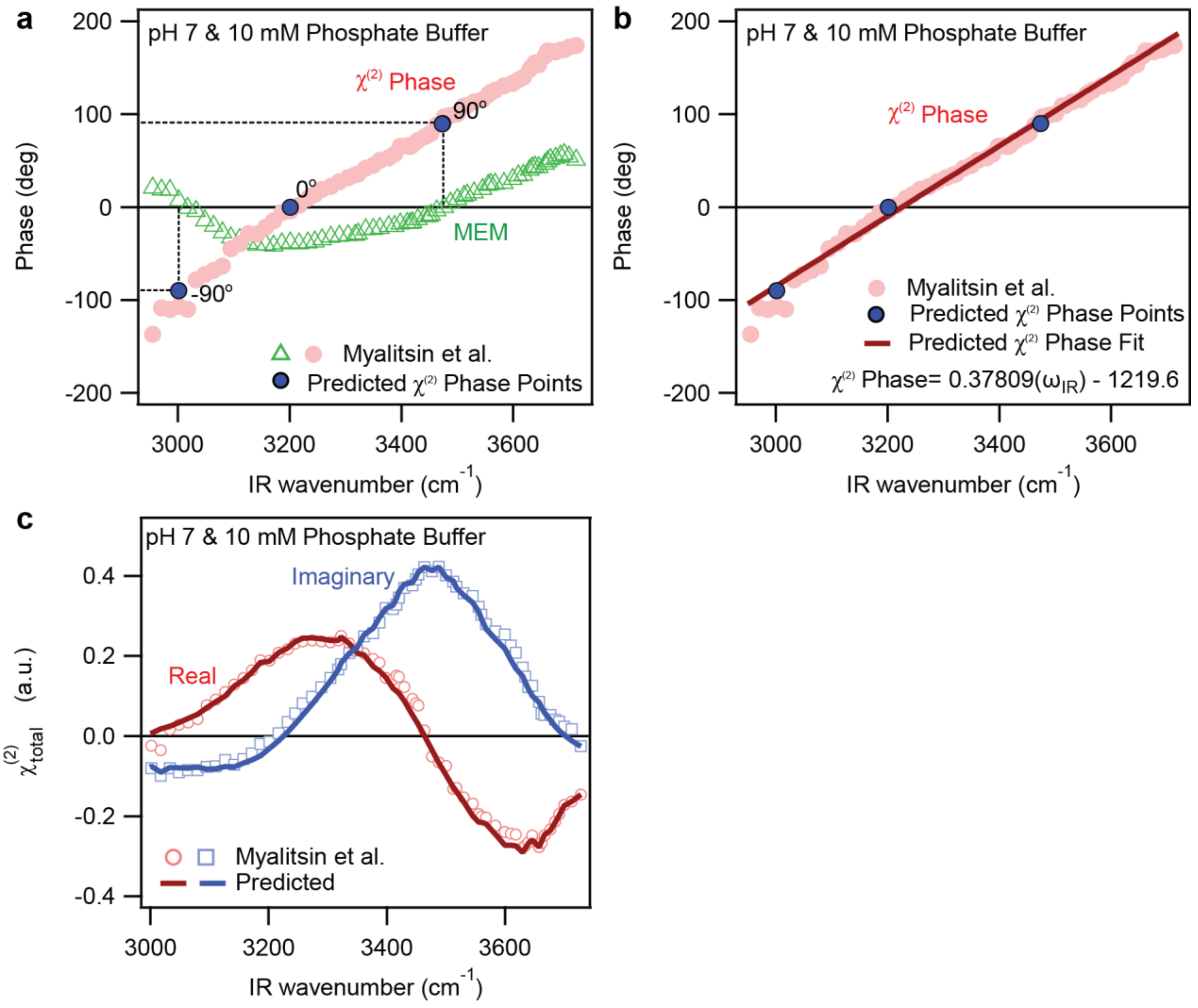

Figure 3.6: (a) The MEM phase of Myalitsin et al.[78] (green triangles) determined from the MEM analysis of their corresponding intensity spectrum. The red squares show the 3 predicted values of the absolute phase derived from the MEM phase of Myalitsin et al.[78] (b)The absolute phase (red line) determined from the linear fit of the 3 predicted values (red squares) in comparison to that of Myalitsin et al.[78] (peach circles). (c) Comparison of the predicted complex spectrum using the absolute phase linear fit to that reported by Myalitsin et al.[78]

As a result, the methodology we propose for predicting the complex spectra of HOD is based on (1) obtaining the MEM phase from the maximum entropy method analysis, (2) determining the three points from the MEM phase, (3) fitting the three points to a linear line to obtain the $\chi^{(2)}$ phase. and (4) using the $\chi^{(2)}$ phase to determine the complex spectra for the ionic strength range covered in this work. We apply this approach to our measured intensity spectra over the ionic range measured as presented in Figure B6 with the corresponding slope and intercept of the linear fits being presented in Figure B7(a & b). In Figure B7(c & d), we present the $\chi^{(2)}$ phase (φ) and error phase spectra determined over the ionic strength range.

In Figure 3.7, we compare our approach to Myalitsin et al.[78], where the $\chi^{(2)}$ phase (φ) at an ionic strength of 10 mM predicted from our MEM phase spectrum is shown in Figure 3.7(a) (red line), shows excellent agreement with the φ spectrum measured by Myalitsin et al.[78] (peach line). The complex spectra at an ionic strength of 10 mM determined from this method of analysis are in good agreement with the phase-sensitive vSFG measurements as presented in Figure 3.7(b). The imaginary component of the complex spectra over the ionic strength range studied is presented in Figure 3.7(c).

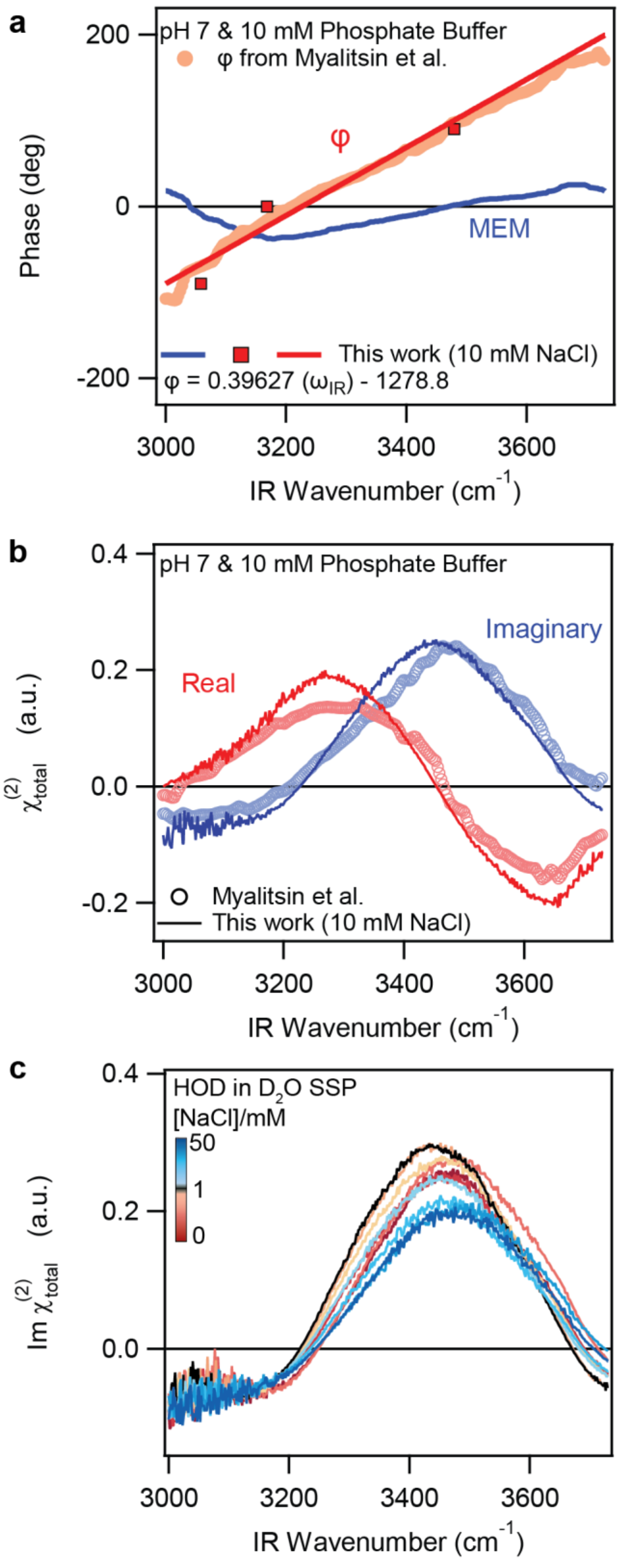

Figure 3.7: (a) The absolute phase determined from the reference complex spectrum of Myalitsin et al.[78] (peach line) and that determined from the MEM phase of our measured intensity spectrum (red squares). The linear fit of the three data points (red squares) was used as the wavenumber-

dependent error phase in our analysis for this set of experimental conditions. (b) The real (red) and imaginary (blue) spectra of 10 mM NaCl HOD at natural pH, which are similar to the HD-SFG measurements of the silica/HOD interface with 10 mM phosphate buffer at pH 7. (c) Imaginary spectra over the ionic strength range of neat HOD to 50 mM NaCl using the calculated frequency-dependent error phase for each salt concentration and MEM analysis of the corresponding intensity spectra.

3.3.3 Stern and Diffuse Layer Spectra

With the complex $\chi^{(2)}_{\text{total}}$ spectra in hand, we can now proceed to the deconvolution of the Stern and diffuse layer spectra. To achieve this goal, we followed the route proposed by Wen et al.,[64] which we have used in our previous work at the silica/H_2O interface.[44,69] The analysis entailed the determination of the $\chi^{(3)}$ term by finding two different ionic strength points where we assumed the Stern layer ($\chi_s^{(2)}$) structure was unchanging and that all differences between the spectra were due to differences in g_3 (for further details about determining the $\chi^{(3)}$ spectrum see Appendix B). The resultant complex $\chi^{(3)}$ obtained from this analysis is presented in Figure 3.8.

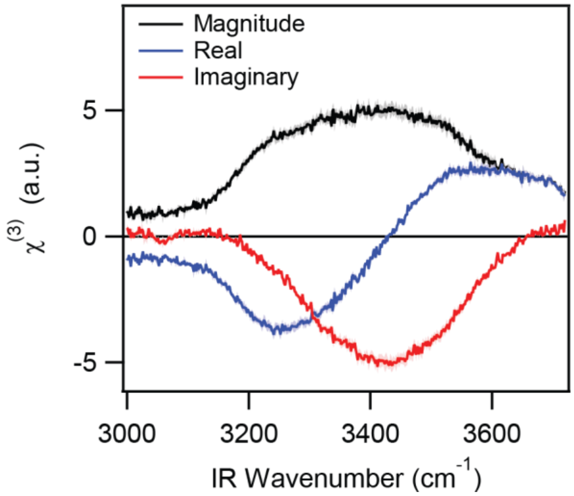

Figure 3.8: The complex $\chi^{(3)}$ spectrum of the silica/HOD interface. The reported complex spectrum is the average from analyzing replicate SFG measurements. Shaded areas represent the error bars propagated from the zeta potential measurements.

To test our $\chi^{(3)}$ spectrum, we determined the resulting $\chi^{(3)}g_3$ (diffuse layer) spectrum at pH 12 with a background of 50 mM NaCl and compared it to that from Urashima et al.[92] Figure 3.9(a) who based it on the overall difference spectra at a high salt concentration (~100 mM and 1

M). Our diffuse layer spectrum is similar to that reported by Urashima et al.[92] as both of the spectra depict a single peak centered at ~3400 cm^{-1}. As further support of our $\chi^{(3)}$ spectrum, we determined the Stern layer imaginary spectrum for the silica/HOD interface at pH 12 and 50 mM NaCl and found a strong resemblance to the analogous $\chi^{(2)}_{\text{topmost}}$ spectrum of Urashima et al.[92] at pH 12 and 2 M NaCl Figure 3.9(b), with slight line shape deviations at extremely high (>3600 cm^{-1}) and low (<3100 cm^{-1}) wavenumbers being a major difference. This suggests that at this high pH, increasing the Na$^+$ concentration from ~60 mM in our experiment (50 mM NaCl + 10 mM NaOH) to 2 M had little impact on the Stern layer structure. We reason that at this pH the high surface charge density leads to a Stern layer nearly saturated with Na$^+$ at 60 mM bulk Na$^+$ concentration such that the structure does not change significantly upon further salt addition.

With confidence in our $\chi^{(3)}$ spectrum of HOD, we determined the pH-dependent diffuse layer spectra of HOD by multiplying the corresponding g_3 values with $\chi^{(3)}$ and made a comparison to the diffuse layer spectra reported for the interface with H_2O Figure 3.9(a).[44,69] Similar to infrared and Raman studies, the vSFG $\chi^{(3)}g_3$ spectra of H_2O is red shifted with respect to that of the isotopically diluted water (HOD), which is attributed to the intermolecular resonant coupling present in H_2O.[92] Additionally, the difference in spectral line shape and the lack of amplitude at lower wavenumber for the HOD compared with H_2O in the diffuse layer spectra suggest that the Fermi resonance contributes significantly to the latter. Nevertheless both $\chi^{(3)}g_3$ spectral responses are dominated by a negative mode in the imaginary spectra, with a small positive feature above 3600 cm^{-1}. Furthermore, the intensity of H_2O versus HOD in the diffuse layer spectra Figure 3.9(a) is consistent with the lesser amount of OH oscillators in the latter (made by diluting 1 part H_2O in 4 parts D_2O). Additionally, we note that there is a strong similarity of the diffuse layer HOD imaginary spectra to the PPP intensity spectra from HOD Figure 3.2(c) suggesting that the PPP spectra of HOD are picking up more contributions from the diffuse layer (the $\chi^{(3)}g_3$ term) than the SSP spectra.

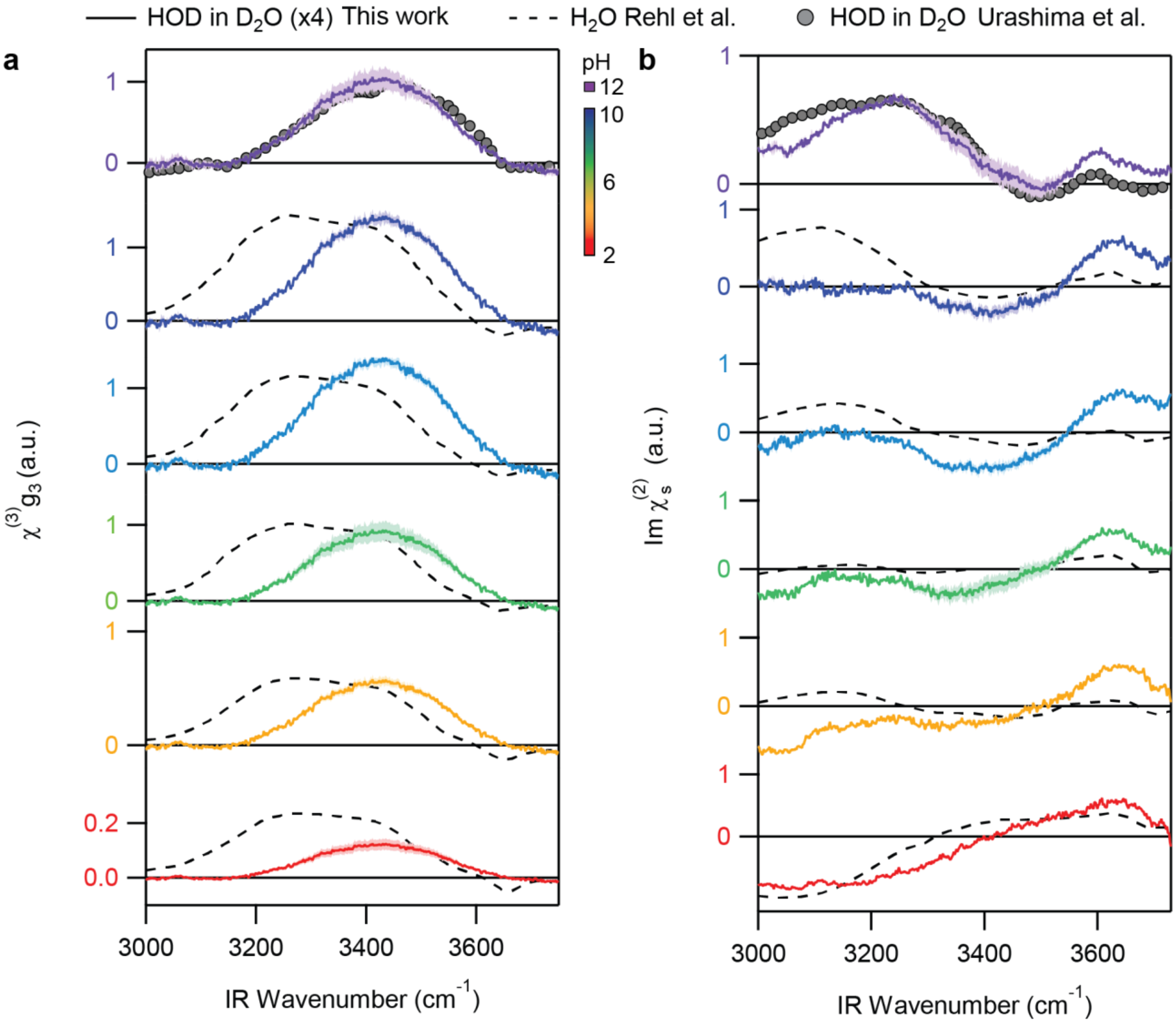

Figure 3.9: (a) Diffuse layer and (b) Stern layer spectra of HOD and H_2O over the pH range of 10 to 2 at 50 mM NaCl. The H_2O spectra were reported in our previous work (Rehl et al.[44]). An additional measurement at pH 12 is also included to allow for comparison with rescaled measurements at pH 12 and 2 M by Urashima et al.[92] Shaded areas represent the uncertainty propagated from the zeta potential measurements.

To determine the Stern layer spectra, the $\boldsymbol{\chi^{(3)}g_3}$ spectra were subtracted from the corresponding $\boldsymbol{\chi^{(2)}_{total}}$ complex spectra. Even though the diffuse layer spectra exhibit a significant difference between HOD in D_2O and H_2O, the overall spectral features in the Stern layer of HOD show a striking resemblance to that from H_2O but with important differences (Figure 3.9(b)). In our previous work, we identified the three spectral regions associated with the different types of hydrogen bonding environments of H_2O in the Stern layer: 3150, 3400, and 3600 cm^{-1}.[44,69] To begin with the latter, we note the mode above 3600 cm^{-1} in both sets of spectra did not change significantly with pH. This mode is independent of pH by multiple groups and has been assigned to either the OH from a silanol site (directed away from the surface) or that from HOD or H_2O weakly donating a hydrogen bond to the oxygen of a siloxane group.[259,260] Based on the positive sign of this mode, it is consistent with an OH group pointed towards the surface.

Prior to discussing the next two spectral regions, it is useful to point out one of the unusual acid-base properties of the silica/aqueous interface. Specifically, interesting observations regarding the acid-base properties of silica suggest that it exhibits bimodal behaviour (i.e., two pKa values stemming from two types of silanol sites). Previous molecular dynamic simulations have proposed that the pKa differences arise from silanol sites that either orient their hydrogens out-of-plane with the OH group pointing towards the bulk solution (pKa = 5.6) or those that orient their hydrogens in-plane, acting as a hydrogen-bond donor to a neighboring site (pKa = 8.5).[89,239] An outstanding goal is to relate the acid-base chemistry of these surface sites with the water spectra.

A small negative feature at 3400 cm^{-1} is apparent in both H_2O and HOD at pH ≥ 4. The microscopic description of this negative mode is unclear as it does not appear in recent spectral simulations with molecular dynamics based on density functional theory (MD-DFT).[261] Furthermore, classical molecular dynamics suggest that the average hyperpolarizability (vSFG activity) of this mode is significantly less in the SSP polarization.[73] Nonetheless, previously the negative mode at 3500 cm^{-1} observed by Urashima et al.[92] at pH 12 was assigned by them to O-H oscillators of water or HOD directed towards the bulk arising from molecules with corresponding O-H or O-D bonds donating an H-bond towards the silica surface. As the pH was lowered from 12 to 10, there is a substantial red shift in this mode. This red shift for the peak maximum has been observed in the spectra simulations of water with MD-DFT[261] upon decreasing the surface charge density on the silica. Between pH 4 to 2, this 3400 cm^{-1} mode flipped from negative to positive for both the HOD and water systems. The positive mode seen most clearly in the H_2O Stern layer spectra at pH 2 is consistent with MD-DFT spectral simulations which suggested it arose from water with OH directed towards the surface acting as a hydrogen-bond donor to neutral in-plane silanol sites.[261] Yet as this spectra region consists of contributions of both hydrogen bond interactions with silanols and with the bulk, disentangling information such as the impact of acid-base chemistry of the in-plane sites on the resulting water structure is a challenge.

On the other hand, the ~3200 cm^{-1} mode can provide valuable information on the acid-base properties of silica. When this mode is positive, it has been assigned to O-H oscillators with hydrogens directed towards the silica surface, presumably at siloxide sites (SiO^-). Most interestingly, as the pH was lowered the point at which a negative feature grew at 3200 cm^{-1}, indicative of a flip of the contributing Stern layer oscillators, varied significantly for both systems. Specifically, H_2O only exhibited a negative feature at 3150 cm^{-1} at pH 2 whereas some negative amplitude at lower wavenumber was evident in the HOD spectra at pH 6 and below. The appearance in HOD of this negative feature from pH 8-2 is in good agreement with the prediction of the pKa of the out-of-plane silanols (pKa = 5.6). As such, we attribute the negative feature to OH acting as a hydrogen bond acceptor (hydrogens pointed away from the surface) from the most acidic out-of-plane silanols, consistent with MD-DFT simulations.[239] As these silanols should be deprotonated by pH 8, the lack of a negative feature is consistent with this assignment. We reason that this feature is less clear in the water spectrum at pH 4 and 6 owing to small contributions from intramolecular coupling, which make it difficult to relate the sign of the imaginary spectrum to the orientation of the oscillator. The presence of intramolecular coupling for water in the Stern layer that is acting as a hydrogen bond acceptor from the surface seems possible as both O-H oscillators are directed away from the surface towards other water molecules potentially allowing for the retention of C_{2v} symmetry.

Regarding the influence of intermolecular coupling on the Stern layer spectra, the strongest evidence is observed at pH 2 with the 3150 cm^{-1} mode. Here we observe similar features but with a significant red-shift between the HOD and H_2O water spectra. At this pH near the point of zero charge, the O-H oscillators that contribute at 3150 cm^{-1} point in the direction of the bulk solution (i.e., hydrogens pointed away from the surface). Not only does this orientation allow H_2O (or HOD) to act as a hydrogen bond acceptor for silanol sites but also as a hydrogen bond donor to H_2O (or D_2O) molecules. Indeed, the presence of strongly ordered water at the point of zero charge has previously been observed at various mineral oxide interfaces.[99,262] Molecular dynamic simulations of protonated (fully hydroxylated) silica in contact with water suggest that there would be an increase in the water – water interactions and a reduction in the water – surface interactions at the point of zero charge.[263] As a result, the increase in the aqueous interactions in both HOD in D_2O and H_2O would lead to the differences between the two systems becoming more apparent.

Specifically, a red-shift and broadening in the peak positions in the vibrational spectra have been related to the presence of intermolecular resonant coupling present in H_2O as a result of hydrogen bonding with H_2O molecules.[228,230] Furthermore, previous molecular dynamics simulations at the air/water interface have shown that the type of hydrogen bonding structure regulates the intermolecular resonant coupling.[264,265] In their simulations, symmetric double-donor hydrogen bonding environments contribute more significantly to intermolecular resonant coupling as compared to asymmetric single-donor hydrogen bonding environments. As such we propose that at pH 2, the hydrogen bonding structure of water in the Stern layer exhibits contributions of intermolecular resonant coupling. As a result, a double donor hydrogen bonding structure is promoted giving rise to the red shift in the Stern layer spectrum of H_2O compared with that of HOD. At higher pH values, these differences notably become less prominent as the oscillators begin to shift to an asymmetric hydrogen bonding environment (hydrogens pointed down) thereby decoupling the O-H oscillators of water.

3.4 Conclusions

In summary, by utilizing vSFG in combination with the maximum entropy method and electrokinetic measurements at the silica/HOD interface and comparing it with our previous work at the silica/H_2O interface,[44] we can elucidate the spectral response of vibrational coupling in different parts of the electric double layer. Over the pH range of 10 to 2, vSFG intensity spectra of H_2O and HOD at the silica interface exhibit different spectral responses due to the absence of the Fermi resonance in the HOD spectra. Decomposing the spectra of the Stern layer reveals strong similarities between HOD in D_2O and H_2O over the pH range studied here. However, evidence of intermolecular resonant coupling is observed at pH 2 based on a red-shift of the H_2O spectra from the HOD spectra, which we attribute at this pH to both O-H oscillators of water pointing toward the bulk solution, forming symmetric hydrogen bonds with neighboring H_2O molecules as well as accepting a hydrogen from surface silanol sites. Moreover, the disappearance of the negative feature at low wavenumber in the HOD assigned to water acting as a hydrogen bond acceptor of the surface with increasing pH is consistent with the deprotonation of the out-of-plane silanol sites between pH 2 and 8. Such correlation between this negative mode in the Stern layer spectra of

HOD and the expected pKa of the more acidic sites was not seen in the corresponding water spectra, which we tentatively attribute to the presence of some intramolecular coupling owing to the symmetry of water-oriented with both hydrogens directed towards the bulk.

Chapter 4

Revealing Silica's Response with Charge Inversion in Second Harmonic Generation at the Silica/Water Interface

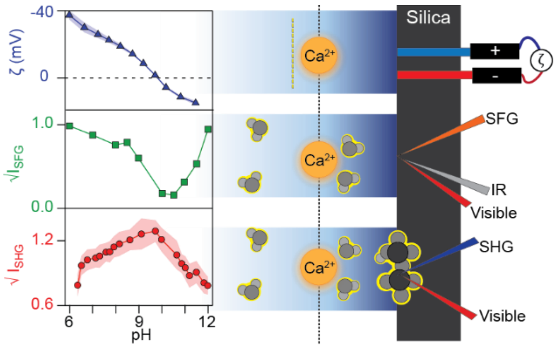

4.1 Introduction

Silica plays an important role in the environment, technology, and biology,[1] and the interactions between silica, ions, and the aqueous phase lead to unique phenomena such as specific ion effects,[40,71,73,86,266] unusual surface acid/base properties,[267,268] and salt-dependent dissolution.[33,269] Developing an intuitive picture and modeling of the processes taking place at charged interfaces, such as that of silica and water, has been the center of several nonlinear optical studies.[27,28,30,51] Among the nonlinear optical techniques used to characterize the interface, second harmonic generation (SHG) has been influential in providing molecular-level information and electrical properties at the silica/water interface.[27,28,30,40,58,65,70,71,86,270,271]

The underlying theory of the sensitivity of nonresonant SHG to charged solid/aqueous interfaces comes from the seminal model proposed by Eisenthal and coworkers[41] which is commonly referred to as the $\chi^{(3)}$ method.[28] This approach emerged from early SHG studies at the silica/water interface and postulated that the signal measured in these experiments was dominated by the orientation or polarization of water molecules responding to the presence of a static electric field originating from the charged silica surface. The success of this model extended its applicability beyond the silica/water interface and to the complementary nonlinear optical technique vibrational sum frequency generation (vSFG).[24,26–28,30,64] The most current, widely accepted model for relating the nonresonant SHG signal to the static electric field is given by

$$\sqrt{I_{SHG}} \propto |\chi^{(2)}_{total}| \propto \ |\chi^{(2)} + \chi^{(3)} \int_0^\infty \mathrm{E}_0(\mathrm{z}) \mathrm{e}^{\mathrm{i}\,\Delta\,\mathrm{kz}} \mathrm{dz}|. \tag{4.1}$$

Here, $\sqrt{I_{SHG}}$ is the square root of the intensity of the second harmonic light, and E_0 is the static field arising from the charged surface, which for silica occurs when the pH of the aqueous phase is above ~2.[43] Finally, $\Delta\, k_z$ is the wave vector mismatch between the incident and second harmonic fields at different penetration depths (z) along the surface normal. The $\chi^{(2)}_{total}$ is the total second-order nonlinear susceptibility of the interface, which can be decomposed into $\chi^{(2)}$and $\chi^{(3)}$ terms.[64,91] The $\chi^{(2)}$ represents the contribution to the second-order nonlinear susceptibility of water molecules aligned by hydrogen bonding interactions close to the surface as well as the underlying mineral surface. The $\chi^{(3)}$ term is the third-order nonlinear susceptibility, accounting for the signal generated due to the alignment or polarization of water molecules by the static electric field.[44,64,91]

In the limit of high ionic strengths and low potentials, the integral of Equation 4.2 can be approximated as the product of the (negative) interfacial potential, $\Phi(0)$, of the electrical double layer and an interference term. [63,66,272]

$$\sqrt{I_{SHG}} \propto |\chi^{(2)}_{total}| \propto |\chi^{(2)} + \chi^{(3)} f_3 \Phi(0)|. \tag{4.2}$$

where $f_3 = \frac{\kappa}{\kappa - i\Delta k_z}$, which accounts for the z-dependent electrostatic screening of the electric based on the Debye length $(1/\kappa)$ and the wave vector mismatch.

The $\chi^{(3)}$ method has been extensively applied to SHG measurements of multiple interfaces, however, the comparison to complementary techniques such as AFM,[75] vSFG,[73] electrokinetic[11,82], and the vibrating plate capacitor method[74] have highlighted discrepancies in relating SHG measurements to the changes in the water response or the interfacial potential. For example, our previous work at the silica/water interface at 500 mM NaCl compared the water responses from the vibrational sum frequency generation (vSFG) in the OH stretching region to second harmonic generation.[73] We observed that vSFG and SHG responses increased in magnitude within the high pH (7 -12) region, but exhibited a different trend in the low pH (7-2) region. This difference at low pH was attributed largely to destructive interference between the SHG response of the water molecules and the SHG response of the silica. Before this work, the silica contribution was often considered to be small and dominated by the water response, which we revealed was not the case and that the underlying silica response is considerable.[73] The change from constructive interference at high pH to destructive interference at low pH was attributed to the reorientation (i.e., flipping) of the water molecules in the aqueous phase, which changed the sign of the aqueous phase SHG response while the sign of the silica SHG response remained unchanged. This reorientation of water molecules at lower pH has since been confirmed by the analysis of the complex spectra determined by vSFG experiments at the silica/water and silica/HOD interfaces.[44,78,273] Moreover, the destructive interference between water and silica at low pH was later confirmed by phase-sensitive SHG measurements that revealed nearly opposite phase behavior between the silica/air signal and the silica/water signal under neat conditions and near the point-of-zero charge.[81]

Yet recently Wang and coworkers[83] proposed that the contributions from both water and silica exhibited pH dependence in SHG measurements. In their model, they explained this pH dependence by incorporating the third-order term in both phases. This extension transformed Equation 4.2 into

$$\chi_{total}^{(2)} = \chi^{(2)} + \chi_{H_2O}^{(3)} f_{3,H_2O} \Phi_{H_2O}(0) - \chi_{SiO_2}^{(3)} f_{3,SiO_2} \Phi_{SiO_2}(0). \quad (4.3)$$

Based on this model, the third order responses of silica and water are *always* destructively interfering with each other, as both $\chi^{(3)}$ values were shown to have the same sign. Moreover, by utilizing Gauss' theorem, they found that the $\chi_{SiO_2}^{(3)}$ term was approximately 50 times larger than that from $\chi_{H_2O}^{(3)}$.

While this proposal further supported the importance of considering the silica contribution to the SHG measurement, it did not address the ability of the silica to either interfere constructively or destructively with the aqueous component (a key finding in our previous work[73]) nor could it explain such transitions from constructive to destructive interference observed at other oxide interfaces with varying pH.[75] Indeed, for a variety of reported mineral and material interfaces, the SHG signal always decreased in magnitude with decreasing pH despite passing through an isoelectric point or point-of-zero charge, which should change the sign of $\Phi(0)$,[75–77] suggesting that destructive interference between the substrate and the aqueous phase tends to dominate at low pH.

In this study, we attempt to shed light on these discrepancies and isolate the pH-dependent contribution of the substrate in second harmonic generation experiments. To achieve these objectives, we compare the SHG response to vibrational sum frequency generation (vSFG) and zeta potential measurements performed on the same planar silica substrates. Such a comparison yields a unique perspective of the electrical double layer.[266] The zeta potential measurements provide electrostatic information about the shear plane of the aqueous region, which is often approximated as the outer Helmholtz plane marking the boundary of the Stern and diffuse layers,[48] whereas the vSFG measurements report on the structure of the water molecules in the electrical double layer without the interference of silica. Finally, when contrasting the second harmonic measurements with the water behaviour and electric potentials from vSFG and zeta potentials, respectively, we reveal the contribution of the silica to SHG.

4.2 Methods

4.2.1 Materials

IR-grade fused silica hemispheres (Almaz optics, KI, 1-inch diameter) were used for the SHG experiments. HPLC grade methanol (Fisher Chemical), sulfuric acid (95-98 %, Caledon Laboratories), and hydrogen peroxide (30 % w/w in H_2O, Sigma-Aldrich) were used. The following were used: NaCl (99.99%, trace metal basis, Alfa Aesar), NaOH (99.99%, trace metal basis, Sigma Aldrich), and $CaCl_2$ (99.999%, trace metal grade, Alfa Aesar). Ultrapure deionized H_2O (18.2 MΩcm) was used during the SHG experiments.

4.2.2 Sample Preparation

Silica hemispheres were rinsed and sonicated for 5 min in deionized H_2O, HPLC grade methanol, and then with deionized H_2O again before being immersed in piranha solution (3:1 H_2SO_4:H_2O_2) for 1 hr. The substrate was rinsed and sonicated in the same manner as before followed by drying in an oven (>100°C) for 15 min. Our in-house Teflon sample cell[274] was rinsed and sonicated in deionized H_2O, MeOH, and deionized H_2O.

Caution: Piranha solution reacts violently with organic material. Ensure there is no residual methanol on the substrate before immersion in piranha.

4.2.3 Second Harmonic Generation Set Up

A beam at 800 nm generated from a Ti: Sapphire oscillator (Spectra-Physics, Maitai, 80 MHz) is passed through a Glan-Thompson polarizer (B. Halle, UV-grade calcite, PGT 4.10), half-wave plate (Thorlabs), and BK7 focusing lens (Thorlabs, focal length = 100 mm) which directs it to the silica sample at an angle of 60° with respect to the surface normal. In this geometry, the SHG light is reflected and passes through a BK7 collimating lens (Thorlabs, focal length = 100 mm), a Glan-Thompson polarizer, a filter (Thorlabs, FB400-40, CWL = 400 nm, FWHM = 40 nm), monochromator (Optometrics, Mini-Chrom MC1-02) and a photomultiplier tube (Hamamatsu Photonics). The response from the photomultiplier tube is amplified and then counted by a gated photon counter (Stanford Research Systems). An in-house LabView code is used to collect the SHG measurements. The optical setup is shown in Figure 4.1 An in-house LabView code is used to collect the SHG measurements.

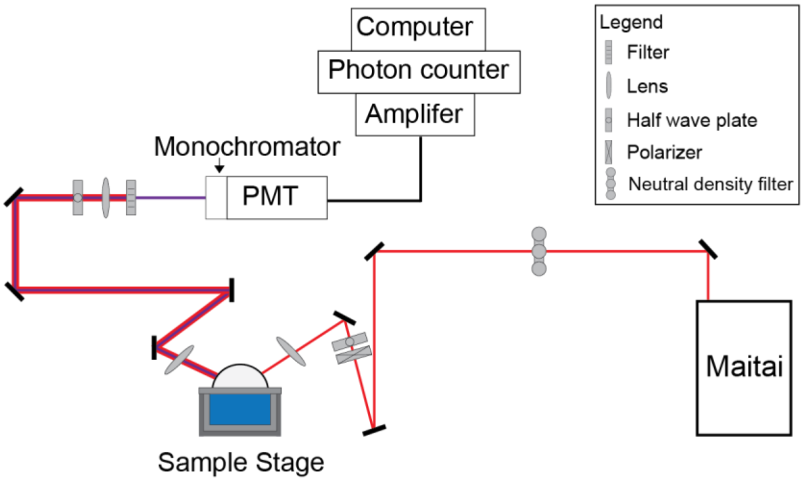

Figure 4.1: Optical setup for the measurement of second harmonic generation at the silica/water interface.

4.2.4 Second Harmonic Generation Experiments

A fused silica hemisphere is assembled to a custom-built Teflon cell and the laser was aligned accordingly. Checks on the quadratic dependence of the SHG signal and center wavelength were done on the silica/air interface before each experiment. Then the following solutions were added and measured: H_2O (30 mins equilibration), 10 mM NaCl (10 mins equilibration), and 100 mM NaCl or 100 mM $CaCl_2$ (10 mins equilibration). The solution was allowed to equilibrate for 10 minutes after the pH was adjusted using NaOH to reach the desired pH. These equilibration times are consistent with those in vSFG and streaming current measurements done in our previous work.[275]

4.2.5 Computational Details

All computations were carried out using the Gaussian 16 suite of programs.[276] The protonated structures in Figure 4.7(a & b) were optimized with CAM-B3LYP[201]/6-31+G(d,p)[202–207] using default convergence parameters. The protonated structure shown in Figure 4.7(c) was extracted from the surface structure of amorphous silica (4.5 sites/nm), with terminal oxygen atoms capped with hydrogen atoms.[277] For all the structures, the first molecular hyperpolarizabilities (β_{ijk}) were computed with CAM-B3LYP/6-31+G(d,p) in the gas phase. The reported values are the vector component of the hyperpolarizabilities parallel to the permanent dipole moment, $\beta_{||}$.[180,219] In the 'T' convention, this value is related to the components of the hyperpolarizability by

$$\beta_{||} = \frac{1}{5}\sum_{i \neq z} \beta_{zii} + \beta_{izi} + \beta_{iiz}. \tag{4.4}$$

The total hyperpolarizability is computed

$$\beta_{tot} = \sqrt{\beta_x^2 + \beta_y^2 + \beta_z^2}\,, \tag{4.5}$$

where

$$\beta_i = \beta_{iii} + \frac{1}{3}\sum_{i \neq j} \beta_{ijj} + \beta_{jij} + \beta_{jji}. \tag{4.6}$$

4.3 Results and Discussion

First, we compare the zeta potential (ζ), integrated vSFG spectra (p-E_{SFG}, p-E_{vis}, p- E_{IR}), and SHG (p-in, p-out) results in the presence of 100 mM NaCl at the silica/aqueous interface with varying pH (Figure 4.2). The zeta potential determined from streaming current measurements reveals that the electric potential increases in magnitude until pH 10 for the aqueous silica interface at 100 mM NaCl, followed by a plateau, and then a decrease at higher pH. Similar observations with a general increase in the zeta potential magnitude with increasing pH can be found in previous measurements at the quartz interface with different monovalent salts and concentrations.[278] This increase in the magnitude of the zeta potential can be attributed to the deprotonation of the surface silanol sites as potentiometric experiments on different forms of colloidal silica indicate that the surface charge densities increase up to pH 10 (the highest pH that they monitored) in the presence of 10-200 mM NaCl or other monovalent salts.[9,47–49]

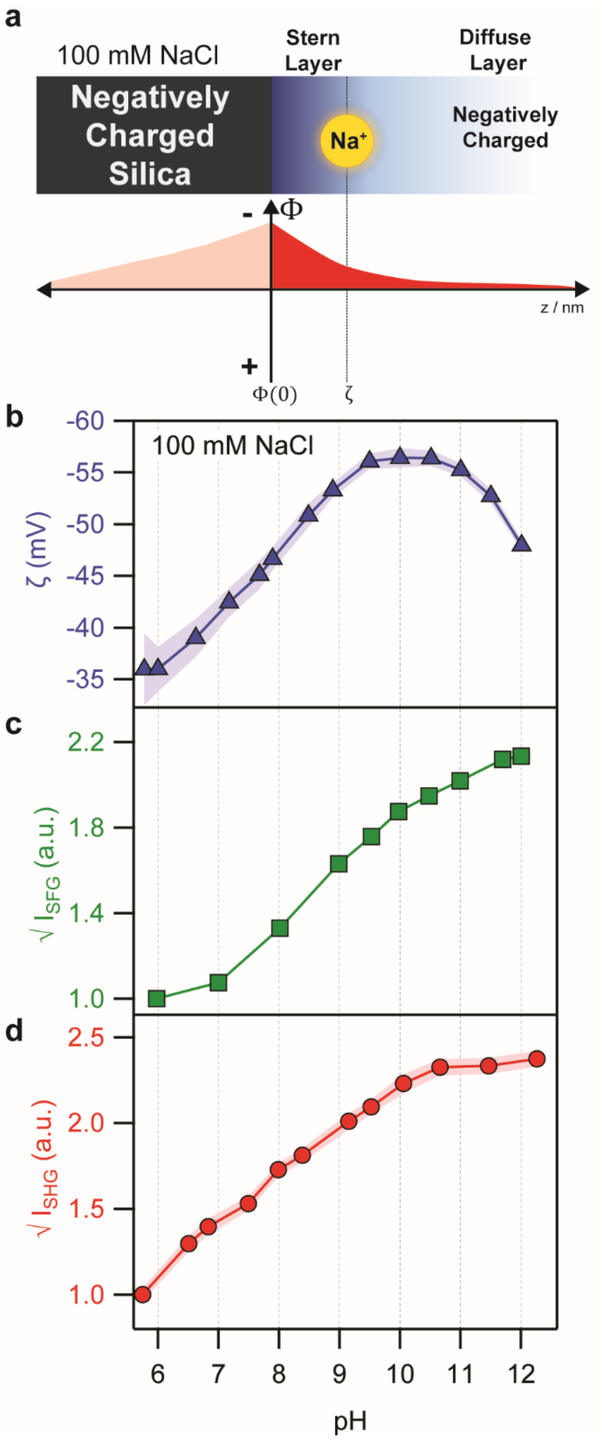

Figure 4.2: (a) Diagram of the electric potential decay in the electrical double layer in the presence of 100 mM NaCl.[45,83] (b) Representative zeta potential performed at the silica interface in the presence of 100 mM NaCl. (c) The square root of the integrated ppp-SFG intensities from 2900 to 3600 cm^{-1} from a representative experiment at the silica interface in the presence of 100 mM NaCl. (d) The square root of SHG intensity of a representative experiment at the silica interface in the presence of 100 mM NaCl. Both vSFG and SHG intensities are normalized to the initial point. Standard deviations are represented by the shaded region in (b) and (d).

Likewise, the square root of the integrated area of the vSFG spectra ($\sqrt{I_{SFG}}$) in the O-H stretching region corresponding to ordered interfacial water displayed an increase in intensity over the entire range. This increase in the observed vSFG signal at the silica/aqueous interface in the presence of 100 mM NaCl is usually attributed to the response of water in the diffuse layer that is modulated by an increasing magnitude of the potential at the boundary of the Stern and diffuse layers owing to surface deprotonation.[44,64] Similarly, SHG measurements exhibit an increase with increasing pH, consistent with previous pH-dependent studies in the presence of various monovalent ions.[40,268,279,280] However, as previously noted, the relative increase in the square root of the SHG signal ($\sqrt{I_{SHG}}$) from pH 6 to 12 is greater than observed for $\sqrt{I_{SFG}}$ (~2.5 vs. 2.2, respectively).[73] This difference suggests the possibility that the silica response is also growing with increasing pH and contributing to the increase in $\sqrt{I_{SHG}}$.

The zeta potential measurements reveal that under these pH conditions (pH 6-12) and ionic strength (100 mM), monovalent counter-ions like sodium are insufficient to neutralize the negative siloxide charges. Consequently, a negative potential modulates the response of the diffuse layer at all pH. Furthermore, the lack of counter-ion compensation in the solid silica matrix should always lead the total potential drop within the bulk silica to be negative at the pH values explored as the surface is net negatively charged (> pH 2). Figure 4.2(a) illustrates this case, where a net negative total potential at the silica surface and throughout the adjacent silica and aqueous regions will occur in the presence of sodium, making it difficult to deconvolute the relative contribution to the SHG as they both are putatively modulated by the same negative potential. One strategy to separate the contribution of the substrate to the overall SHG signal is by promoting conditions in which the interfacial potential modulating the diffuse layer of the aqueous region is of the opposite sign to that at the silica surface. Overcharging creates such a scenario where counter-ions concentrate in the Stern layer and overcompensate the surface charges.[281] In the case of the silica/aqueous interface, the surface sites remain negative (SiO^-) resulting in a net negative total potential in the silica phase, while due to overcharging in the aqueous phase, a net positive potential will be apparent in the diffuse layer (Figure 4.3(a)).

Divalent ions such as Ca^{2+} have been known to reduce the aqueous interfacial potential and cause overcharging in two main cases: (i) as the pH is increased with constant Ca^{2+} concentration[275] or (ii) at neutral pH and sufficiently high Ca^{2+} concentrations (>100 mM).[70,282,283] In our previous work, we utilized vSFG and zeta potential measurements to examine the former, i.e., the mechanism behind overcharging of the silica/water interface in the presence of 100 mM $CaCl_2$ with increasing pH.[275] In Figure 4.3, we compare our previously reported zeta potentials and the square root of the integrated vSFG area to the corresponding SHG measurements of 100 mM $CaCl_2$ over a similar pH range.

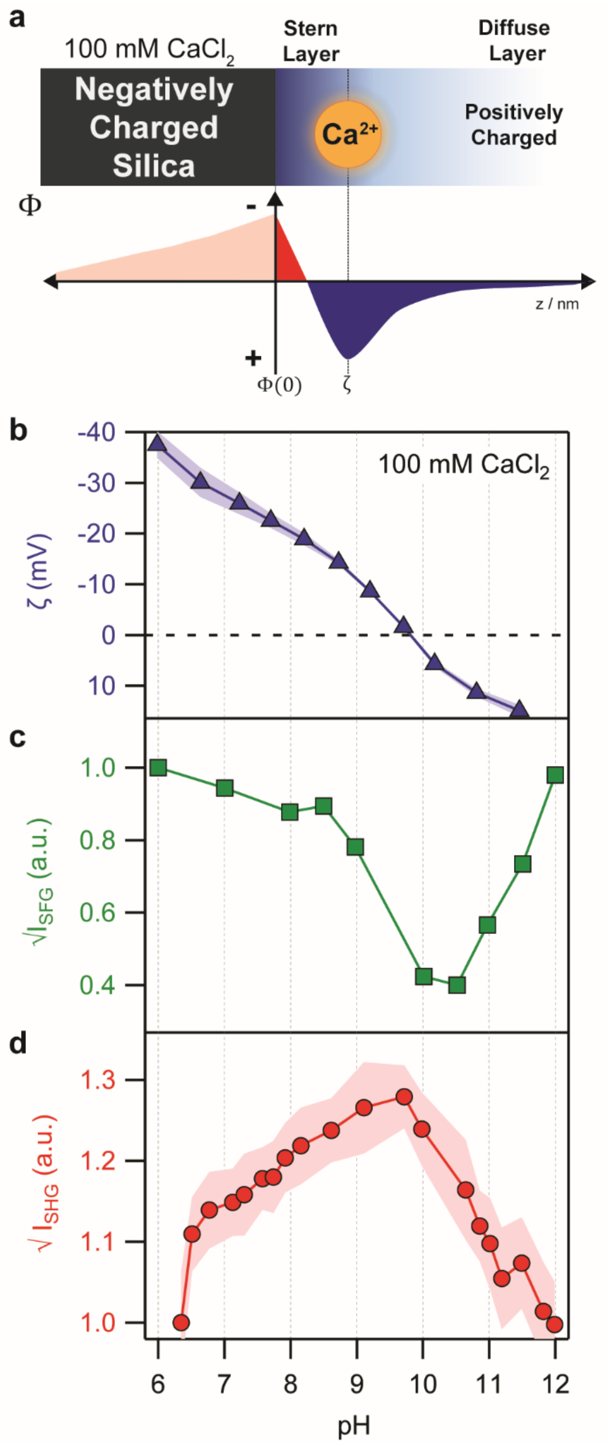

Figure 4.3: (a) Diagram of the electric potential decay in the electrical double layer in the presence of 100 mM $CaCl_2$ under conditions of overcharging (> pH 10).[45,83] (b) Representative zeta potential (ζ) performed at the silica interface in the presence of 100 mM $CaCl_2$ with 10 mM NaCl as background electrolyte. (c) The square root of the integrated ppp-SFG intensities from 2900 to 3600 cm^{-1} from a representative experiment at the silica interface in the presence of 100 mM $CaCl_2$ with 10 mM NaCl. (d) The square root of SHG intensity of a representative experiment at the silica

interface in the presence of 100 mM $CaCl_2$ with 10 mM NaCl. Both vSFG and SHG intensities are normalized to the initial point. Standard deviations are represented by the shaded region in (b) and (d).

Upon examining Figure 4.3, there are significant differences between the three techniques for the Ca^{2+} system unlike that with Na^+ (Figure 4.2). The zeta potential and the $\sqrt{I_{SFG}}$ decrease in magnitude as the pH approaches ~10, after which the zeta potential becomes positive and $\sqrt{I_{SFG}}$ signal begins to increase. These observations are consistent with overcharging and the general sensitivity of the vSFG response of water to the potential at the shear plane.[44,69,273] Furthermore, spectral fitting reveals a change in the orientation of water (i.e., flipping) above pH 10 from water pointed with hydrogens towards the surface at lower pH to hydrogens pointed away from the surface at higher (Figure C1). In contrast, the SHG measurements display the opposite behavior as the intensity increases with pH until ~ pH 10 and then abruptly decreases at higher pH. Interestingly, the pH at which there was a change in the direction of the SHG response occurs qualitatively near the isoelectric point (i.e., when ζ = 0 V) and the pH corresponding to a minimum in vSFG intensity. Previous work at lipid interfaces suggested a constant SHG response of the lipid substrate that interfered destructively or constructively with that from water depending on net water orientation.[74] Yet the presence of a constant silica contribution to the signal cannot explain why the SHG signal *increases* from pH 6 to pH 10 when the vSFG response decreases as shown in Figure C2. An increasing SHG contribution based on the speciation of calcium chloride is possible based on the growth of the $CaOH^+$ as observed in the vSFG spectra.[275] However, as shown by the vSFG spectra and speciation calculations, these species only become prominent at higher pH values (pH>9) and thereafter remained constant (Figure C1). Hence, they cannot have led to the intensity increase observed in the SHG experiments from pH 6 and above.

To rationalize these findings, we present a simplified model of the total response in terms of the total nonlinear susceptibilities of the aqueous $(\chi^{(2)}_{H_2O,total})$ and silica $(\chi^{(2)}_{SiO_2,total})$ phases, i.e.,

$$\sqrt{I_{2\omega}} \propto |\chi^{(2)}_{total}| = |\chi^{(2)}_{SiO_2,total} + \chi^{(2)}_{H_2O,total}|. \qquad (4.7)$$

Similar to the work of Wang and coworkers, the total second order nonlinear susceptibility of both silica and water can be broken down into

$$\chi^{(2)}_{SiO_2,total} = \chi^{(2)}_{SiO_2} + \chi^{(3)}_{SiO_2} f_{3,SiO_2} \Phi(0)\,. \qquad (4.8)$$

$$\chi^{(2)}_{H_2O,total} = \chi^{(2)}_{H_2O} + \chi^{(3)}_{H_2O} f_{3,H_2O} \Phi(0). \qquad (4.9)$$

In the presence of 100 mM NaCl and $CaCl_2$, the term $\chi^{(2)}_{SiO_2,total}$ can be estimated by considering the difference in behavior between vSFG, which only probes $\chi^{(2)}_{H_2O,total}$, and SHG which probes both $\chi^{(2)}_{SiO_2,total}$ and $\chi^{(2)}_{H_2O,total}$.

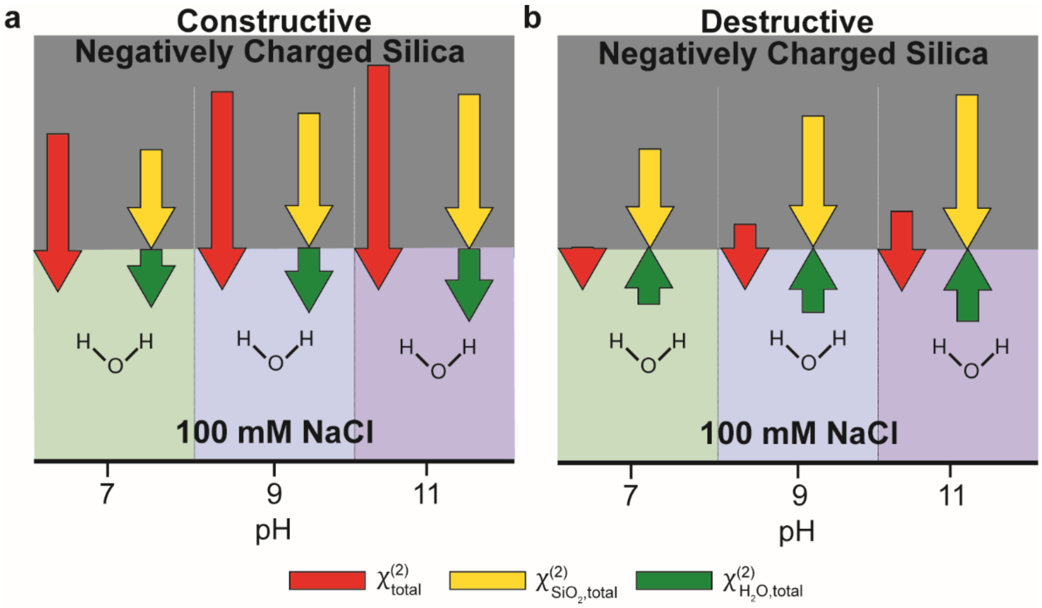

Figure 4.4: Two scenarios illustrating (a) constructive or (b) destructive interference between the total second nonlinear susceptibility contributions in the aqueous phase (green) and silica (yellow) from neutral to high pH in the presence of 100 mM NaCl. The total (red) is the sum of these two

contributions, where the magnitude is proportional to the square root of the SHG intensity. The direction of the arrow is drawn arbitrarily to a relative scale, and they represent instances where there is constructive (same arrow direction) or destructive (opposite arrow direction) interference. A water molecule is drawn to indicate the average orientation based on spectral fitting.[275]

First, in the presence of 100 mM NaCl, the vSFG measurements make evident that $\chi^{(2)}_{H_2O,total}$ is increasing in magnitude from neutral to high (Figure 4.4, green arrows) consistent with the increasing magnitude of the zeta potential. To determine how the contribution of the $\chi^{(2)}_{SiO_2,total}$ will evolve over this pH range, we rely on potentiometric titrations, which have shown that the surface charge density increases from pH 3 to 8.5.[47] Moreover, heterodyne second harmonic generation (HD-SHG) measurements[81] observed that the surface potential became more negative with increasing pH above pH 6. Thus, we can deduce that both $\chi^{(2)}_{H_2O,total}$ and $\chi^{(2)}_{SiO_2,total}$ increase monotonically in magnitude from neutral to pH 12 in the presence of 100 mM NaCl. This is consistent with the SHG intensity increasing with increasing pH (Figure 4.2(c)).

However, if both the silica and water response increase in magnitude without changing sign then from this experiment alone we cannot rule out the possibility that the responses are destructively interfering at all pH values, and the net response is dictated by the larger component. As mentioned, Wang and coworkers[83] proposed that the $\chi^{(3)}$ contribution of silica would be opposite in sign and 20-50 times greater in magnitude to that from the aqueous phase in the presence of 100 mM NaCl. This would result in such a scenario where there would be destructive interference between the $\chi^{(2)}_{SiO_2,total}$ and $\chi^{(2)}_{H_2O,total}$ over the entire pH range studied here. Figure 4.4(b) illustrates the scenario where such destructive interference from pH 6 to 12 with increasing magnitude of both the silica and water response occurs. The sum of the two responses (Figure 4.4(b), red arrows) matches the general trend in SHG if the $\chi^{(2)}_{SiO_2,total}$ response dominates as proposed by Wang and coworkers.[83] However, as we will show such intrinsically destructive interference between the silica and water SHG response cannot explain our observations in the pH-dependent SHG for the aqueous silica/100 mM Ca^{2+} interface.

Accordingly, we now apply this model to the aqueous silica/100 mM Ca^{2+} interface. In the presence of 100 mM $CaCl_2$, from pH 7 to 10, $\chi^{(2)}_{H_2O,total}$ is decreasing in magnitude as reflected by the vSFG measurements (Figure 4.5, green arrows), once again consistent with the decreasing magnitude of the zeta potential. Above pH 10, vSFG spectral fitting indicates that the orientation of water molecules has flipped (reoriented) leading to a change in the sign of the water response. This change in the sign of the water response is also consistent with the change in the sign of the zeta potential from negative to positive above pH 10 (Figure 4.3(a)). Yet in this same pH range, the intensity measured by SHG is increasing from pH 6 to 10 and then decreases, which means the magnitude of $\chi^{(2)}_{total}$ must follow accordingly (Figure 4.5, red arrows). This anti-correlation between the SHG and vSFG can only be rationalized by changes in $\chi^{(2)}_{SiO_2,total}$ as the change in the water response cannot account for the changes in $\chi^{(2)}_{total}$ even with destructive interference between a large constant $\chi^{(2)}_{SiO_2,total}$ and a changing $\chi^{(2)}_{H_2O,total}$ (Figure C2). Moreover, $\chi^{(2)}_{SiO_2,total}$ should not change sign as the pH is varied because the molecular structure of bulk silica, unlike liquid water, cannot flip (reorient).[44,78] As such, the $\chi^{(2)}_{SiO_2,total}$ must be changing uniquely with pH compared to the pH-dependent changes to $\chi^{(2)}_{H_2O,total}$.

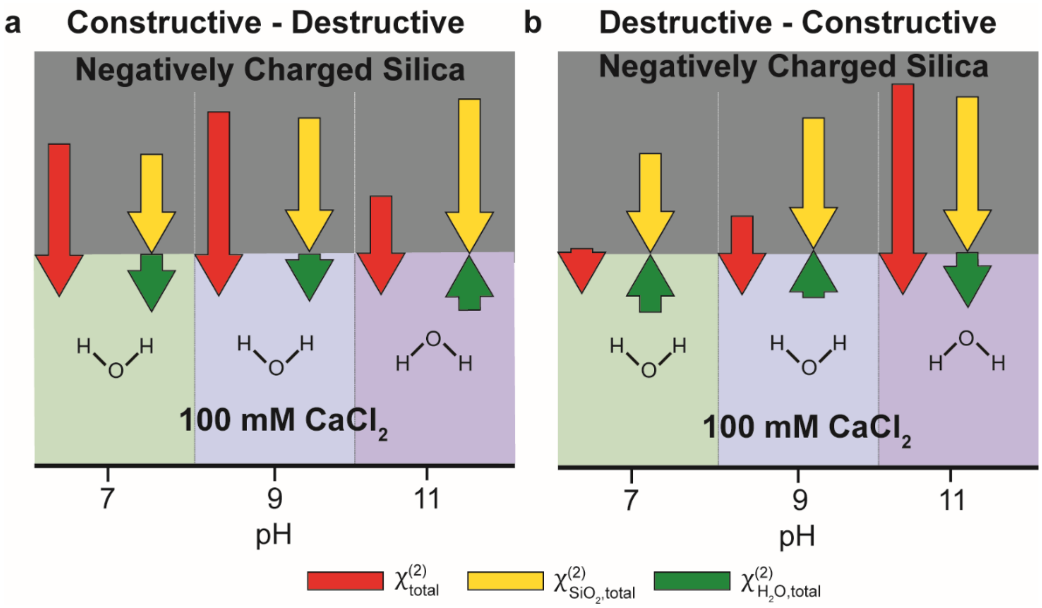

Figure 4.5: Possible scenarios moving from (a) constructive to destructive or (b) destructive to constructive interference of the total second nonlinear susceptibility contributions in the aqueous phase (green), silica (yellow), and the total (red) from neutral to high pH in the presence of 100 mM $CaCl_2$. The measured square root of the SHG intensity is consistent with the scenario in (a).

Under conditions of overcharging, the positive zeta potential impacting the water in the diffuse layer is not the same potential experienced at the silica surface.[282] As shown in Figure 4.3(a) for the case of overcharging, the silica surface would still exhibit a negative potential, which changes sign upon moving away from the surface through the Stern layer. This model of the local potentials is supported by potentiometric titrations that reveal the surface charge density becomes more negative as the pH is increased even in the presence of Ca^{2+} ions.[33,47] Accordingly, we propose that the $\chi^{(2)}_{SiO_2,total}$ response grows with increasing pH owing to the rise in surface charge density at the surface as observed in potentiometric titrations from pH 6 to 8.5.[47] Furthermore, we reason that the interference between $\chi^{(2)}_{SiO_2,total}$ and $\chi^{(2)}_{H_2O,total}$ is constructive until pH 10 when the hydrogens of water have the net direction towards the surface and then becomes destructive at higher pH owing to the flip in the water response as shown in Figure 4.5(a). This scenario is consistent with the observed increase in SHG to pH 10 and a decrease in the SHG signal with further increases to the pH.

If we utilize the model proposed by Wang and coworkers,[83] the silica and water response would be destructive at lower pH when they both experience a negative surface and diffuse layer (zeta) potential, switching to constructive at higher pH once the zeta potential but not the surface potential had changed sign (Figure 4.5(b)). However, this would result in a decrease in SHG from pH 6 to 10 and an increase in the SHG intensity above pH 10, which was not observed (Figure 4.5(b), red arrows). Our model reveals that destructive interference between $\chi^{(2)}_{H_2O,total}$ and $\chi^{(2)}_{SiO_2,total}$ is taking place above pH 10 once the water is flipped (oxygen pointing towards the surface), lending support to our earlier work that reasoned the silica and water responses add constructively in SHG when the water is oriented with hydrogens towards the surface. This interpretation indicates that in the case of 100 mM NaCl, $\chi^{(2)}_{H_2O,total}$ and $\chi^{(2)}_{SiO_2,total}$ are of similar phases, i.e., constructively interfering from neutral to pH 12 (Figure 4.5(a)), ruling out the model proposed by Wang and coworkers[83] under these conditions.

Our simple model rationalizing the pH-dependent SHG results does not resolve the source of the changing response of the silica with varying pH (i.e., $\chi^{(2)}_{SiO_2}$ or $\chi^{(3)}_{SiO_2}\Phi(0)$). However, given the robust derivation of the $\chi^{(3)}$ effect of silica as proposed by Wang and coworkers[83] which requires an opposite phase of $\chi^{(3)}$ of silica and water response, we can rule out a $\chi^{(3)}$ origin as it not consistent with the 100 mM Ca^{2+} SHG measurements. The other possible scenario that we can investigate is the contribution of surface silica sites enveloped in the $\chi^{(2)}_{SiO_2}$ term in Equation 4.8.

The $\chi^{(2)}_{SiO_2}$ term depends on the orientationally averaged hyperpolarizability of the silica surface sites as well as their number density. Recent models of the $\chi^{(2)}_{SiO_2}$ term only considered the abundant species (-SiOH and water) contributions and neglected the hyperpolarizability response of deprotonated species such as SiO^-.[284] This makes it unclear how the deprotonation of -SiOH sites would contribute to the measurement. To evaluate the possibility that the deprotonation of silica can directly contribute to the SHG measurements based on changes to the hyperpolarizability, we compute the nonresonant molecular hyperpolarizabilities of protonated (neutral) and deprotonated (anionic) silica structures with electronic structure computations. Any changes in the molecular hyperpolarizabilities would manifest themselves in $\chi^{(2)}_{SiO_2}$ since

$$\chi^{(2)}_{SiO_2} \propto N(SiO^-)\langle\beta_{SiO^-}\rangle + N(SiOH)\langle\beta_{SiOH}\rangle. \tag{4.10}$$

Here, N is the number density of silanols (SiOH) or siloxides (SiO^-), and $\langle\beta\rangle$ is the orientational average of the first molecular hyperpolarizability.[41,114,248] We computed the molecular hyperpolarizabilities of three silica cluster models, where the Z axis (Figure 4.6, black arrow) is aligned to the Si-O bond which is either protonated or deprotonated.

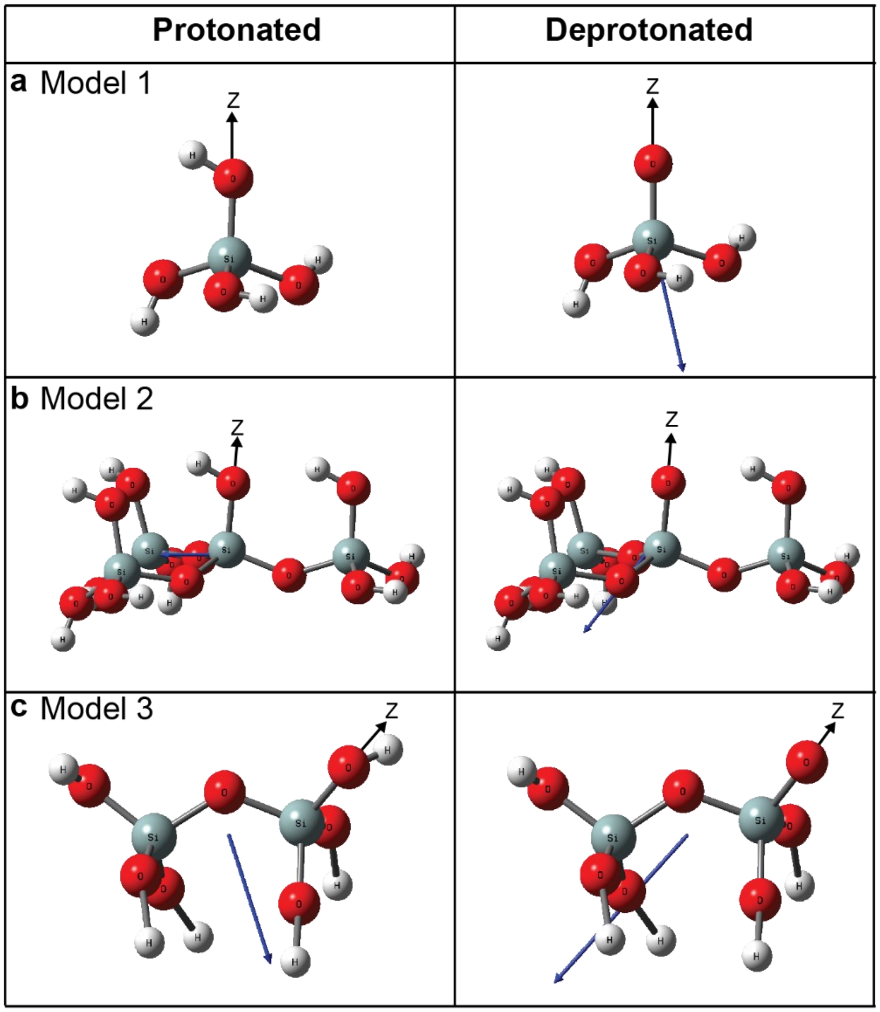

Figure 4.6: Protonated (neutral) and deprotonated (anionic) silica models, (a) orthosilicic acid structure (Model 1), (b) model based on Hassanali and Singer (Model 2),[285] and (c) truncated structure from the surface model proposed by Ugliengo et al.(Model 3).[277] The blue arrow from the center of mass indicates the direction of the dipole moment, while the black arrow indicates the z-axis.

Three models of silica were considered as presented in Figure 4.6: firstly in Model 1, an orthosilicic acid model was constructed ($Si(OH)_4$). In Model 2, we considered a silica model similar to those used in previous work,[285,286] where three of the hydrogens in orthosilicic acid are replaced with -$Si(OH)_3$ groups. Finally, in Model 3, we used a truncated model based on amorphous silica slabs optimized by Ugliengo et al.[277] and commonly employed in ab initio molecular dynamic studies (Figure 4.6(c)).[237,259] Specifically, we selected the first layer of silica representing the surface sites. For all these structures, the hyperpolarizability values associated with the zzz component of the tensor (β_{zzz}), which we assume would be the dominant contributor to the PPP polarization configuration in the SHG experiment was considered. The total hyperpolarizability (β_{tot})and the hyperpolarizability parallel to the dipole moment ($\beta_{||}$) are presented in the Appendix C.

All the silica models exhibit an increase in the magnitude of the hyperpolarizabilities when an -SiOH group is deprotonated. However, as shown in Table S1, Models 2 and 3 provide more consistent results due to the absence of symmetry effects present in Model 1. To determine how these hyperpolarizability changes would influence the $\chi_{SiO_2}^{(2)}$ term, we utilize Equation 4.10 in conjunction with previous potentiometric studies in the presence of NaCl and $CaCl_2$ which would predict the approximate number density of -SiOH and -SiO$^-$ sites. We also assume a total silanol density of 4.6-4.9 OH/nm^2 as commonly employed in the literature.[48,287]

In presence of 100 mM NaCl, previous potentiometric titrations on silica colloids have shown that there is an increase in the number of deprotonated sites (SiO$^-$) from 2% at pH 5.8 to 25% at pH 10.[48] Similarly, potentiometric titrations in the presence of 67 mM $CaCl_2$ show that there is also an increase in the number of SiO$^-$ sites from 2% at pH 6.2 to 25% at pH 8.5.[47] Utilizing these values with the computed hyperpolarizabilities in Equation 4.10 provides an estimate of a ~2 fold increase in the $\chi_{SiO_2}^{(2)}$ term in both salts with increasing pH from 6 to ~9. As the SHG measures both the silica and water response, we cannot quantify the contribution of each. Yet, the computational model does qualitatively show that there should be an increase in the SHG response due to the deprotonation of silanols. Furthermore, the computational model points to a $\chi_{SiO_2}^{(2)}$

contribution as opposed to a $\chi^{(3)}_{SiO_2}\Phi(0)$ contribution (an indirect response owing to the polarization of the silica by the static surface field).

We note, however, that another model for $\chi^{(3)}$ has been recently put forth by Geiger and coworkers.[81] They recently performed HD-SHG experiments at the silica interface in the presence of 500 mM NaCl that revealed a new $\chi^{(3)}$ term (labelled $\chi^{(3)}_{x}$) which is 1.5 times greater than the aqueous counterpart and 90° phase shifted relative to $\chi^{(3)}_{H2O}$, which they tentatively assigned to quadrupolar contributions to the third-order nonlinear susceptibility. Moreover, they concluded that this term does not originate from silica. We would expect that this third-order term is inherently dependent on the potential of the aqueous phase, which would lead to the SHG response resembling that of vSFG in the presence of 100 mM $CaCl_2$. However, as we have shown the SHG response displays the opposite behaviour to that of vSFG in these conditions. This suggests that a term other than $\chi^{(3)}_{x}$ is contributing to the measurements although we cannot rule it out if this term is modulated by the surface potential, which is negative, rather than the potential at the outer Helmholtz (or shear) plane, which is positive, under conditions of overcharging.

4.4 Conclusions

In summary, by comparing the pH-dependent SHG, vSFG, and zeta potential trends of the silica/water interface with 100 mM NaCl or 100 mM $CaCl_2$, we reveal that the silica substrate response is changing with pH and contributes significantly to the observed SHG signal. Monovalent ions such as Na^+ lead to the total potential being negative in the aqueous phase, which leads to constructive interference between the silica and the aqueous phase from pH 6 and above, consistent with an overall increase in the SHG signal due to an increase in the magnitude of both the silica and water response. In the presence of Ca^{2+}, the potential in the aqueous phase can become positive due to overcharging with increasing pH. In such a scenario, the signal from the water and silica interferes destructively owing to the reorientation of water, which results in the SHG signal decreasing substantially above the pH of overcharging (pH 10). However, such a model requires a significant change in the silica response with pH. We propose that one source of the pH-dependent SHG response might be the change in the hyperpolarizability of silica upon deprotonation. This possible origin of the response is exciting as it suggests SHG can be used to directly probe deprotonation of mineral oxide surfaces, providing complementary information to techniques such as SFG that monitor the water response and zeta potential measurements that report on the potential at the shear plane. These observations highlight the sensitivity of SHG to the substrate (silica) and reveal how combining second order nonlinear optical and electrokinetic measurements are crucial to shed light on phenomena such as overcharging and specific ions effects at mineral aqueous interfaces.

Chapter 5

Conclusions

5.1 Summary of Thesis

The overarching goal of this thesis was to highlight new physical insights in experimental and computational nonlinear optical studies. Second order nonlinear optical techniques such as vibrational sum frequency generation (vSFG) and second harmonic generation (SHG) provide unique information on microscopic and macroscopic levels due to their unique centrosymmetric restrictions. Due to the high sensitivity and selectivity, the promise of utilizing these techniques in studying interfaces relevant to processes such as oil-sand mining operations can yield fruitful results in tackling the challenges present in this area. For example, using vSFG to study interactions between kaolinite, silica, and water in the presence of calcium suggests conditions that lead to the dewatering of oil-sand tailings that can be predicted with vSFG.[288] As a result, vSFG can screen dewatering conditions such as ions, pH, and other additives. However, while the field of nonlinear optics continues to grow, the gaps in the interpretations and models persist due to underlying physical phenomena such as electronic resonances and vibrational coupling. Considering the factors that affect the experimental and computational determinations can provide more accurate physical insights on both a microscopic and macroscopic level.

In Chapter 2, the aim was to determine the effect of excitation wavelength in hyperpolarizability computations. The relationship between the hyperpolarizability of a system and the intramolecular charge transfer taking place within a system is well known. However, this relationship has been determined in off-resonant regimes. As such, it is unclear how the charge transfer effects would behave in on-resonant regions such as near one and two-photon resonances. Furthermore, optimal gap tuning of range-separated hybrid functionals has provided variable accuracy relative to the experiment. One cause of this variability is optimal gap tuning being rendered ineffective due to the underlying charge transfer properties of the molecular system (commonly referred to as pathological behaviour). Hence, by utilizing the nitroanilines' hyperpolarizability trend based on charge transfer (pNA>oNA>mNA), we can uncover how the excitation wavelength affects the prediction of the hyperpolarizabilities in both on and off resonant regimes and optimal gap tuning of RSH functionals. In non-resonant regions, with reference to CCSD/aug-cc-pVDZ and experimental studies, we find that some computational approaches do not consistently reproduce the nitroanilines' trend at specific excitation wavelengths. For example, RSH functionals require optimal gap tuning to reproduce the trend. In resonant regions, we find that damped response theory predicts that the trend is maintained at the two-photon absorption but breaks down near the one-photon pole. This behavior suggests that the underlying charge transfer characteristics are compromised in the one-photon pole region. With reference to the two-state model suggests that this is due to the presence of other electronic states and false poles in some of the isomers. Furthermore, we find cases where optimal gap tuning is ineffective (pathological behavior) depends on the excitation wavelength.

In Chapter 3, the goal was to isolate the vibrational coupling effects in the Stern and diffuse layer vSFG spectra at the silica/water interface. While vSFG spectroscopy is a powerful tool for determining the local hydrogen-bonding environment at the silica/water, intramolecular vibrational coupling in H_2O can make it challenging to relate vibrational spectra to a molecular description of the system. While numerous bulk studies have shed light on this phenomenon, the influence of intra- and intermolecular vibrational coupling on the resulting electrical double layer spectra at buried interfaces remains largely unexplored. By utilizing the combination of vibrational sum frequency generation (vSFG), electrokinetic measurements, and the maximum entropy method on isotopically diluted water (HOD) at the silica/aqueous interface, we reveal the influence of vibrational coupling on the Stern and diffuse layer spectra as the surface charge density is varied.

For the pH-dependent Stern layer spectra, we observe differences in the frequency centers at pH 2 that are less significant at higher pH, signifying the presence of intermolecular coupling, which can be related to the double donor hydrogen-bonded structure of water. Furthermore, the differences in the evolution of the Stern layer of H_2O and HOD suggest that the presence of intramolecular coupling in the former may distort the spectral response. Moreover, we observe that the evolution of the HOD closely matches the pKa of the out-of-plane silanols predicted by previous molecular dynamics simulations.

In Chapter 4, the goal was to isolate the contribution of the silica in second harmonic generation (SHG) studies at the silica/water interface and determine the origin of this contribution. The contribution of the substrate in SHG measurements remains a controversial question since isolating the contribution of the substrate in second harmonic generation (SHG) studies remains a challenge. In this study, the silica (substrate) contribution at the silica/water interface was deconvoluted by combining SHG with previously measured zeta potential and vibrational sum frequency generation (vSFG) measurements under conditions that promote charge inversion. Zeta potential and the vSFG measurements follow the same trend, whereas SHG yields the opposite behaviour under the same conditions. By using density functional theory computations, we find that changes in the hyperpolarizability upon the deprotonation of surface sites result in silica contributing to the SHG measurements. This results in the contribution of silica in SHG measurements being able to interfere with the aqueous phase constructively or destructively.

5.2 Future Work

The broad nature of this thesis leaves considerable room for further investigations. Several challenges and questions are related to the work done here, which can provide new physical insights through experiments and computations.

As shown in Chapter 4, the application of (homodyne) SHG to obtain structural and electrostatic information at mineral oxide interfaces is hindered by the interference between the mineral and aqueous phases. While utilizing phase-sensitive or heterodyne second harmonic generation setups can resolve the complex values, they cannot separate the contributions of the individual terms. As a result, the challenge that needs to be addressed is: can we deconvolute the silica response in conventional homodyne SHG? To tackle this challenge, the likely option would be to combine vSFG with SHG with an appropriate reference system to account for the measured quantities. Indeed, such an approach can open the door to the quantification of the electrostatics of the substrate, under a buried interface. This determination would be of great value in both environmental and technological studies on minerals and materials as properties such as the surface charge density can only be determined on substrates with large surface areas (particles), whereas the surface area of the substrate does not restrict the nonlinear optical techniques.

The studies on charge inversion done with calcium can also be extended by attempting measurement with other divalent cations (Mg^{2+}, Ba^{2+}, and Sr^{2+}). Previous work based on HD-SHG, surface charge density, and zeta potential measurements shows remarkable differences based on the specific cation. However, it is unclear where these differences originate from as the cations are known to have several different properties such as the difference in speciation, ion affinity, and hydration shells. As shown in Chapter 3, utilizing vSFG with the maximum entropy method and zeta potential measurements can yield valuable insights into the structure of Stern and diffuse layers. Furthermore, comparison to previous HD-SHG measurements can permit the determination of the ion’s contribution in SHG studies.

Computational modeling of the nonlinear responses of interfaces can provide a comprehensive microscopic picture. However, simulations are centered around vibrational sum frequency generation, with the minimal ground being covered for the properties determined through SHG. The challenge mainly stems from the high computational cost associated with the determination of hyperpolarizabilities over an extended system such as a mineral oxide interface. More recently, schemes based on quantum mechanical–molecular mechanics (QM-MM) at the air/water interface were used to determine second harmonic generation hyperpolarizabilities.[289] The approach enabled the determination of hyperpolarizability parameters (β_{zzz} & $\beta_{||}$) at each water layer of the interface. While this approach is still in its infancy, adopting it at the silica/water can provide valuable physical insights into the contribution of silica, ions, and water molecules in SHG studies.

Such computational modeling can be beneficial in rationalizing the different ionic strength-dependent findings in studying the HOD-D_2O/silica interface (Appendix B, Figure B3). HOD-D_2O and H_2O display very different responses, likely pointing to fundamental differences between the two species. While previous work on D_2O has suggested that nuclear quantum effects may play a role, the extent to which they manifest themselves is unclear. Combining computational-based modeling with experimental measurements can reveal the unique properties of water that modulate the macroscopic properties.

While computational modeling can provide insights on a microscopic level, the accuracy of these findings (energies, structures, properties, etc) relative to experiments will always depend on the level of theory. In Chapter 1, we use optimal gap tuning to improve the accuracy of the computed hyperpolarizability. However, as noted earlier, optimal gap tuning is inherently flawed in the presence of a solvent, which points to shortfalls in early optimal gap tuning studies of hyperpolarizabilities. Indeed, in more recent work, Kronik and coworkers have devised a new approach to consider solvation in optimal gap tuning.[290] Revisiting the prediction of the hyperpolarizabilities with this new approach can serve as a helpful test in predicting the ability of optimal gap tuning in solvated systems.

References

(1) Iler, R. K. *The Chemistry of Silica: Solubility, Polymerization, Colloid and Surface Properties, and Biochemistry*; Wiley: New York, 1979.

(2) Bergna, H. E. The Colloid Chemistry of Silica.

(3) Shimura, F. *Semiconductor Silicon Crystal Technology*; Elsevier, 2012.

(4) Belton, D. J.; Deschaume, O.; Perry, C. C. An Overview of the Fundamentals of the Chemistry of Silica with Relevance to Biosilicification and Technological Advances. *FEBS J.* **2012**, *279* (10), 1710–1720. https://doi.org/10.1111/j.1742-4658.2012.08531.x.

(5) Heaney, P. J.; Prewitt, C. T.; Gibbs, G. V. *Silica: Physical Behavior, Geochemistry, and Materials Applications*; Walter de Gruyter GmbH & Co KG, 2018.

(6) Chalaturnyk, R. J.; Don Scott, J.; Özüm, B. Management of Oil Sands Tailings. *Pet. Sci. Technol.* **2002**, *20* (9–10), 1025–1046. https://doi.org/10.1081/LFT-120003695.

(7) Speight, J. G. Chapter 3 - Oil Sand Mining. In *Oil Sand Production Processes*; Speight, J. G., Ed.; Gulf Professional Publishing: Boston, 2013; pp 59–79. https://doi.org/10.1016/B978-0-12-404572-9.00003-6.

(8) Morag, J.; Dishon, M.; Sivan, U. The Governing Role of Surface Hydration in Ion Specific Adsorption to Silica: An AFM-Based Account of the Hofmeister Universality and Its Reversal. *Langmuir* **2013**, *29* (21), 6317–6322. https://doi.org/10.1021/la400507n.

(9) Brown, M. A.; Abbas, Z.; Kleibert, A.; Green, R. G.; Goel, A.; May, S.; Squires, T. M. Determination of Surface Potential and Electrical Double-Layer Structure at the Aqueous Electrolyte-Nanoparticle Interface. *Phys. Rev. X* **2016**, *6* (1), 011007. https://doi.org/10.1103/PhysRevX.6.011007.

(10) Schlegel, M. L.; Nagy, K. L.; Fenter, P.; Sturchio, N. C. Structures of Quartz (100)- and (101)-Water Interfaces Determined by x-Ray Reflectivity and Atomic Force Microscopy of Natural Growth Surfaces. *Geochim. Cosmochim. Acta* **2002**, *66* (17), 3037–3054. https://doi.org/10.1016/S0016-7037(02)00912-2.

(11) Lützenkirchen, J.; Scharnweber, T.; Ho, T.; Striolo, A.; Sulpizi, M.; Abdelmonem, A. A Set-up for Simultaneous Measurement of Second Harmonic Generation and Streaming Potential and Some Test Applications. *J. Colloid Interface Sci.* **2018**, *529*, 294–305. https://doi.org/10.1016/j.jcis.2018.06.017.

(12) Boyd, R. W. *Nonlinear Optics*; Academic press, 2020.

(13) Butcher, P. N.; Cotter, D. *The Elements of Nonlinear Optics*; Cambridge Studies in Modern Optics; Cambridge University Press: Cambridge, 1990. https://doi.org/10.1017/CBO9781139167994.

(14) Göppert-Mayer, M. Über Elementarakte Mit Zwei Quantensprüngen. *Ann. Phys.* **1931**, *401* (3), 273–294. https://doi.org/10.1002/andp.19314010303.

(15) Maiman, T. H. Stimulated Optical Radiation in Ruby. *Nature* **1960**, *187* (4736), 493–494. https://doi.org/10.1038/187493a0.

(16) Franken, P. A.; Hill, A. E.; Peters, C. W.; Weinreich, G. Generation of Optical Harmonics. *Phys. Rev. Lett.* **1961**, *7* (4), 118–119. https://doi.org/10.1103/PhysRevLett.7.118.

(17) Rumi, M.; Perry, J. W. Two-Photon Absorption: An Overview of Measurements and Principles. *Adv. Opt. Photonics* **2010**, *2* (4), 451–518. https://doi.org/10.1364/AOP.2.000451.

(18) Squier, J. A.; Müller, M.; Brakenhoff, G. J.; Wilson, K. R. Third Harmonic Generation Microscopy. *Opt. Express* **1998**, *3* (9), 315–324. https://doi.org/10.1364/OE.3.000315.

(19) Shen, Y. R. Surface Properties Probed by Second-Harmonic and Sum-Frequency Generation. *Nature* **1989**, *337* (6207), 519–525. https://doi.org/10.1038/337519a0.

(20) Kanis, D. R.; Ratner, M. A.; Marks, T. J. Design and Construction of Molecular Assemblies with Large Second-Order Optical Nonlinearities. Quantum Chemical Aspects. *Chem. Rev.* **1994**, *94* (1), 195–242. https://doi.org/10.1021/cr00025a007.

(21) Kleinman, D. A. Nonlinear Dielectric Polarization in Optical Media. *Phys. Rev.* **1962**, *126* (6), 1977–1979. https://doi.org/10.1103/PhysRev.126.1977.

(22) Hall, S. A.; Jena, K. C.; Covert, P. A.; Roy, S.; Trudeau, T. G.; Hore, D. K. Molecular-Level Surface Structure from Nonlinear Vibrational Spectroscopy Combined with Simulations. *J. Phys. Chem. B* **2014**, *118* (21), 5617–5636. https://doi.org/10.1021/jp412742u.

(23) Terhune, R. W.; Maker, P. D.; Savage, C. M. Optical Harmonic Generation in Calcite. *Phys. Rev. Lett.* **1962**, *8* (10), 404–406. https://doi.org/10.1103/PhysRevLett.8.404.

(24) Eisenthal, K. B. Liquid Interfaces Probed by Second-Harmonic and Sum-Frequency Spectroscopy. *Chem. Rev.* **1996**, *96* (4), 1343–1360. https://doi.org/10.1021/cr9502211.

(25) Eisenthal, K. B. Equilibrium and Dynamic Processes at Interfaces by Second Harmonic and Sum Frequency Generation. *Annu. Rev. Phys. Chem.* **1992**, *43* (1), 627–661. https://doi.org/10.1146/annurev.pc.43.100192.003211.

(26) Eisenthal, K. B. Second Harmonic Spectroscopy of Aqueous Nano- and Microparticle Interfaces. *Chem. Rev.* **2006**, *106* (4), 1462–1477. https://doi.org/10.1021/cr0403685.

(27) Covert, P. A.; Hore, D. K. Geochemical Insight from Nonlinear Optical Studies of Mineral–Water Interfaces. *Annu. Rev. Phys. Chem.* **2016**, *67* (1), 233–257. https://doi.org/10.1146/annurev-physchem-040215-112300.

(28) Geiger, F. M. Second Harmonic Generation, Sum Frequency Generation, and $\chi(3)$: Dissecting Environmental Interfaces with a Nonlinear Optical Swiss Army Knife. *Annu. Rev. Phys. Chem.* **2009**, *60* (1), 61–83. https://doi.org/10.1146/annurev.physchem.59.032607.093651.

(29) Geiger, F. M.; Hartland, G. V. Sixty Years of Surface-Specific Spectroscopy. *J. Phys. Chem. C* **2022**, *126* (34), 14375–14379. https://doi.org/10.1021/acs.jpcc.2c05021.

(30) Backus, E. H. G.; Schaefer, J.; Bonn, M. Probing the Mineral–Water Interface with Nonlinear Optical Spectroscopy. *Angew. Chem. Int. Ed.* **2021**, *60* (19), 10482–10501. https://doi.org/10.1002/anie.202003085.

(31) Dewan, S.; Yeganeh, M. S.; Borguet, E. Experimental Correlation Between Interfacial Water Structure and Mineral Reactivity. *J. Phys. Chem. Lett.* **2013**, *4* (11), 1977–1982. https://doi.org/10.1021/jz4007417.

(32) Putnis, A. Why Mineral Interfaces Matter. *Science* **2014**, *343* (6178), 1441–1442. https://doi.org/10.1126/science.1250884.

(33) Karlsson, M.; Craven, C.; Dove, P. M.; Casey, W. H. Surface Charge Concentrations on Silica in Different 1.0 M Metal-Chloride Background Electrolytes and Implications for Dissolution Rates. *Aquat. Geochem.* *7*, 13–32.

(34) Ghosh, N.; Roy, S.; Mondal, J. A. On the Behavior of Perfluorinated Persistent Organic Pollutants (POPs) at Environmentally Relevant Aqueous Interfaces: An Interplay of Hydrophobicity and Hydrogen Bonding. *Langmuir* **2020**, *36* (14), 3720–3729. https://doi.org/10.1021/acs.langmuir.0c00189.

(35) Weeraman, C.; Yatawara, A. K.; Bordenyuk, A. N.; Benderskii, A. V. Effect of Nanoscale Geometry on Molecular Conformation: Vibrational Sum-Frequency Generation of Alkanethiols on Gold Nanoparticles. *J. Am. Chem. Soc.* **2006**, *128* (44), 14244–14245. https://doi.org/10.1021/ja065756y.

(36) Roeters, S. J.; van Dijk, C. N.; Torres-Knoop, A.; Backus, E. H. G.; Campen, R. K.; Bonn, M.; Woutersen, S. Determining In Situ Protein Conformation and Orientation from the Amide-I Sum-Frequency Generation Spectrum: Theory and Experiment. *J. Phys. Chem. A* **2013**, *117* (29), 6311–6322. https://doi.org/10.1021/jp401159r.

(37) Li, Z.; Weeraman, C. N.; Gibbs-Davis, J. M. Following the Azide-Alkyne Cycloaddition at the Silica/Solvent Interface with Sum Frequency Generation. *ChemPhysChem* **2014**, *15* (11), 2247–2251. https://doi.org/10.1002/cphc.201402161.

(38) Li, Z.; N. Weeraman, C.; Shafiul Azam, M.; Osman, E.; M. Gibbs-Davis, J. The Thermal Reorganization of DNA Immobilized at the Silica/Buffer Interface: A Vibrational Sum Frequency Generation Investigation. *Phys. Chem. Chem. Phys.* **2015**, *17* (19), 12452–12457. https://doi.org/10.1039/C5CP00781J.

(39) Li, Z.; Weeraman, C. N.; Gibbs-Davis, J. M. Ketone Binding at Amino and Ureido Monolayer/Solvent Interfaces Studied by Nonlinear Optical Techniques. *J. Phys. Chem. C* **2014**, *118* (49), 28662–28670. https://doi.org/10.1021/jp509392r.

(40) Azam, Md. S.; Weeraman, C. N.; Gibbs-Davis, J. M. Specific Cation Effects on the Bimodal Acid–Base Behavior of the Silica/Water Interface. *J. Phys. Chem. Lett.* **2012**, *3* (10), 1269–1274. https://doi.org/10.1021/jz300255x.

(41) Ong, S.; Zhao, X.; Eisenthal, K. B. Polarization of Water Molecules at a Charged Interface: Second Harmonic Studies of the Silica/Water Interface. *Chem. Phys. Lett.* **1992**, *191* (3), 327–335. https://doi.org/10.1016/0009-2614(92)85309-X.

(42) Du, Q.; Freysz, E.; Shen, Y. R. Vibrational Spectra of Water Molecules at Quartz/Water Interfaces. *Phys. Rev. Lett.* **1994**, *72* (2), 238–241. https://doi.org/10.1103/PhysRevLett.72.238.

(43) Kosmulski, M. The PH Dependent Surface Charging and Points of Zero Charge. IX. Update. *Adv. Colloid Interface Sci.* **2021**, *296*, 102519. https://doi.org/10.1016/j.cis.2021.102519.

(44) Rehl, B.; Ma, E.; Parshotam, S.; DeWalt-Kerian, E. L.; Liu, T.; Geiger, F. M.; Gibbs, J. M. Water Structure in the Electrical Double Layer and the Contributions to the Total Interfacial Potential at Different Surface Charge Densities. *J. Am. Chem. Soc.* **2022**, *144* (36), 16338–16349. https://doi.org/10.1021/jacs.2c01830.

(45) Grahame, D. C. The Electrical Double Layer and the Theory of Electrocapillarity. *Chem. Rev.* **1947**, *41* (3), 441–501. https://doi.org/10.1021/cr60130a002.

(46) Luxbacher, Thomas. *The Zeta Potential for Solid Surface Analysis - A Practical Guide to Streaming Potential Measurement*; Anton Paar GmbH: Austria, 2014.

(47) Dove, P. M.; Craven, C. M. Surface Charge Density on Silica in Alkali and Alkaline Earth Chloride Electrolyte Solutions. *Geochim. Cosmochim. Acta* **2005**, *69* (21), 4963–4970. https://doi.org/10.1016/j.gca.2005.05.006.

(48) Brown, M. A.; Goel, A.; Abbas, Z. Effect of Electrolyte Concentration on the Stern Layer Thickness at a Charged Interface. *Angew. Chem. Int. Ed.* **2016**, *55* (11), 3790–3794. https://doi.org/10.1002/anie.201512025.

(49) Gmür, T. A.; Goel, A.; Brown, M. A. Quantifying Specific Ion Effects on the Surface Potential and Charge Density at Silica Nanoparticle–Aqueous Electrolyte Interfaces. *J. Phys. Chem. C* **2016**, *120* (30), 16617–16625. https://doi.org/10.1021/acs.jpcc.6b02476.
(50) Ilgen, A. G.; Kabengi, N.; Leung, K.; Ilani-Kashkouli, P.; Knight, A. W.; Loera, L. Defining Silica–Water Interfacial Chemistry under Nanoconfinement Using Lanthanides. *Environ. Sci. Nano* **2021**, *8* (2), 432–443. https://doi.org/10.1039/D0EN00971G.
(51) Gonella, G.; Backus, E. H. G.; Nagata, Y.; Bonthuis, D. J.; Loche, P.; Schlaich, A.; Netz, R. R.; Kühnle, A.; McCrum, I. T.; Koper, M. T. M.; Wolf, M.; Winter, B.; Meijer, G.; Campen, R. K.; Bonn, M. Water at Charged Interfaces. *Nat. Rev. Chem.* **2021**, *5* (7), 466–485. https://doi.org/10.1038/s41570-021-00293-2.
(52) Bloembergen, N. Nonlinear Optics and Spectroscopy. *Rev. Mod. Phys.* **1982**, *54* (3), 685–695. https://doi.org/10.1103/RevModPhys.54.685.
(53) Bloembergen, N.; Pershan, P. S. Light Waves at the Boundary of Nonlinear Media. *Phys. Rev.* **1962**, *128* (2), 606–622. https://doi.org/10.1103/PhysRev.128.606.
(54) Xu, P.; Huang, A.; Suntivich, J. Phase-Sensitive Second-Harmonic Generation of Electrochemical Interfaces. *J. Phys. Chem. Lett.* **2020**, *11* (19), 8216–8221. https://doi.org/10.1021/acs.jpclett.0c02364.
(55) Boman, F. C.; Musorrafiti, M. J.; Gibbs, J. M.; Stepp, B. R.; Salazar, A. M.; Nguyen, S. T.; Geiger, F. M. DNA Single Strands Tethered to Fused Quartz/Water Interfaces Studied by Second Harmonic Generation. *J. Am. Chem. Soc.* **2005**, *127* (44), 15368–15369. https://doi.org/10.1021/ja055468m.
(56) Stokes, G. Y.; Gibbs-Davis, J. M.; Boman, F. C.; Stepp, B. R.; Condie, A. G.; Nguyen, S. T.; Geiger, F. M. Making “Sense” of DNA. *J. Am. Chem. Soc.* **2007**, *129* (24), 7492–7493. https://doi.org/10.1021/ja071848r.
(57) Parodi, V.; Jacchetti, E.; Osellame, R.; Cerullo, G.; Polli, D.; Raimondi, M. T. Nonlinear Optical Microscopy: From Fundamentals to Applications in Live Bioimaging. *Front. Bioeng. Biotechnol.* **2020**, *8*.
(58) Mifflin, A. L.; Gerth, K. A.; Weiss, B. M.; Geiger, F. M. Surface Studies of Chromate Binding to Fused Quartz/Water Interfaces. *J. Phys. Chem. A* **2003**, *107* (32), 6212–6217. https://doi.org/10.1021/jp034308z.
(59) Mifflin, A. L.; Gerth, K. A.; Geiger, F. M. Kinetics of Chromate Adsorption and Desorption at Fused Quartz/Water Interfaces Studied by Second Harmonic Generation. *J. Phys. Chem. A* **2003**, *107* (45), 9620–9627. https://doi.org/10.1021/jp035649f.
(60) Al-Abadleh, H. A.; Voges, A. B.; Bertin, P. A.; Nguyen; Geiger, F. M. Chromium(VI) Binding to Functionalized Silica/Water Interfaces Studied by Nonlinear Optical Spectroscopy. *J. Am. Chem. Soc.* **2004**, *126* (36), 11126–11127. https://doi.org/10.1021/ja048063v.
(61) Al-Abadleh, H. A.; Mifflin, A. L.; Musorrafiti, M. J.; Geiger, F. M. Kinetic Studies of Chromium (VI) Binding to Carboxylic Acid- and Methyl Ester-Functionalized Silica/Water Interfaces Important in Geochemistry. *J. Phys. Chem. B* **2005**, *109* (35), 16852–16859. https://doi.org/10.1021/jp053006p.
(62) Al-Abadleh, H. A.; Mifflin, A. L.; Bertin, P. A.; Nguyen, S. T.; Geiger, F. M. Control of Carboxylic Acid and Ester Groups on Chromium (VI) Binding to Functionalized Silica/Water Interfaces Studied by Second Harmonic Generation. *J. Phys. Chem. B* **2005**, *109* (19), 9691–9702. https://doi.org/10.1021/jp050782o.

(63) Gonella, G.; Lütgebaucks, C.; de Beer, A. G. F.; Roke, S. Second Harmonic and Sum-Frequency Generation from Aqueous Interfaces Is Modulated by Interference. *J. Phys. Chem. C* **2016**, *120* (17), 9165–9173. https://doi.org/10.1021/acs.jpcc.5b12453.
(64) Wen, Y.-C.; Zha, S.; Liu, X.; Yang, S.; Guo, P.; Shi, G.; Fang, H.; Shen, Y. R.; Tian, C. Unveiling Microscopic Structures of Charged Water Interfaces by Surface-Specific Vibrational Spectroscopy. *Phys. Rev. Lett.* **2016**, *116* (1), 016101. https://doi.org/10.1103/PhysRevLett.116.016101.
(65) Cai, C.; Azam, Md. S.; Hore, D. K. Determining the Surface Potential of Charged Aqueous Interfaces Using Nonlinear Optical Methods. *J. Phys. Chem. C* **2021**, *125* (45), 25307–25315. https://doi.org/10.1021/acs.jpcc.1c07761.
(66) Ohno, P. E.; Saslow, S. A.; Wang, H.; Geiger, F. M.; Eisenthal, K. B. Phase-Referenced Nonlinear Spectroscopy of the α-Quartz/Water Interface. *Nat. Commun.* **2016**, *7* (1), 13587. https://doi.org/10.1038/ncomms13587.
(67) Hore, D. K.; Tyrode, E. Probing Charged Aqueous Interfaces Near Critical Angles: Effect of Varying Coherence Length. *J. Phys. Chem. C* **2019**, *123* (27), 16911–16920. https://doi.org/10.1021/acs.jpcc.9b05256.
(68) Schaefer, J.; Gonella, G.; Bonn, M.; G. Backus, E. H. Surface-Specific Vibrational Spectroscopy of the Water/Silica Interface: Screening and Interference. *Phys. Chem. Chem. Phys.* **2017**, *19* (25), 16875–16880. https://doi.org/10.1039/C7CP02251D.
(69) Rehl, B.; Gibbs, J. M. Role of Ions on the Surface-Bound Water Structure at the Silica/Water Interface: Identifying the Spectral Signature of Stability. *J. Phys. Chem. Lett.* **2021**, *12* (11), 2854–2864. https://doi.org/10.1021/acs.jpclett.0c03565.
(70) Ma, E.; Geiger, F. M. Divalent Ion Specific Outcomes on Stern Layer Structure and Total Surface Potential at the Silica:Water Interface. *J. Phys. Chem. A* **2021**, *125* (46), 10079–10088. https://doi.org/10.1021/acs.jpca.1c08143.
(71) Boamah, M. D.; Ohno, P. E.; Lozier, E.; Van Ardenne, J.; Geiger, F. M. Specifics about Specific Ion Adsorption from Heterodyne-Detected Second Harmonic Generation. *J. Phys. Chem. B* **2019**, *123* (27), 5848–5856. https://doi.org/10.1021/acs.jpcb.9b04425.
(72) Ohno, P. E.; Chang, H.; Spencer, A. P.; Liu, Y.; Boamah, M. D.; Wang, H.; Geiger, F. M. Beyond the Gouy–Chapman Model with Heterodyne-Detected Second Harmonic Generation. *J. Phys. Chem. Lett.* **2019**, *10* (10), 2328–2334. https://doi.org/10.1021/acs.jpclett.9b00727.
(73) Rehl, B.; Rashwan, M.; DeWalt-Kerian, E. L.; Jarisz, T. A.; Darlington, A. M.; Hore, D. K.; Gibbs, J. M. New Insights into χ(3) Measurements: Comparing Nonresonant Second Harmonic Generation and Resonant Sum Frequency Generation at the Silica/Aqueous Electrolyte Interface. *J. Phys. Chem. C* **2019**, *123* (17), 10991–11000. https://doi.org/10.1021/acs.jpcc.9b01300.
(74) Dreier, L. B.; Bernhard, C.; Gonella, G.; Backus, E. H. G.; Bonn, M. Surface Potential of a Planar Charged Lipid–Water Interface. What Do Vibrating Plate Methods, Second Harmonic and Sum Frequency Measure? *J. Phys. Chem. Lett.* **2018**, *9* (19), 5685–5691. https://doi.org/10.1021/acs.jpclett.8b02093.
(75) Stack, A. G.; Higgins, S. R.; Eggleston, C. M. Point of Zero Charge of a Corundum-Water Interface Probed with Optical Second Harmonic Generation (SHG) and Atomic Force Microscopy (AFM): New Approaches to Oxide Surface Charge. *Geochim. Cosmochim. Acta* **2001**, *65* (18), 3055–3063. https://doi.org/10.1016/S0016-7037(01)00649-4.

(76) Fitts, J. P.; Shang, X.; Flynn, G. W.; Heinz, T. F.; Eisenthal, K. B. Electrostatic Surface Charge at Aqueous/α-Al2O3 Single-Crystal Interfaces as Probed by Optical Second-Harmonic Generation. *J. Phys. Chem. B* **2005**, *109* (16), 7981–7986. https://doi.org/10.1021/jp040297d.

(77) Fitts, J. P.; Machesky, M. L.; Wesolowski, D. J.; Shang, X.; Kubicki, J. D.; Flynn, G. W.; Heinz, T. F.; Eisenthal, K. B. Second-Harmonic Generation and Theoretical Studies of Protonation at the Water/α-TiO2 (110) Interface. *Chem. Phys. Lett.* **2005**, *411* (4), 399–403. https://doi.org/10.1016/j.cplett.2005.03.152.

(78) Myalitsin, A.; Urashima, S.; Nihonyanagi, S.; Yamaguchi, S.; Tahara, T. Water Structure at the Buried Silica/Aqueous Interface Studied by Heterodyne-Detected Vibrational Sum-Frequency Generation. *J. Phys. Chem. C* **2016**, *120* (17), 9357–9363. https://doi.org/10.1021/acs.jpcc.6b03275.

(79) Chang, H.; Ohno, P. E.; Liu, Y.; Lozier, E. H.; Dalchand, N.; Geiger, F. M. Direct Measurement of Charge Reversal on Lipid Bilayers Using Heterodyne-Detected Second Harmonic Generation Spectroscopy. *J. Phys. Chem. B* **2020**, *124* (4), 641–649. https://doi.org/10.1021/acs.jpcb.9b09341.

(80) Dalstein, L.; Chiang, K.-Y.; Wen, Y.-C. Direct Quantification of Water Surface Charge by Phase-Sensitive Second Harmonic Spectroscopy. *J. Phys. Chem. Lett.* **2019**, *10* (17), 5200–5205. https://doi.org/10.1021/acs.jpclett.9b02156.

(81) Ma, E.; Ohno, P. E.; Kim, J.; Liu, Y.; Lozier, E. H.; Miller, T. F.; Wang, H.-F.; Geiger, F. M. A New Imaginary Term in the Second-Order Nonlinear Susceptibility from Charged Interfaces. *J. Phys. Chem. Lett.* **2021**, *12* (24), 5649–5659. https://doi.org/10.1021/acs.jpclett.1c01103.

(82) Marchioro, A.; Bischoff, M.; Lütgebaucks, C.; Biriukov, D.; Předota, M.; Roke, S. Surface Characterization of Colloidal Silica Nanoparticles by Second Harmonic Scattering: Quantifying the Surface Potential and Interfacial Water Order. *J. Phys. Chem. C* **2019**, *123* (33), 20393–20404. https://doi.org/10.1021/acs.jpcc.9b05482.

(83) Wang, H.; Hu, X.-H.; Wang, H.-F. Charge-Induced χ(3) Susceptibility in Interfacial Nonlinear Optical Spectroscopy Beyond the Bulk Aqueous Contributions: The Case for Silica/Water Interface. *J. Phys. Chem. C* **2021**, *125* (47), 26208–26215. https://doi.org/10.1021/acs.jpcc.1c08263.

(84) Guyot-Sionnest, P.; Hunt, J. H.; Shen, Y. R. Sum-Frequency Vibrational Spectroscopy of a Langmuir Film: Study of Molecular Orientation of a Two-Dimensional System. *Phys. Rev. Lett.* **1987**, *59* (14), 1597–1600. https://doi.org/10.1103/PhysRevLett.59.1597.

(85) Zhu, X. D.; Suhr, H.; Shen, Y. R. Surface Vibrational Spectroscopy by Infrared-Visible Sum Frequency Generation. *Phys. Rev. B* **1987**, *35* (6), 3047–3050. https://doi.org/10.1103/PhysRevB.35.3047.

(86) DeWalt-Kerian, E. L.; Kim, S.; Azam, Md. S.; Zeng, H.; Liu, Q.; Gibbs, J. M. PH-Dependent Inversion of Hofmeister Trends in the Water Structure of the Electrical Double Layer. *J. Phys. Chem. Lett.* **2017**, *8* (13), 2855–2861. https://doi.org/10.1021/acs.jpclett.7b01005.

(87) Lo Nostro, P.; Ninham, B. W. Hofmeister Phenomena: An Update on Ion Specificity in Biology. *Chem. Rev.* **2012**, *112* (4), 2286–2322. https://doi.org/10.1021/cr200271j.

(88) Brown, G. E.; Henrich, V. E.; Casey, W. H.; Clark, D. L.; Eggleston, C.; Felmy, A.; Goodman, D. W.; Grätzel, M.; Maciel, G.; McCarthy, M. I.; Nealson, K. H.; Sverjensky, D. A.; Toney, M. F.; Zachara, J. M. Metal Oxide Surfaces and Their Interactions with

Aqueous Solutions and Microbial Organisms. *Chem. Rev.* **1999**, *99* (1), 77–174. https://doi.org/10.1021/cr980011z.

(89) Gaigeot, M.-P.; Sprik, M.; Sulpizi, M. Oxide/Water Interfaces: How the Surface Chemistry Modifies Interfacial Water Properties. *J. Phys. Condens. Matter* **2012**, *24* (12), 124106. https://doi.org/10.1088/0953-8984/24/12/124106.

(90) Cimas, Á.; Tielens, F.; Sulpizi, M.; Gaigeot, M.-P.; Costa, D. The Amorphous Silica–Liquid Water Interface Studied by Ab Initio Molecular Dynamics (AIMD): Local Organization in Global Disorder. *J. Phys. Condens. Matter* **2014**, *26* (24), 244106. https://doi.org/10.1088/0953-8984/26/24/244106.

(91) Pezzotti, S.; Galimberti, D. R.; Shen, Y. R.; Gaigeot, M.-P. Structural Definition of the BIL and DL: A New Universal Methodology to Rationalize Non-Linear $\chi(2)(\omega)$ SFG Signals at Charged Interfaces, Including $\chi(3)(\omega)$ Contributions. *Phys. Chem. Chem. Phys.* **2018**, *20* (7), 5190–5199. https://doi.org/10.1039/C7CP06110B.

(92) Urashima, S.; Myalitsin, A.; Nihonyanagi, S.; Tahara, T. The Topmost Water Structure at a Charged Silica/Aqueous Interface Revealed by Heterodyne-Detected Vibrational Sum Frequency Generation Spectroscopy. *J. Phys. Chem. Lett.* **2018**, *9* (14), 4109–4114. https://doi.org/10.1021/acs.jpclett.8b01650.

(93) Wang, H.; Xu, Q.; Liu, Z.; Tang, Y.; Wei, G.; Shen, Y. R.; Liu, W.-T. Gate-Controlled Sum-Frequency Vibrational Spectroscopy for Probing Charged Oxide/Water Interfaces. *J. Phys. Chem. Lett.* **2019**, *10* (19), 5943–5948. https://doi.org/10.1021/acs.jpclett.9b01908.

(94) Inoue, K.; Nihonyanagi, S.; Singh, P. C.; Yamaguchi, S.; Tahara, T. 2D Heterodyne-Detected Sum Frequency Generation Study on the Ultrafast Vibrational Dynamics of H2O and HOD Water at Charged Interfaces. *J. Chem. Phys.* **2015**, *142* (21), 212431. https://doi.org/10.1063/1.4918644.

(95) Morawietz, T.; Marsalek, O.; Pattenaude, S. R.; Streacker, L. M.; Ben-Amotz, D.; Markland, T. E. The Interplay of Structure and Dynamics in the Raman Spectrum of Liquid Water over the Full Frequency and Temperature Range. *J. Phys. Chem. Lett.* **2018**, *9* (4), 851–857. https://doi.org/10.1021/acs.jpclett.8b00133.

(96) Morita, A.; Hynes, J. T. A Theoretical Analysis of the Sum Frequency Generation Spectrum of the Water Surface. *Chem. Phys.* **2000**, *258* (2), 371–390. https://doi.org/10.1016/S0301-0104(00)00127-0.

(97) Jena, K. C.; Covert, P. A.; Hore, D. K. The Effect of Salt on the Water Structure at a Charged Solid Surface: Differentiating Second- and Third-Order Nonlinear Contributions. *J. Phys. Chem. Lett.* **2011**, *2* (9), 1056–1061. https://doi.org/10.1021/jz200251h.

(98) Richmond, G. L. Molecular Bonding and Interactions at Aqueous Surfaces as Probed by Vibrational Sum Frequency Spectroscopy. *Chem. Rev.* **2002**, *102* (8), 2693–2724. https://doi.org/10.1021/cr0006876.

(99) Ostroverkhov, V.; Waychunas, G. A.; Shen, Y. R. New Information on Water Interfacial Structure Revealed by Phase-Sensitive Surface Spectroscopy. *Phys. Rev. Lett.* **2005**, *94* (4), 046102. https://doi.org/10.1103/PhysRevLett.94.046102.

(100) Ostroverkhov, V.; Waychunas, G. A.; Shen, Y. R. Vibrational Spectra of Water at Water/α-Quartz (0001) Interface. *Chem. Phys. Lett.* **2004**, *386* (1), 144–148. https://doi.org/10.1016/j.cplett.2004.01.047.

(101) Shen, Y. R. 1998 Frank Isakson Prize Address Sum Frequency Generation for Vibrational Spectroscopy: Applications to Water Interfaces and Films of Water and Ice.

Solid State Commun. **1998**, *108* (7), 399–406. https://doi.org/10.1016/S0038-1098(98)00399-8.

(102) Liljeblad, J. F. D.; Furó, I.; Tyrode, E. C. The Premolten Layer of Ice next to a Hydrophilic Solid Surface: Correlating Adhesion with Molecular Properties. *Phys. Chem. Chem. Phys.* **2016**, *19* (1), 305–317. https://doi.org/10.1039/C6CP05303C.

(103) Sovago, M.; Kramer Campen, R.; Bakker, H. J.; Bonn, M. Hydrogen Bonding Strength of Interfacial Water Determined with Surface Sum-Frequency Generation. *Chem. Phys. Lett.* **2009**, *470* (1), 7–12. https://doi.org/10.1016/j.cplett.2009.01.009.

(104) Sovago, M.; Campen, R. K.; Wurpel, G. W. H.; Müller, M.; Bakker, H. J.; Bonn, M. Vibrational Response of Hydrogen-Bonded Interfacial Water Is Dominated by Intramolecular Coupling. *Phys. Rev. Lett.* **2008**, *100* (17), 173901. https://doi.org/10.1103/PhysRevLett.100.173901.

(105) Auer, B. M.; Skinner, J. L. IR and Raman Spectra of Liquid Water: Theory and Interpretation. *J. Chem. Phys.* **2008**, *128* (22), 224511. https://doi.org/10.1063/1.2925258.

(106) Falk, M.; Ford, T. A. Infrared Spectrum and Structure of Liquid Water. *Can. J. Chem.* **1966**, *44* (14), 1699–1707. https://doi.org/10.1139/v66-255.

(107) Kananenka, A. A.; Skinner, J. L. Fermi Resonance in OH-Stretch Vibrational Spectroscopy of Liquid Water and the Water Hexamer. *J. Chem. Phys.* **2018**, *148* (24), 244107. https://doi.org/10.1063/1.5037113.

(108) Ortíz-Trejo, F.; Trejo-Valdez, M.; Campos-López, J. P.; Castro-Chacón, J. H.; Torres-Torres, C. Multipath Data Storage by Third-Order Nonlinear Optical Properties in Zinc Oxide Nanostructures. *Appl. Sci.* **2020**, *10* (16), 5688. https://doi.org/10.3390/app10165688.

(109) Chen, C.; Liu, G. Recent Advances in Nonlinear Optical and Electro-Optical Materials. *Annu. Rev. Mater. Sci.* **1986**, *16* (1), 203–243. https://doi.org/10.1146/annurev.ms.16.080186.001223.

(110) Schneider, T. *Nonlinear Optics in Telecommunications*; Advanced Texts in Physics; Springer Berlin Heidelberg: Berlin, Heidelberg, 2004. https://doi.org/10.1007/978-3-662-08996-5.

(111) Gindre, D.; Champigny, E.; Iliopoulos, K.; Sallé, M. 3D Optical Data Storage by Nonlinear Processes in Thin Films of Coumarin-Containing Copolymers. In *2013 15th International Conference on Transparent Optical Networks (ICTON)*; 2013; pp 1–1. https://doi.org/10.1109/ICTON.2013.6602833.

(112) Oudar, J. L.; Chemla, D. S. Hyperpolarizabilities of the Nitroanilines and Their Relations to the Excited State Dipole Moment. *J. Chem. Phys.* **1977**, *66* (6), 2664–2668. https://doi.org/10.1063/1.434213.

(113) Levine, B. F. Donor—Acceptor Charge Transfer Contributions to the Second Order Hyperpolarizability. *Chem. Phys. Lett.* **1976**, *37* (3), 516–520. https://doi.org/10.1016/0009-2614(76)85027-0.

(114) Levine, B. F.; Bethea, C. G. Molecular Hyperpolarizabilities Determined from Conjugated and Nonconjugated Organic Liquids. *Appl. Phys. Lett.* **1974**, *24* (9), 445–447. https://doi.org/10.1063/1.1655254.

(115) Levine, B. F.; Bethea, C. G. Effects on Hyperpolarizabilities of Molecular Interactions in Associating Liquid Mixtures. *J. Chem. Phys.* **1976**, *65* (6), 2429–2438. https://doi.org/10.1063/1.433359.

(116) Preface: New Materials for a New Age. In *Nonlinear Optical Properties of Organic Molecules and Crystals*; Chemla, D. S., Zyss, J., Eds.; Academic Press, 1987; pp ix–xiii. https://doi.org/10.1016/B978-0-12-170611-1.50004-8.

(117) Oudar, J. L. Optical Nonlinearities of Conjugated Molecules. Stilbene Derivatives and Highly Polar Aromatic Compounds. *J. Chem. Phys.* **1977**, *67* (2), 446–457. https://doi.org/10.1063/1.434888.

(118) Kaatz, P.; Donley, E. A.; Shelton, D. P. A Comparison of Molecular Hyperpolarizabilities from Gas and Liquid Phase Measurements. *J. Chem. Phys.* **1998**, *108* (3), 849–856. https://doi.org/10.1063/1.475448.

(119) Clays, K.; Persoons, A. Hyper-Rayleigh Scattering in Solution with Tunable Femtosecond Continuous-wave Laser Source. *Rev. Sci. Instrum.* **1994**, *65* (7), 2190–2194. https://doi.org/10.1063/1.1144725.

(120) Clays, K.; Persoons, A. Hyper-Rayleigh Scattering in Solution. *Phys. Rev. Lett.* **1991**, *66* (23), 2980–2983. https://doi.org/10.1103/PhysRevLett.66.2980.

(121) Shelton, D. P.; Rice, J. E. Measurements and Calculations of the Hyperpolarizabilities of Atoms and Small Molecules in the Gas Phase. *Chem. Rev.* **1994**, *94* (1), 3–29. https://doi.org/10.1021/cr00025a001.

(122) Whittall, I. R.; McDonagh, A. M.; Humphrey, M. G.; Samoc, M. Organometallic Complexes in Nonlinear Optics I: Second-Order Nonlinearities. In *Advances in Organometallic Chemistry*; Stone, F. G. A., West, R., Eds.; Academic Press, 1998; Vol. 42, pp 291–362. https://doi.org/10.1016/S0065-3055(08)60545-6.

(123) Stadler, S.; Bourhill, G.; Bräuchle, C. Problems Associated with Hyper-Rayleigh Scattering as a Means To Determine the Second-Order Polarizability of Organic Chromophores. *J. Phys. Chem.* **1996**, *100* (17), 6927–6934. https://doi.org/10.1021/jp9535102.

(124) Helgaker, T.; Coriani, S.; Jørgensen, P.; Kristensen, K.; Olsen, J.; Ruud, K. Recent Advances in Wave Function-Based Methods of Molecular-Property Calculations. *Chem. Rev.* **2012**, *112* (1), 543–631. https://doi.org/10.1021/cr2002239.

(125) Cohen, H. D.; Roothaan, C. C. J. Electric Dipole Polarizability of Atoms by the Hartree—Fock Method. I. Theory for Closed-Shell Systems. *J. Chem. Phys.* **1965**, *43* (10), S34–S39. https://doi.org/10.1063/1.1701512.

(126) Patel, A. H. G.; Mohammed, A. A. K.; Limacher, P. A.; Ayers, P. W. Finite Field Method for Nonlinear Optical Property Prediction Using Rational Function Approximants. *J. Phys. Chem. A* **2017**, *121* (28), 5313–5323. https://doi.org/10.1021/acs.jpca.7b04049.

(127) Orr, B. J.; Ward, J. F. Perturbation Theory of the Non-Linear Optical Polarization of an Isolated System. *Mol. Phys.* **1971**, *20* (3), 513–526. https://doi.org/10.1080/00268977100100481.

(128) Ward, J. F. Calculation of Nonlinear Optical Susceptibilities Using Diagrammatic Perturbation Theory. *Rev. Mod. Phys.* **1965**, *37* (1), 1–18. https://doi.org/10.1103/RevModPhys.37.1.

(129) Franken, P. A.; Ward, J. F. Optical Harmonics and Nonlinear Phenomena. *Rev. Mod. Phys.* **1963**, *35* (1), 23–39. https://doi.org/10.1103/RevModPhys.35.23.

(130) Alam, M. M.; Beerepoot, M. T. P.; Ruud, K. A Generalized Few-State Model for the First Hyperpolarizability. *J. Chem. Phys.* **2020**, *152* (24), 244106. https://doi.org/10.1063/5.0010231.

(131) Kurtz, H. A.; Dudis, D. S. Quantum Mechanical Methods for Predicting Nonlinear Optical Properties. In *Reviews in Computational Chemistry*; Lipkowitz, K. B., Boyd, D. B., Eds.; John Wiley & Sons, Inc.: Hoboken, NJ, USA, 2007; pp 241–279. https://doi.org/10.1002/9780470125892.ch5.

(132) Luo, Y.; Ågren, H.; Vahtras, O.; Jørgensen, P. The Hyperpolarizability Dispersion of Para-Nitroaniline. *Chem. Phys. Lett.* **1993**, *207* (2–3), 190–194. https://doi.org/10.1016/0009-2614(93)87013-S.

(133) Pedersen, T. B. Introduction to Response Theory. In *Handbook of Computational Chemistry*; Leszczynski, J., Ed.; Springer Netherlands: Dordrecht, 2012; pp 135–156. https://doi.org/10.1007/978-94-007-0711-5_5.

(134) Jensen, F. *Introduction to Computational Chemistry*, 2nd ed.; John Wiley & Sons: Chichester, England ; Hoboken, NJ, 2007.

(135) Norman, P.; Bishop, D. M.; Jensen, H. J. Aa.; Oddershede, J. Nonlinear Response Theory with Relaxation: The First-Order Hyperpolarizability. *J. Chem. Phys.* **2005**, *123* (19), 194103. https://doi.org/10.1063/1.2107627.

(136) Perdew, J. P.; Schmidt, K. Jacob's Ladder of Density Functional Approximations for the Exchange-Correlation Energy. *AIP Conf. Proc.* **2001**, *577* (1), 1–20. https://doi.org/10.1063/1.1390175.

(137) Kurth, S.; Perdew, J. P.; Blaha, P. Molecular and Solid-State Tests of Density Functional Approximations: LSD, GGAs, and Meta-GGAs. *Int. J. Quantum Chem. 75* (4).

(138) Champagne, B.; Perpète, E. A.; van Gisbergen, S. J. A.; Baerends, E.-J.; Snijders, J. G.; Soubra-Ghaoui, C.; Robins, K. A.; Kirtman, B. Assessment of Conventional Density Functional Schemes for Computing the Polarizabilities and Hyperpolarizabilities of Conjugated Oligomers: An *Ab Initio* Investigation of Polyacetylene Chains. *J. Chem. Phys.* **1998**, *109* (23), 10489–10498. https://doi.org/10.1063/1.477731.

(139) Champagne, B.; Perpète, E. A.; Jacquemin, D.; van Gisbergen, S. J. A.; Baerends, E.-J.; Soubra-Ghaoui, C.; Robins, K. A.; Kirtman, B. Assessment of Conventional Density Functional Schemes for Computing the Dipole Moment and (Hyper)Polarizabilities of Push−Pull π-Conjugated Systems. *J. Phys. Chem. A* **2000**, *104* (20), 4755–4763. https://doi.org/10.1021/jp993839d.

(140) Grüning, M.; Gritsenko, O. V.; van Gisbergen, S. J. A.; Jan Baerends, E. On the Required Shape Corrections to the Local Density and Generalized Gradient Approximations to the Kohn–Sham Potentials for Molecular Response Calculations of (Hyper)Polarizabilities and Excitation Energies. *J. Chem. Phys.* **2002**, *116* (22), 9591–9601. https://doi.org/10.1063/1.1476007.

(141) Karna, S. P.; Prasad, P. N.; Dupuis, M. Nonlinear Optical Properties of *p* -nitroaniline: An *Ab Initio* Time-dependent Coupled Perturbed Hartree–Fock Study. *J. Chem. Phys.* **1991**, *94* (2), 1171–1181. https://doi.org/10.1063/1.460024.

(142) Matsuzawa, N.; Dixon, D. A. Semiempirical Calculations of Hyperpolarizabilities for Donor-Acceptor Molecules: Comparison to Experiment. *J. Phys. Chem.* **1992**, *96* (15), 6232–6241. https://doi.org/10.1021/j100194a027.

(143) Burland, D. M.; Kajzar, F.; Sentein, C.; Walsh, C. A. Comparison of Hyperpolarizabilities Obtained with Different Experimental Methods and Theoretical Techniques. *J. Opt. Soc. Am. B* **1991**, *8* (11), 2269. https://doi.org/10.1364/JOSAB.8.002269.

(144) Suponitsky, K. Yu.; Tafur, S.; Masunov, A. E. Applicability of Hybrid Density Functional Theory Methods to Calculation of Molecular Hyperpolarizability. *J. Chem. Phys.* **2008**, *129* (4), 044109. https://doi.org/10.1063/1.2936121.

(145) Dreuw, A.; Head-Gordon, M. Failure of Time-Dependent Density Functional Theory for Long-Range Charge-Transfer Excited States: The Zincbacteriochlorin−Bacteriochlorin and Bacteriochlorophyll−Spheroidene Complexes. *J. Am. Chem. Soc.* **2004**, *126* (12), 4007–4016. https://doi.org/10.1021/ja039556n.

(146) Dreuw, A.; Weisman, J. L.; Head-Gordon, M. Long-Range Charge-Transfer Excited States in Time-Dependent Density Functional Theory Require Non-Local Exchange. *J. Chem. Phys.* **2003**, *119* (6), 2943–2946. https://doi.org/10.1063/1.1590951.

(147) Cohen, A. J.; Mori-Sánchez, P.; Yang, W. Challenges for Density Functional Theory. *Chem. Rev.* **2012**, *112* (1), 289–320. https://doi.org/10.1021/cr200107z.

(148) Autschbach, J. Charge-Transfer Excitations and Time-Dependent Density Functional Theory: Problems and Some Proposed Solutions. *ChemPhysChem* **2009**, *10* (11), 1757–1760. https://doi.org/10.1002/cphc.200900268.

(149) Tozer, D. J. Relationship between Long-Range Charge-Transfer Excitation Energy Error and Integer Discontinuity in Kohn–Sham Theory. *J. Chem. Phys.* **2003**, *119* (24), 12697–12699. https://doi.org/10.1063/1.1633756.

(150) Perdew, J. P.; Ruzsinszky, A.; Constantin, L. A.; Sun, J.; Csonka, G. I. Some Fundamental Issues in Ground-State Density Functional Theory: A Guide for the Perplexed. *J. Chem. Theory Comput.* **2009**, *5* (4), 902–908. https://doi.org/10.1021/ct800531s.

(151) Savin, A.; Flad, H.-J. Density Functionals for the Yukawa Electron-Electron Interaction. *Int. J. Quantum Chem.* **1995**, *56* (4), 327–332. https://doi.org/10.1002/qua.560560417.

(152) Leininger, T.; Stoll, H.; Werner, H.-J.; Savin, A. Combining Long-Range Configuration Interaction with Short-Range Density Functionals. *Chem. Phys. Lett.* **1997**, *275* (3–4), 151–160. https://doi.org/10.1016/S0009-2614(97)00758-6.

(153) Iikura, H.; Tsuneda, T.; Yanai, T.; Hirao, K. A Long-Range Correction Scheme for Generalized-Gradient-Approximation Exchange Functionals. *J. Chem. Phys.* **2001**, *115* (8), 3540–3544. https://doi.org/10.1063/1.1383587.

(154) de Wergifosse, M.; Champagne, B. Electron Correlation Effects on the First Hyperpolarizability of Push–Pull π-Conjugated Systems. *J. Chem. Phys.* **2011**, *134* (7), 074113. https://doi.org/10.1063/1.3549814.

(155) Garza, A. J.; Scuseria, G. E.; Khan, S. B.; Asiri, A. M. Assessment of Long-Range Corrected Functionals for the Prediction of Non-Linear Optical Properties of Organic Materials. *Chem. Phys. Lett.* **2013**, *575*, 122–125. https://doi.org/10.1016/j.cplett.2013.04.081.

(156) Garza, A.; Scuseria, G.; Khan, S.; Asiri, A. Erratum to “Assessment of Long-Range Corrected Functionals for the Prediction of Non-Linear Optical Properties of Organic Materials” [Chem. Phys. Lett. 575 (2013) 122–125]. *Chem. Phys. Lett.* **2013**, *579*, 137. https://doi.org/10.1016/j.cplett.2013.06.025.

(157) Lu, S.-I. Assessment of the Global and Range-Separated Hybrids for Computing the Dynamic Second-Order Hyperpolarizability of Solution-Phase Organic Molecules. *Theor. Chem. Acc.* **2013**, *133* (2), 1439. https://doi.org/10.1007/s00214-013-1439-4.

(158) Kamiya, M.; Sekino, H.; Tsuneda, T.; Hirao, K. Nonlinear Optical Property Calculations by the Long-Range-Corrected Coupled-Perturbed Kohn–Sham Method. *J. Chem. Phys.* **2005**, *122* (23), 234111. https://doi.org/10.1063/1.1935514.

(159) Perpète, E. A.; Jacquemin, D.; Adamo, C.; Scuseria, G. E. Revisiting the Nonlinear Optical Properties of Polybutatriene and Polydiacetylene with Density Functional Theory. *Chem. Phys. Lett.* **2008**, *456* (1), 101–104. https://doi.org/10.1016/j.cplett.2008.02.086.

(160) Song, J.-W.; Watson, M. A.; Sekino, H.; Hirao, K. Nonlinear Optical Property Calculations of Polyynes with Long-Range Corrected Hybrid Exchange-Correlation Functionals. *J. Chem. Phys.* **2008**, *129* (2), 024117. https://doi.org/10.1063/1.2936830.

(161) Day, P. N.; Pachter, R.; Nguyen, K. A. Analysis of Nonlinear Optical Properties in Donor–Acceptor Materials. *J. Chem. Phys.* **2014**, *140* (18), 184308. https://doi.org/10.1063/1.4874267.

(162) Egger, D. A.; Weissman, S.; Refaely-Abramson, S.; Sharifzadeh, S.; Dauth, M.; Baer, R.; Kümmel, S.; Neaton, J. B.; Zojer, E.; Kronik, L. Outer-Valence Electron Spectra of Prototypical Aromatic Heterocycles from an Optimally Tuned Range-Separated Hybrid Functional. *J. Chem. Theory Comput.* **2014**, *10* (5), 1934–1952. https://doi.org/10.1021/ct400956h.

(163) Baer, R.; Livshits, E.; Salzner, U. Tuned Range-Separated Hybrids in Density Functional Theory. *Annu. Rev. Phys. Chem.* **2010**, *61* (1), 85–109. https://doi.org/10.1146/annurev.physchem.012809.103321.

(164) Kronik, L.; Kümmel, S. Dielectric Screening Meets Optimally Tuned Density Functionals. *Adv. Mater.* **2018**, *30* (41), 1706560. https://doi.org/10.1002/adma.201706560.

(165) Rohrdanz, M. A.; Martins, K. M.; Herbert, J. M. A Long-Range-Corrected Density Functional That Performs Well for Both Ground-State Properties and Time-Dependent Density Functional Theory Excitation Energies, Including Charge-Transfer Excited States. *J. Chem. Phys.* **2009**, *130* (5), 054112. https://doi.org/10.1063/1.3073302.

(166) Refaely-Abramson, S.; Baer, R.; Kronik, L. Fundamental and Excitation Gaps in Molecules of Relevance for Organic Photovoltaics from an Optimally Tuned Range-Separated Hybrid Functional. *Phys. Rev. B* **2011**, *84* (7), 075144. https://doi.org/10.1103/PhysRevB.84.075144.

(167) Stein, T.; Eisenberg, H.; Kronik, L.; Baer, R. Fundamental Gaps in Finite Systems from Eigenvalues of a Generalized Kohn-Sham Method. *Phys. Rev. Lett.* **2010**, *105* (26), 266802. https://doi.org/10.1103/PhysRevLett.105.266802.

(168) Stein, T.; Kronik, L.; Baer, R. Reliable Prediction of Charge Transfer Excitations in Molecular Complexes Using Time-Dependent Density Functional Theory. *J. Am. Chem. Soc.* **2009**, *131* (8), 2818–2820. https://doi.org/10.1021/ja8087482.

(169) Stein, T.; Kronik, L.; Baer, R. Prediction of Charge-Transfer Excitations in Coumarin-Based Dyes Using a Range-Separated Functional Tuned from First Principles. *J. Chem. Phys.* **2009**, *131* (24), 244119. https://doi.org/10.1063/1.3269029.

(170) Kronik, L.; Stein, T.; Refaely-Abramson, S.; Baer, R. Excitation Gaps of Finite-Sized Systems from Optimally Tuned Range-Separated Hybrid Functionals. *J. Chem. Theory Comput.* **2012**, *8* (5), 1515–1531. https://doi.org/10.1021/ct2009363.

(171) Koopmans, T. Über die Zuordnung von Wellenfunktionen und Eigenwerten zu den Einzelnen Elektronen Eines Atoms. *Physica* **1934**, *1* (1), 104–113. https://doi.org/10.1016/S0031-8914(34)90011-2.

(172) Garza, A. J.; Osman, O. I.; Asiri, A. M.; Scuseria, G. E. Can Gap Tuning Schemes of Long-Range Corrected Hybrid Functionals Improve the Description of Hyperpolarizabilities? *J. Phys. Chem. B* **2015**, *119* (3), 1202–1212. https://doi.org/10.1021/jp507226v.

(173) Garza, A. J.; Wazzan, N. A.; Asiri, A. M.; Scuseria, G. E. Can Short- and Middle-Range Hybrids Describe the Hyperpolarizabilities of Long-Range Charge-Transfer Compounds? *J. Phys. Chem. A* **2014**, *118* (50), 11787–11796. https://doi.org/10.1021/jp510062b.

(174) *Non-Linear Optical Properties of Matter: From Molecules to Condensed Phases*; Papadopoulos, M. G., Sadlej, A. J., Leszczynski, J., Eds.; Challenges and advances in computational chemistry and physics; Springer: Dordrecht, 2006.

(175) *Nonlinear Optical Effects and Materials*; Günter, P., Ed.; Springer Series in Optical Sciences; Springer Berlin Heidelberg: Berlin, Heidelberg, 2000; Vol. 72. https://doi.org/10.1007/978-3-540-49713-4.

(176) Marder, S. R. Organic Nonlinear Optical Materials: Where We Have Been and Where We Are Going. *Chem. Commun.* **2006**, No. 2, 131–134. https://doi.org/10.1039/B512646K.

(177) Lescos, L.; Sitkiewicz, S. P.; Beaujean, P.; Blanchard-Desce, M.; Champagne, B.; Matito, E.; Castet, F. Performance of DFT Functionals for Calculating the Second-Order Nonlinear Optical Properties of Dipolar Merocyanines. *Phys. Chem. Chem. Phys.* **2020**, *22* (29), 16579–16594. https://doi.org/10.1039/D0CP02992K.

(178) de Wergifosse, M.; Grimme, S. Perspective on Simplified Quantum Chemistry Methods for Excited States and Response Properties. *J. Phys. Chem. A* **2021**, *125* (18), 3841–3851. https://doi.org/10.1021/acs.jpca.1c02362.

(179) Teng, C. C.; Garito, A. F. Dispersion of the Nonlinear Second-Order Optical Susceptibility of Organic Systems. *Phys. Rev. B* **1983**, *28* (12), 6766–6773. https://doi.org/10.1103/PhysRevB.28.6766.

(180) Reis, H. Problems in the Comparison of Theoretical and Experimental Hyperpolarizabilities Revisited. *J. Chem. Phys.* **2006**, *125* (1), 014506. https://doi.org/10.1063/1.2211611.

(181) Paley, M. S.; Harris, J. M.; Looser, H.; Baumert, J. C.; Bjorklund, G. C.; Jundt, D.; Twieg, R. J. A Solvatochromic Method for Determining Second-Order Polarizabilities of Organic Molecules. *J. Org. Chem.* **1989**, *54* (16), 3774–3778. https://doi.org/10.1021/jo00277a007.

(182) Sim, F.; Chin, S.; Dupuis, M.; Rice, J. E. Electron Correlation Effects in Hyperpolarizabilities of P-Nitroaniline. *J. Phys. Chem.* **1993**, *97* (6), 1158–1163. https://doi.org/10.1021/j100108a010.

(183) Sałek, P.; Helgaker, T.; Vahtras, O.; Ågren, H.; Jonsson ⊥, D.; Gauss, J. A Comparison of Density-Functional-Theory and Coupled-Cluster Frequency-Dependent Polarizabilities and Hyperpolarizabilities. *Mol. Phys.* **2005**, *103* (2–3), 439–450. https://doi.org/10.1080/00268970412331319254.

(184) Norman, P.; Luo, Y.; Jonsson, D.; Ågren, H.; Sylvester-Hvid, K. O.; Mikkelsen, K. V. Hyperpolarizability Depolarization Ratios of Nitroanilines. *J. Chem. Phys.* **1997**, *107* (21), 9063–9066. https://doi.org/10.1063/1.475196.

(185) Cheng, L. T.; Tam, W.; Stevenson, S. H.; Meredith, G. R.; Rikken, G.; Marder, S. R. Experimental Investigations of Organic Molecular Nonlinear Optical Polarizabilities. 1. Methods and Results on Benzene and Stilbene Derivatives. *J. Phys. Chem.* **1991**, *95* (26), 10631–10643. https://doi.org/10.1021/j100179a026.

(186) Marder, S. R.; Beratan, D. N.; Cheng, L.-T. Approaches for Optimizing the First Electronic Hyperpolarizability of Conjugated Organic Molecules. *Science* **1991**, *252* (5002), 103–106. https://doi.org/10.1126/science.252.5002.103.

(187) Hammond, J. R.; Kowalski, K. Parallel Computation of Coupled-Cluster Hyperpolarizabilities. *J. Chem. Phys.* **2009**, *130* (19), 194108. https://doi.org/10.1063/1.3134744.

(188) Tawada, Y.; Tsuneda, T.; Yanagisawa, S.; Yanai, T.; Hirao, K. A Long-Range-Corrected Time-Dependent Density Functional Theory. *J. Chem. Phys.* **2004**, *120* (18), 8425–8433. https://doi.org/10.1063/1.1688752.

(189) Vydrov, O. A.; Scuseria, G. E. Assessment of a Long-Range Corrected Hybrid Functional. *J. Chem. Phys.* **2006**, *125* (23), 234109. https://doi.org/10.1063/1.2409292.

(190) Toulouse, J.; Colonna, F.; Savin, A. Long-Range--Short-Range Separation of the Electron-Electron Interaction in Density-Functional Theory. *Phys. Rev. A* **2004**, *70* (6), 062505. https://doi.org/10.1103/PhysRevA.70.062505.

(191) Kirtman, B.; Bonness, S.; Ramirez-Solis, A.; Champagne, B.; Matsumoto, H.; Sekino, H. Calculation of Electric Dipole (Hyper)Polarizabilities by Long-Range-Correction Scheme in Density Functional Theory: A Systematic Assessment for Polydiacetylene and Polybutatriene Oligomers. *J. Chem. Phys.* **2008**, *128* (11), 114108. https://doi.org/10.1063/1.2885051.

(192) Sekino, H.; Maeda, Y.; Kamiya, M.; Hirao, K. Polarizability and Second Hyperpolarizability Evaluation of Long Molecules by the Density Functional Theory with Long-Range Correction. *J. Chem. Phys.* **2007**, *126* (1), 014107. https://doi.org/10.1063/1.2428291.

(193) Autschbach, J.; Srebro, M. Delocalization Error and “Functional Tuning” in Kohn–Sham Calculations of Molecular Properties. *Acc. Chem. Res.* **2014**, *47* (8), 2592–2602. https://doi.org/10.1021/ar500171t.

(194) Nénon, S.; Champagne, B.; Spassova, M. I. Assessing Long-Range Corrected Functionals with Physically-Adjusted Range-Separated Parameters for Calculating the Polarizability and the Second Hyperpolarizability of Polydiacetylene and Polybutatriene Chains. *Phys. Chem. Chem. Phys.* **2014**, *16* (15), 7083–7088. https://doi.org/10.1039/C4CP00105B.

(195) Kronik, L.; Stein, T.; Refaely-Abramson, S.; Baer, R. Excitation Gaps of Finite-Sized Systems from Optimally Tuned Range-Separated Hybrid Functionals. *J. Chem. Theory Comput.* **2012**, *8* (5), 1515–1531. https://doi.org/10.1021/ct2009363.

(196) Sun, H.; Autschbach, J. Influence of the Delocalization Error and Applicability of Optimal Functional Tuning in Density Functional Calculations of Nonlinear Optical Properties of Organic Donor–Acceptor Chromophores. *ChemPhysChem* **2013**, *14* (11), 2450–2461. https://doi.org/10.1002/cphc.201300256.

(197) Garrett, K.; Sosa Vazquez, X.; Egri, S. B.; Wilmer, J.; Johnson, L. E.; Robinson, B. H.; Isborn, C. M. Optimum Exchange for Calculation of Excitation Energies and Hyperpolarizabilities of Organic Electro-Optic Chromophores. *J. Chem. Theory Comput.* **2014**, *10* (9), 3821–3831. https://doi.org/10.1021/ct500528z.

(198) Ye, J.-T.; Liu, J.-H.; Zhang, Q.; Qiu, Y.-Q.; Wang, L.-H. Tuning of Second-Order Nonlinear Optical Properties Based on [2.2]Paracyclophanes Isomer: The Relative Configuration and Polarizable Environment. *J. Phys. Chem. C* **2020**, *124* (39), 21692–21701. https://doi.org/10.1021/acs.jpcc.0c05980.

(199) Frisch, M. J.; Trucks, G. W.; Schlegel, H. B.; Scuseria, G. E.; Robb, M. A.; Cheeseman, J. R.; Scalmani, G.; Barone, V.; Petersson, G. A.; Nakatsuji, H.; Li, X.; Caricato, M.; Marenich, A. V.; Bloino, J.; Janesko, B. G.; Gomperts, R.; Mennucci, B.; Hratchian, H. P.; Ortiz, J. V.; Izmaylov, A. F.; Sonnenberg, J. L.; Williams-Young, D.; Ding, F.; Lipparini, F.; Egidi, F.; Goings, J.; Peng, B.; Petrone, A.; Henderson, T.; Ranasinghe, D.; Zakrzewski, V. G.; Gao, J.; Rega, N.; Zheng, G.; Liang, W.; Hada, M.; Ehara, M.; Toyota, K.; Fukuda, R.; Hasegawa, J.; Ishida, M.; Nakajima, T.; Honda, Y.; Kitao, O.; Nakai, H.; Vreven, T.; Throssell, K.; Montgomery, J. A., Jr.; Peralta, J. E.; Ogliaro, F.; Bearpark, M. J.; Heyd, J. J.; Brothers, E. N.; Kudin, K. N.; Staroverov, V. N.; Keith, T. A.; Kobayashi, R.; Normand, J.; Raghavachari, K.; Rendell, A. P.; Burant, J. C.; Iyengar, S. S.; Tomasi, J.; Cossi, M.; Millam, J. M.; Klene, M.; Adamo, C.; Cammi, R.; Ochterski, J. W.; Martin, R. L.; Morokuma, K.; Farkas, O.; Foresman, J. B.; Fox, D. J. Gaussian 16 Revision C.01, 2016.

(200) Aidas, K.; Angeli, C.; Bak, K. L.; Bakken, V.; Bast, R.; Boman, L.; Christiansen, O.; Cimiraglia, R.; Coriani, S.; Dahle, P.; Dalskov, E. K.; Ekström, U.; Enevoldsen, T.; Eriksen, J. J.; Ettenhuber, P.; Fernández, B.; Ferrighi, L.; Fliegl, H.; Frediani, L.; Hald, K.; Halkier, A.; Hättig, C.; Heiberg, H.; Helgaker, T.; Hennum, A. C.; Hettema, H.; Hjertenæs, E.; Høst, S.; Høyvik, I.-M.; Iozzi, M. F.; Jansík, B.; Jensen, H. J. Aa.; Jonsson, D.; Jørgensen, P.; Kauczor, J.; Kirpekar, S.; Kjærgaard, T.; Klopper, W.; Knecht, S.; Kobayashi, R.; Koch, H.; Kongsted, J.; Krapp, A.; Kristensen, K.; Ligabue, A.; Lutnæs, O. B.; Melo, J. I.; Mikkelsen, K. V.; Myhre, R. H.; Neiss, C.; Nielsen, C. B.; Norman, P.; Olsen, J.; Olsen, J. M. H.; Osted, A.; Packer, M. J.; Pawlowski, F.; Pedersen, T. B.; Provasi, P. F.; Reine, S.; Rinkevicius, Z.; Ruden, T. A.; Ruud, K.; Rybkin, V. V.; Sałek, P.; Samson, C. C. M.; de Merás, A. S.; Saue, T.; Sauer, S. P. A.; Schimmelpfennig, B.; Sneskov, K.; Steindal, A. H.; Sylvester-Hvid, K. O.; Taylor, P. R.; Teale, A. M.; Tellgren, E. I.; Tew, D. P.; Thorvaldsen, A. J.; Thøgersen, L.; Vahtras, O.; Watson, M. A.; Wilson, D. J. D.; Ziolkowski, M.; Ågren, H. The Dalton Quantum Chemistry Program System. *WIREs Comput. Mol. Sci.* **2014**, *4* (3), 269–284. https://doi.org/10.1002/wcms.1172.

(201) Yanai, T.; Tew, D. P.; Handy, N. C. A New Hybrid Exchange–Correlation Functional Using the Coulomb-Attenuating Method (CAM-B3LYP). *Chem. Phys. Lett.* **2004**, *393* (1), 51–57. https://doi.org/10.1016/j.cplett.2004.06.011.

(202) Ditchfield, R.; Hehre, W. J.; Pople, J. A. Self-Consistent Molecular-Orbital Methods. IX. An Extended Gaussian-Type Basis for Molecular-Orbital Studies of Organic Molecules. *J. Chem. Phys.* **1971**, *54* (2), 724–728. https://doi.org/10.1063/1.1674902.

(203) Hehre, W. J.; Ditchfield, R.; Pople, J. A. Self—Consistent Molecular Orbital Methods. XII. Further Extensions of Gaussian—Type Basis Sets for Use in Molecular Orbital Studies of Organic Molecules. *J. Chem. Phys.* **1972**, *56* (5), 2257–2261. https://doi.org/10.1063/1.1677527.

(204) Hariharan, P. C.; Pople, J. A. The Influence of Polarization Functions on Molecular Orbital Hydrogenation Energies. *Theor. Chim. Acta* **1973**, *28* (3), 213–222. https://doi.org/10.1007/BF00533485.

(205) Rassolov, V. A.; Ratner, M. A.; Pople, J. A.; Redfern, P. C.; Curtiss, L. A. 6-31G* Basis Set for Third-Row Atoms. *J. Comput. Chem.* **2001**, *22* (9), 976–984. https://doi.org/10.1002/jcc.1058.

(206) Francl, M. M.; Pietro, W. J.; Hehre, W. J.; Binkley, J. S.; Gordon, M. S.; DeFrees, D. J.; Pople, J. A. Self-consistent Molecular Orbital Methods. XXIII. A Polarization-type Basis

Set for Second-row Elements. *J. Chem. Phys.* **1982**, *77* (7), 3654–3665. https://doi.org/10.1063/1.444267.

(207) Gordon, M. S.; Binkley, J. S.; Pople, J. A.; Pietro, W. J.; Hehre, W. J. Self-Consistent Molecular-Orbital Methods. 22. Small Split-Valence Basis Sets for Second-Row Elements. *J. Am. Chem. Soc.* **1982**, *104* (10), 2797–2803. https://doi.org/10.1021/ja00374a017.

(208) Becke, A. D. Density-functional Thermochemistry. III. The Role of Exact Exchange. *J. Chem. Phys.* **1993**, *98* (7), 5648–5652. https://doi.org/10.1063/1.464913.

(209) Chai, J.-D.; Head-Gordon, M. Long-Range Corrected Hybrid Density Functionals with Damped Atom–Atom Dispersion Corrections. *Phys. Chem. Chem. Phys.* **2008**, *10* (44), 6615–6620. https://doi.org/10.1039/B810189B.

(210) Chai, J.-D.; Head-Gordon, M. Systematic Optimization of Long-Range Corrected Hybrid Density Functionals. *J. Chem. Phys.* **2008**, *128* (8), 084106. https://doi.org/10.1063/1.2834918.

(211) Runge, E.; Gross, E. K. U. Density-Functional Theory for Time-Dependent Systems. *Phys. Rev. Lett.* **1984**, *52* (12), 997–1000. https://doi.org/10.1103/PhysRevLett.52.997.

(212) Tomasi, J.; Mennucci, B.; Cammi, R. Quantum Mechanical Continuum Solvation Models. *Chem. Rev.* **2005**, *105* (8), 2999–3094. https://doi.org/10.1021/cr9904009.

(213) Dunning, T. H. Gaussian Basis Sets for Use in Correlated Molecular Calculations. I. The Atoms Boron through Neon and Hydrogen. *J. Chem. Phys.* **1989**, *90* (2), 1007–1023. https://doi.org/10.1063/1.456153.

(214) Kendall, R. A.; Dunning, T. H.; Harrison, R. J. Electron Affinities of the First-row Atoms Revisited. Systematic Basis Sets and Wave Functions. *J. Chem. Phys.* **1992**, *96* (9), 6796–6806. https://doi.org/10.1063/1.462569.

(215) Berkovic, G.; Meshulam, G.; Kotler, Z. Measurement and Analysis of Molecular Hyperpolarizability in the Two-Photon Resonance Regime. *J. Chem. Phys.* **2000**, *112* (9), 3997–4003. https://doi.org/10.1063/1.480991.

(216) Wang, C. H. Effects of Dephasing and Vibronic Structure on the First Hyperpolarizability of Strongly Charge-Transfer Molecules. *J. Chem. Phys.* **2000**, *112* (4), 1917–1924. https://doi.org/10.1063/1.480754.

(217) Meshulam, G.; Berkovic, G.; Kotler, Z.; Sa'ar, A. Electric Field Induced Second Harmonic Generation with and without Fringes. *Rev. Sci. Instrum.* **2000**, *71* (9), 3490–3493. https://doi.org/10.1063/1.1287629.

(218) Hu, Z.; Autschbach, J.; Jensen, L. Simulating Third-Order Nonlinear Optical Properties Using Damped Cubic Response Theory within Time-Dependent Density Functional Theory. *J. Chem. Theory Comput.* **2016**, *12* (3), 1294–1304. https://doi.org/10.1021/acs.jctc.5b01060.

(219) Willetts, A.; Rice, J. E.; Burland, D. M.; Shelton, D. P. Problems in the Comparison of Theoretical and Experimental Hyperpolarizabilities. *J. Chem. Phys.* **1992**, *97* (10), 7590–7599. https://doi.org/10.1063/1.463479.

(220) Quinet, O.; Kirtman, B.; Champagne, B. Analytical Time-Dependent Hartree-Fock Evaluation of the Dynamic Zero-Point Vibrationally Averaged (ZPVA) First Hyperpolarizability. *J. Chem. Phys.* **2003**, *118* (2), 505–513. https://doi.org/10.1063/1.1523903.

(221) Audebert, P.; Kamada, K.; Matsunaga, K.; Ohta, K. The Third-Order NLO Properties of D-π-A Molecules with Changing a Primary Amino Group into Pyrrole. *Chem. Phys. Lett.* **2003**, *367* (1), 62–71. https://doi.org/10.1016/S0009-2614(02)01575-0.

(222) Hu, Z.; Autschbach, J.; Jensen, L. Simulation of Resonance Hyper-Rayleigh Scattering of Molecules and Metal Clusters Using a Time-Dependent Density Functional Theory Approach. *J. Chem. Phys.* **2014**, *141* (12), 124305. https://doi.org/10.1063/1.4895971.

(223) Woodford, J. N.; Wang, C. H.; Asato, A. E.; Liu, R. S. H. Hyper-Rayleigh Scattering of Azulenic Donor–Acceptor Molecules at 1064 and 1907 Nm. *J. Chem. Phys.* **1999**, *111* (10), 4621–4628. https://doi.org/10.1063/1.479223.

(224) Campo, J.; Wenseleers, W.; Goovaerts, E.; Szablewski, M.; Cross, G. H. Accurate Determination and Modeling of the Dispersion of the First Hyperpolarizability of an Efficient Zwitterionic Nonlinear Optical Chromophore by Tunable Wavelength Hyper-Rayleigh Scattering. *J. Phys. Chem. C* **2008**, *112* (1), 287–296. https://doi.org/10.1021/jp0758824.

(225) Peng, J.; Guo, J.; Ma, R.; Jiang, Y. Water-Solid Interfaces Probed by High-Resolution Atomic Force Microscopy. *Surf. Sci. Rep.* **2022**, *77* (1), 100549. https://doi.org/10.1016/j.surfrep.2021.100549.

(226) Bourg, I. C.; Lee, S. S.; Fenter, P.; Tournassat, C. Stern Layer Structure and Energetics at Mica–Water Interfaces. *J. Phys. Chem. C* **2017**, *121* (17), 9402–9412. https://doi.org/10.1021/acs.jpcc.7b01828.

(227) Seki, T.; Yu, C.-C.; Chiang, K.-Y.; Tan, J.; Sun, S.; Ye, S.; Bonn, M.; Nagata, Y. Disentangling Sum-Frequency Generation Spectra of the Water Bending Mode at Charged Aqueous Interfaces. *J. Phys. Chem. B* **2021**, *125* (25), 7060–7067. https://doi.org/10.1021/acs.jpcb.1c03258.

(228) Matt, S. M.; Ben-Amotz, D. Influence of Intermolecular Coupling on the Vibrational Spectrum of Water. *J. Phys. Chem. B* **2018**, *122* (21), 5375–5380. https://doi.org/10.1021/acs.jpcb.7b11063.

(229) Cyran, J. D.; Backus, E. H. G.; Nagata, Y.; Bonn, M. Structure from Dynamics: Vibrational Dynamics of Interfacial Water as a Probe of Aqueous Heterogeneity. *J. Phys. Chem. B* **2018**, *122* (14), 3667–3679. https://doi.org/10.1021/acs.jpcb.7b10574.

(230) Schaefer, J.; Backus, E. H. G.; Nagata, Y.; Bonn, M. Both Inter- and Intramolecular Coupling of O–H Groups Determine the Vibrational Response of the Water/Air Interface. *J. Phys. Chem. Lett.* **2016**, *7* (22), 4591–4595. https://doi.org/10.1021/acs.jpclett.6b02513.

(231) Raymond, E. A.; Tarbuck, T. L.; Brown, M. G.; Richmond, G. L. Hydrogen-Bonding Interactions at the Vapor/Water Interface Investigated by Vibrational Sum-Frequency Spectroscopy of HOD/H_2O/D_2O Mixtures and Molecular Dynamics Simulations. *J. Phys. Chem. B* **2003**, *107* (2), 546–556. https://doi.org/10.1021/jp021366w.

(232) Stiopkin, I. V.; Weeraman, C.; Pieniazek, P. A.; Shalhout, F. Y.; Skinner, J. L.; Benderskii, A. V. Hydrogen Bonding at the Water Surface Revealed by Isotopic Dilution Spectroscopy. *Nature* **2011**, *474* (7350), 192–195. https://doi.org/10.1038/nature10173.

(233) Tian, C.-S.; Shen, Y. R. Isotopic Dilution Study of the Water/Vapor Interface by Phase-Sensitive Sum-Frequency Vibrational Spectroscopy. *J. Am. Chem. Soc.* **2009**, *131* (8), 2790–2791. https://doi.org/10.1021/ja809497y.

(234) Walker, D. S.; Richmond, G. L. Understanding the Effects of Hydrogen Bonding at the Vapor−Water Interface: Vibrational Sum Frequency Spectroscopy of H2O/HOD/D2O Mixtures Studied Using Molecular Dynamics Simulations. *J. Phys. Chem. C* **2007**, *111* (23), 8321–8330. https://doi.org/10.1021/jp070493v.

(235) Xu, X.; Shen, Y. R.; Tian, C. Phase-Sensitive Sum Frequency Vibrational Spectroscopic Study of Air/Water Interfaces: H2O, D2O, and Diluted Isotopic Mixtures. *J. Chem. Phys.* **2019**, *150* (14), 144701. https://doi.org/10.1063/1.5081135.

(236) Inoue, K. (井上賢一); Ahmed, M.; Nihonyanagi, S. (二本柳聡史); Tahara, T. (田原太平). Effect of Hydrogen-Bond on Ultrafast Spectral Diffusion Dynamics of Water at Charged Monolayer Interfaces. *J. Chem. Phys.* **2019**, *150* (5), 054705. https://doi.org/10.1063/1.5081077.

(237) Tuladhar, A.; Dewan, S.; Pezzotti, S.; Brigiano, F. S.; Creazzo, F.; Gaigeot, M.-P.; Borguet, E. Ions Tune Interfacial Water Structure and Modulate Hydrophobic Interactions at Silica Surfaces. *J. Am. Chem. Soc.* **2020**, *142* (15), 6991–7000. https://doi.org/10.1021/jacs.9b13273.

(238) Darlington, A. M.; Jarisz, T. A.; DeWalt-Kerian, E. L.; Roy, S.; Kim, S.; Azam, Md. S.; Hore, D. K.; Gibbs, J. M. Separating the PH-Dependent Behavior of Water in the Stern and Diffuse Layers with Varying Salt Concentration. *J. Phys. Chem. C* **2017**, *121* (37), 20229–20241. https://doi.org/10.1021/acs.jpcc.7b03522.

(239) Sulpizi, M.; Gaigeot, M.-P.; Sprik, M. The Silica–Water Interface: How the Silanols Determine the Surface Acidity and Modulate the Water Properties. *J. Chem. Theory Comput.* **2012**, *8* (3), 1037–1047. https://doi.org/10.1021/ct2007154.

(240) Glasoe, P. K.; Long, F. A. Use of Glass Electrodes to Measure Acidities in Deuterium Oxide. *J. Phys. Chem.* **1960**, *64* (1), 188–190. https://doi.org/10.1021/j100830a521.

(241) Krężel, A.; Bal, W. A Formula for Correlating PKa Values Determined in D2O and H2O. *J. Inorg. Biochem.* **2004**, *98* (1), 161–166. https://doi.org/10.1016/j.jinorgbio.2003.10.001.

(242) Hardy, R. C.; Cottington, R. L. Viscosity of Deuterium Oxide and Water from 5° to 125°C. *J. Chem. Phys.* **1949**, *17* (5), 509–510. https://doi.org/10.1063/1.1747310.

(243) Horita, J.; Cole, D. R. Stable Isotope Partitioning in Aqueous and Hydrothermal Systems to Elevated Temperatures. *Aqueous Syst. Elev. Temp. Press. Phys. Chem. Water Steam Hydrothermal Solut.* **2004**, 277–319. https://doi.org/10.1016/B978-012544461-3/50010-7.

(244) Vidulich, G. A.; Evans, D. F.; Kay, R. L. The Dielectric Constant of Water and Heavy Water between 0 and 40.Degree. *J. Phys. Chem.* **1967**, *71* (3), 656–662. https://doi.org/10.1021/j100862a028.

(245) Sovago, M.; Vartiainen, E.; Bonn, M. Erratum: "Observation of Buried Water Molecules in Phospholipid Membranes by Surface Sum-Frequency Generation Spectroscopy" [J. Chem. Phys. 131, 161107 (2009)]. *J. Chem. Phys.* **2010**, *133* (22), 229901. https://doi.org/10.1063/1.3511705.

(246) Sovago, M.; Vartiainen, E.; Bonn, M. Determining Absolute Molecular Orientation at Interfaces: A Phase Retrieval Approach for Sum Frequency Generation Spectroscopy. *J. Phys. Chem. C* **2009**, *113* (15), 6100–6106. https://doi.org/10.1021/jp810123g.

(247) Sovago, M.; Vartiainen, E.; Bonn, M. Observation of Buried Water Molecules in Phospholipid Membranes by Surface Sum-Frequency Generation Spectroscopy. *J. Chem. Phys.* **2009**, *131* (16), 161107. https://doi.org/10.1063/1.3257600.

(248) Lambert, A. G.; Davies, P. B.; Neivandt, D. J. Implementing the Theory of Sum Frequency Generation Vibrational Spectroscopy: A Tutorial Review. *Appl. Spectrosc. Rev.* **2005**, *40* (2), 103–145. https://doi.org/10.1081/ASR-200038326.

(249) Eftekhari-Bafrooei, A.; Borguet, E. Effect of Hydrogen-Bond Strength on the Vibrational Relaxation of Interfacial Water. *J. Am. Chem. Soc.* **2010**, *132* (11), 3756–3761. https://doi.org/10.1021/ja907745r.

(250) Dedic, J.; Okur, H. I.; Roke, S. Polyelectrolytes Induce Water-Water Correlations That Result in Dramatic Viscosity Changes and Nuclear Quantum Effects. *Sci. Adv.* **2019**, *5* (12), eaay1443. https://doi.org/10.1126/sciadv.aay1443.

(251) Chen, Y.; Okur, H. I.; Gomopoulos, N.; Macias-Romero, C.; Cremer, P. S.; Petersen, P. B.; Tocci, G.; Wilkins, D. M.; Liang, C.; Ceriotti, M.; Roke, S. Electrolytes Induce Long-Range Orientational Order and Free Energy Changes in the H-Bond Network of Bulk Water. *Sci. Adv.* **2016**, *2* (4), e1501891. https://doi.org/10.1126/sciadv.1501891.

(252) de Beer, A. G. F.; Chen, Y.; Scheu, R.; Conboy, J. C.; Roke, S. Analysis of Complex Spectra Using Fourier Filtering. *J. Phys. Chem. C* **2013**, *117* (50), 26582–26587. https://doi.org/10.1021/jp406161n.

(253) de Beer, A. G. F.; Samson, J.-S.; Hua, W.; Huang, Z.; Chen, X.; Allen, H. C.; Roke, S. Direct Comparison of Phase-Sensitive Vibrational Sum Frequency Generation with Maximum Entropy Method: Case Study of Water. *J. Chem. Phys.* **2011**, *135* (22), 224701. https://doi.org/10.1063/1.3662469.

(254) Hofmann, M. J.; Koelsch, P. Retrieval of Complex $\chi(2)$ Parts for Quantitative Analysis of Sum-Frequency Generation Intensity Spectra. *J. Chem. Phys.* **2015**, *143* (13), 134112. https://doi.org/10.1063/1.4932180.

(255) Johansson, P. K.; Koelsch, P. Vibrational Sum-Frequency Scattering for Detailed Studies of Collagen Fibers in Aqueous Environments. *J. Am. Chem. Soc.* **2014**, *136* (39), 13598–13601. https://doi.org/10.1021/ja508190d.

(256) Roy, S.; Covert, P. A.; Jarisz, T. A.; Chan, C.; Hore, D. K. Surface–Bulk Vibrational Correlation Spectroscopy. *Anal. Chem.* **2016**, *88* (9), 4682–4691. https://doi.org/10.1021/acs.analchem.5b04544.

(257) Yang, P.-K.; Huang, J. Y. Model-Independent Maximum-Entropy Method for the Analysis of Sum-Frequency Vibrational Spectroscopy. *J. Opt. Soc. Am. B* **2000**, *17* (7), 1216. https://doi.org/10.1364/JOSAB.17.001216.

(258) Yang, W.-C.; Hore, D. K. Broadband Models and Their Consequences on Line Shape Analysis in Vibrational Sum-Frequency Spectroscopy. *J. Chem. Phys.* **2018**, *149* (17), 174703. https://doi.org/10.1063/1.5053128.

(259) Cyran, J. D.; Donovan, M. A.; Vollmer, D.; Brigiano, F. S.; Pezzotti, S.; Galimberti, D. R.; Gaigeot, M.-P.; Bonn, M.; Backus, E. H. G. Molecular Hydrophobicity at a Macroscopically Hydrophilic Surface. *Proc. Natl. Acad. Sci.* **2019**, *116* (5), 1520–1525. https://doi.org/10.1073/pnas.1819000116.

(260) Dalstein, L.; Potapova, E.; Tyrode, E. The Elusive Silica/Water Interface: Isolated Silanols under Water as Revealed by Vibrational Sum Frequency Spectroscopy. *Phys. Chem. Chem. Phys.* **2017**, *19* (16), 10343–10349. https://doi.org/10.1039/C7CP01507K.

(261) Pezzotti, S.; Ruth Galimberti, D.; Gaigeot, M.-P. Deconvolution of BIL-SFG and DL-SFG Spectroscopic Signals Reveals Order/Disorder of Water at the Elusive Aqueous Silica Interface. *Phys. Chem. Chem. Phys.* **2019**, *21* (40), 22188–22202. https://doi.org/10.1039/C9CP02766A.

(262) Zhang, L.; Tian, C.; Waychunas, G. A.; Shen, Y. R. Structures and Charging of α-Alumina (0001)/Water Interfaces Studied by Sum-Frequency Vibrational Spectroscopy. *J. Am. Chem. Soc.* **2008**, *130* (24), 7686–7694. https://doi.org/10.1021/ja8011116.

(263) Pezzotti, S.; Serva, A.; Sebastiani, F.; Brigiano, F. S.; Galimberti, D. R.; Potier, L.; Alfarano, S.; Schwaab, G.; Havenith, M.; Gaigeot, M.-P. Molecular Fingerprints of

Hydrophobicity at Aqueous Interfaces from Theory and Vibrational Spectroscopies. *J. Phys. Chem. Lett.* **2021**, *12* (15), 3827–3836. https://doi.org/10.1021/acs.jpclett.1c00257.

(264) Kaliannan, N. K.; Henao Aristizabal, A.; Wiebeler, H.; Zysk, F.; Ohto, T.; Nagata, Y.; Kühne, T. D. Impact of Intermolecular Vibrational Coupling Effects on the Sum-Frequency Generation Spectra of the Water/Air Interface. *Mol. Phys.* **2020**, *118* (4), 1620358. https://doi.org/10.1080/00268976.2019.1620358.

(265) Moberg, D. R.; Straight, S. C.; Paesani, F. Temperature Dependence of the Air/Water Interface Revealed by Polarization Sensitive Sum-Frequency Generation Spectroscopy. *J. Phys. Chem. B* **2018**, *122* (15), 4356–4365. https://doi.org/10.1021/acs.jpcb.8b01726.

(266) Zdrali, E.; Baer, M. D.; Okur, H. I.; Mundy, C. J.; Roke, S. The Diverse Nature of Ion Speciation at the Nanoscale Hydrophobic/Water Interface. *J. Phys. Chem. B* **2019**, *123* (10), 2414–2423. https://doi.org/10.1021/acs.jpcb.8b10207.

(267) Zhao, X.; Ong, S.; Wang, H.; Eisenthal, K. B. New Method for Determination of Surface PKa Using Second Harmonic Generation. *Chem. Phys. Lett.* **1993**, *214* (2), 203–207. https://doi.org/10.1016/0009-2614(93)90082-C.

(268) Darlington, A. M.; Gibbs-Davis, J. M. Bimodal or Trimodal? The Influence of Starting PH on Site Identity and Distribution at the Low Salt Aqueous/Silica Interface. *J. Phys. Chem. C* **2015**, *119* (29), 16560–16567. https://doi.org/10.1021/acs.jpcc.5b02480.

(269) Dove, P. M.; Nix, C. J. The Influence of the Alkaline Earth Cations, Magnesium, Calcium, and Barium on the Dissolution Kinetics of Quartz. *Geochim. Cosmochim. Acta* **1997**, *61* (16), 3329–3340. https://doi.org/10.1016/S0016-7037(97)00217-2.

(270) Chen, E. H.; Saslow, S. A.; Nguyen, S. T.; Geiger, F. M. Zinc Ion–Hydroxyl Interactions at Undecanol-Functionalized Fused Silica/Water Interfaces Using the Eisenthal χ(3) Technique. *J. Phys. Chem. C* **2012**, *116* (12), 7016–7020. https://doi.org/10.1021/jp212331x.

(271) Bischoff, M.; Biriukov, D.; Předota, M.; Roke, S.; Marchioro, A. Surface Potential and Interfacial Water Order at the Amorphous TiO2 Nanoparticle/Aqueous Interface. *J. Phys. Chem. C* **2020**, *124* (20), 10961–10974. https://doi.org/10.1021/acs.jpcc.0c01158.

(272) Boamah, M. D.; Ohno, P. E.; Geiger, F. M.; Eisenthal, K. B. Relative Permittivity in the Electrical Double Layer from Nonlinear Optics. *J. Chem. Phys.* **2018**, *148* (22), 222808. https://doi.org/10.1063/1.5011977.

(273) Parshotam, S.; Rehl, B.; Busse, F.; Brown, A.; Gibbs, J. M. Influence of the Hydrogen-Bonding Environment on Vibrational Coupling in the Electrical Double Layer at the Silica/Aqueous Interface. *J. Phys. Chem. C* **2022**, *126* (51), 21734–21744. https://doi.org/10.1021/acs.jpcc.2c06412.

(274) Azam, Md. S.; Gibbs-Davis, J. M. Monitoring DNA Hybridization and Thermal Dissociation at the Silica/Water Interface Using Resonantly Enhanced Second Harmonic Generation Spectroscopy. *Anal. Chem.* **2013**, *85* (17), 8031–8038. https://doi.org/10.1021/ac401009u.

(275) Rashwan, M.; Rehl, B.; Sthoer, A.; Darlington, A. M.; Azam, Md. S.; Zeng, H.; Liu, Q.; Tyrode, E.; Gibbs, J. M. Structure of the Silica/Divalent Electrolyte Interface: Molecular Insight into Charge Inversion with Increasing PH. *J. Phys. Chem. C* **2020**, *124* (49), 26973–26981. https://doi.org/10.1021/acs.jpcc.0c09747.

(276) Frisch, M. J.; Trucks, G. W.; Schlegel, H. B.; Scuseria, G. E.; Robb, M. A.; Cheeseman, J. R.; Scalmani, G.; Barone, V.; Petersson, G. A.; Li, X.; Caricato, M.; Marenich, A. V.; Bloino, J.; Janesko, B. G.; Gomperts, R.; Mennucci, B.; Hratchian, H. P.; Ortiz, J. V.;

Izmaylov, A. F.; Sonnenberg, J. L.; Williams-Young, D.; Ding, F.; Lipparini, F.; Egidi, F.; Goings, J.; Peng, B.; Petrone, A.; Henderson, T.; Ranasinghe, D. Gaussian 16, Revision C.01, 2016.

(277) Ugliengo, P.; Sodupe, M.; Musso, F.; Bush, I. J.; Orlando, R.; Dovesi, R. Realistic Models of Hydroxylated Amorphous Silica Surfaces and MCM-41 Mesoporous Material Simulated by Large-Scale Periodic B3LYP Calculations. *Adv. Mater.* **2008**, *20* (23), 4579–4583. https://doi.org/10.1002/adma.200801489.

(278) Brkljača, Z.; Namjesnik, D.; Lützenkirchen, J.; Předota, M.; Preočanin, T. Quartz/Aqueous Electrolyte Solution Interface: Molecular Dynamic Simulation and Interfacial Potential Measurements. *J. Phys. Chem. C* **2018**, *122* (42), 24025–24036. https://doi.org/10.1021/acs.jpcc.8b04035.

(279) Azam, M. S.; Darlington, A.; Gibbs-Davis, J. M. The Influence of Concentration on Specific Ion Effects at the Silica/Water Interface. *J. Phys. Condens. Matter* **2014**, *26* (24), 244107. https://doi.org/10.1088/0953-8984/26/24/244107.

(280) Azam, Md. S.; Weeraman, C. N.; Gibbs-Davis, J. M. Halide-Induced Cooperative Acid–Base Behavior at a Negatively Charged Interface. *J. Phys. Chem. C* **2013**, *117* (17), 8840–8850. https://doi.org/10.1021/jp401164r.

(281) Lyklema, J. Overcharging, Charge Reversal: Chemistry or Physics? *Colloids Surf. Physicochem. Eng. Asp.* **2006**, *291* (1), 3–12. https://doi.org/10.1016/j.colsurfa.2006.06.043.

(282) van der Heyden, F. H. J.; Stein, D.; Besteman, K.; Lemay, S. G.; Dekker, C. Charge Inversion at High Ionic Strength Studied by Streaming Currents. *Phys. Rev. Lett.* **2006**, *96* (22), 224502. https://doi.org/10.1103/PhysRevLett.96.224502.

(283) Lovering, K. A.; Bertram, A. K.; Chou, K. C. New Information on the Ion-Identity-Dependent Structure of Stern Layer Revealed by Sum Frequency Generation Vibrational Spectroscopy. *J. Phys. Chem. C* **2016**, *120* (32), 18099–18104. https://doi.org/10.1021/acs.jpcc.6b05564.

(284) Ma, E.; Kim, J.; Chang, H.; Ohno, P. E.; Jodts, R. J.; Miller, T. F. I.; Geiger, F. M. Stern and Diffuse Layer Interactions during Ionic Strength Cycling. *J. Phys. Chem. C* **2021**, *125* (32), 18002–18014. https://doi.org/10.1021/acs.jpcc.1c04836.

(285) Hassanali, A. A.; Singer, S. J. Model for the Water−Amorphous Silica Interface: The Undissociated Surface. *J. Phys. Chem. B* **2007**, *111* (38), 11181–11193. https://doi.org/10.1021/jp062971s.

(286) Hassanali, A. A.; Zhang, H.; Knight, C.; Shin, Y. K.; Singer, S. J. The Dissociated Amorphous Silica Surface: Model Development and Evaluation. *J. Chem. Theory Comput.* **2010**, *6* (11), 3456–3471. https://doi.org/10.1021/ct100260z.

(287) Zhuravlev, L. T. The Surface Chemistry of Amorphous Silica. Zhuravlev Model. *Colloids Surf. Physicochem. Eng. Asp.* **2000**, *173* (1–3), 1–38. https://doi.org/10.1016/S0927-7757(00)00556-2.

(288) Rashwan, M.; Rehl, B.; Romaniuk, N.; Gibbs, J. M. Probing Silica–Kaolinite Interactions with Sum Frequency Generation Spectroscopy. *Langmuir* **2022**, *38* (51), 15984–15994. https://doi.org/10.1021/acs.langmuir.2c02414.

(289) Ramos, T. N.; Champagne, B. Investigation of the Second Harmonic Generation at the Water–Vacuum Interface by Using Multi-Scale Modeling Methods. *ChemistryOpen n/a* (n/a), e202200045. https://doi.org/10.1002/open.202200045.

(290) Bhandari, S.; Cheung, M. S.; Geva, E.; Kronik, L.; Dunietz, B. D. Fundamental Gaps of Condensed-Phase Organic Semiconductors from Single-Molecule Calculations Using Polarization-Consistent Optimally Tuned Screened Range-Separated Hybrid Functionals. *J. Chem. Theory Comput.* **2018**, *14* (12), 6287–6294. https://doi.org/10.1021/acs.jctc.8b00876.

(291) Stähelin, M.; Burland, D. M.; Rice, J. E. Solvent Dependence of the Second Order Hyperpolarizability in P-Nitroaniline. *Chem. Phys. Lett.* **1992**, *191* (3–4), 245–250. https://doi.org/10.1016/0009-2614(92)85295-L.

(292) Max, J.-J.; Chapados, C. Isotope Effects in Liquid Water by Infrared Spectroscopy. III. H2O and D2O Spectra from 6000to0cm−1. *J. Chem. Phys.* **2009**, *131* (18), 184505. https://doi.org/10.1063/1.3258646.

(293) Rehl, B.; Ma, E.; Parshotam, S.; DeWalt-Kerian, E. L.; Liu, T.; Geiger, F. M.; Gibbs, J. M. Water Structure in the Electrical Double Layer and the Contribution to the Total Interfacial Potential at Different Surface Charge Densities. *ChemRxiv*. https://doi.org/10.26434/chemrxiv-2022-p5fwp-v4.

Appendix A.

Appendix to Chapter 2

A1. Experimental Studies on Nitroaniline Isomers

Table A1: Experimental hyperpolarizability values of the nitroaniline isomers at various excitation wavelengths (in nm) and in different solvents.

	Reference	**λ_{ex} (nm)**	**Solvent**	**Reported β (au)**	**Converted β_z^T (au)***	**$\beta_{\|\|}$ (au)**
pNA	[185]	1907	Acetone	1065	3604	2162
	[179]	1907	1,4 dioxane	1111	2660	1596
	[179]	1370	1,4 dioxane	1366	3277	1966
	[179]	1064	1,4 dioxane	1956	4694	2816
	[179]	909	1,4 dioxane	2893	6944	4166
	[179]	830	1,4 dioxane	4629	11110	6666
	[291]	1064	1,4 dioxane	1852	4530	2718
	[115]	1064	Methanol	3703	10186	6112
	[117]	1064	Methanol	3993	9584	5750
	[181]	1064	1,4 dioxane	3356	4601	2761
oNA	[185]	1907	1,4 dioxane	289	1042	521
	[115]	1064	Acetone	1111	3066	1333
	[117]	1064	Acetone	1180	2833	1417
mNA	[185]	1907	1,4 dioxane	220	792	396
	[115]	1064	Acetone	729	2012	875
	[117]	1064	Acetone	694	1666	833

*Hyperpolarizabilities converted and corrected with calibration factors based on Reis[180] and Burland et al.[143]

A2. Optimal Gap Tuning of RSH Functionals

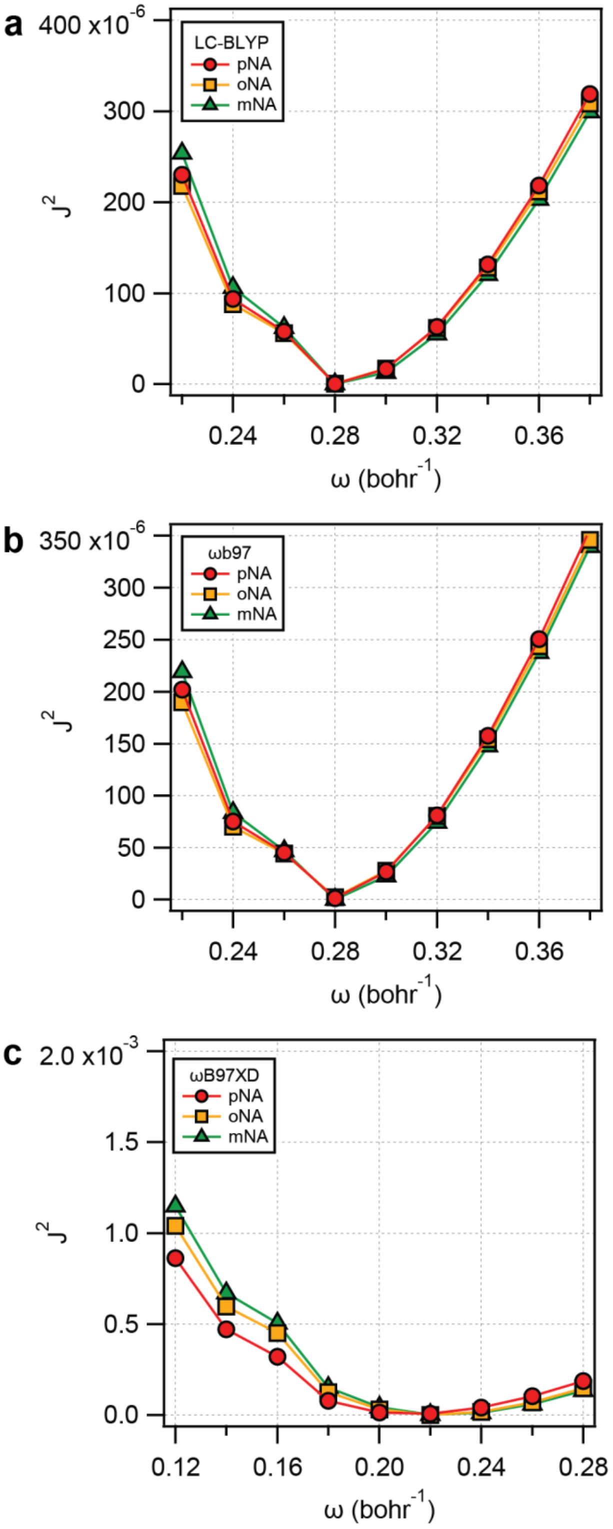

Figure A1: Absolute differences of J^2, see Equation 1 in the main text, against the range separation parameter used to determine the optimized ω values. All results were determined in the gas phase with the 6-311+G (d,p) basis set.

A3. Variation of the Hyperpolarizability for the Tuned RSH Functionals.

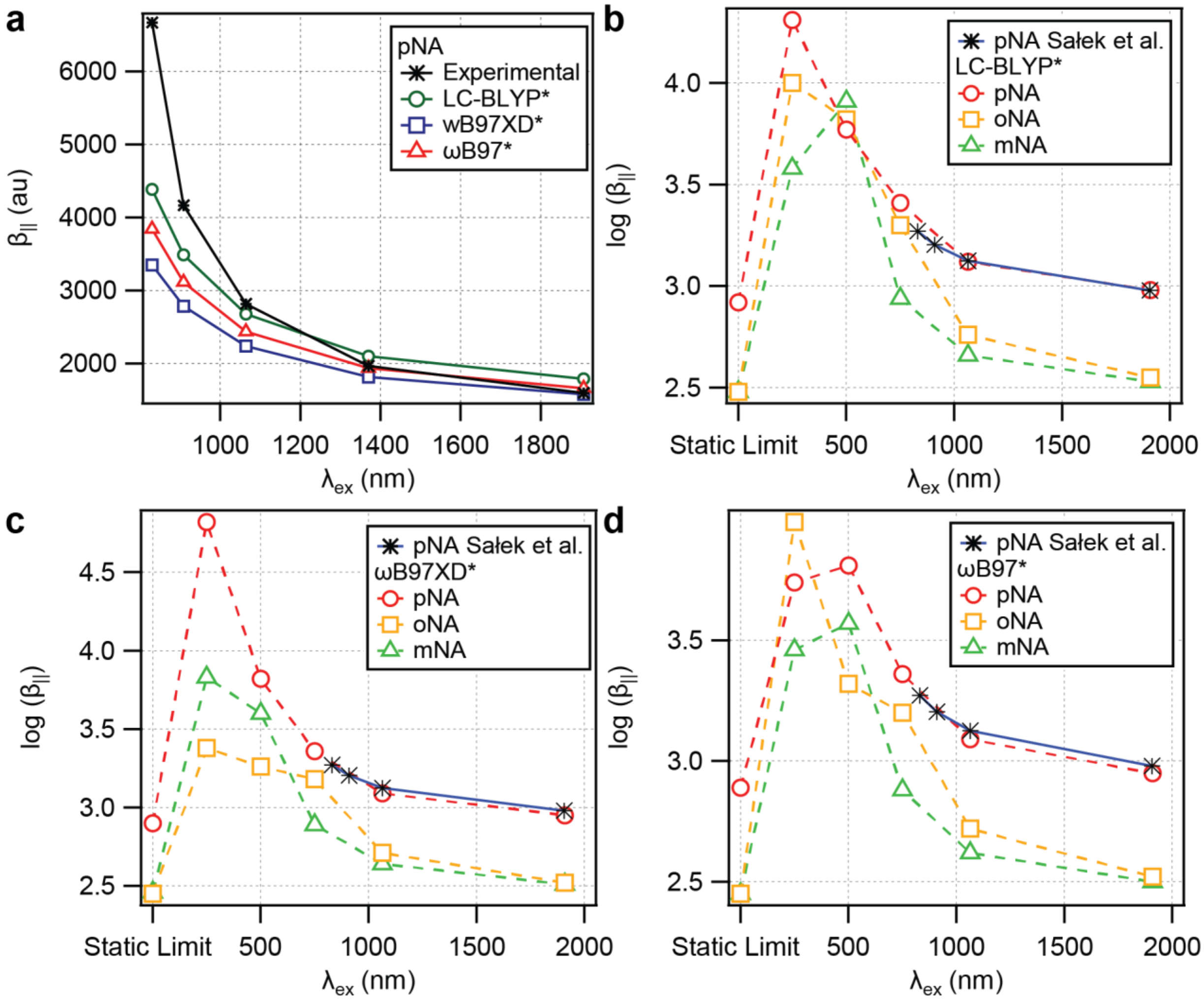

Figure A2: Variation of hyperpolarizabilities with respect to the excitation wavelengths for tuned RSH functionals (a) at excitation wavelengths and 1,4 dioxane,[179] and (b)-(d) over a broader excitation wavelength window in the gas phase. All results were determined with the 6-311+G (d,p) basis set. Previous CCSD/aug-cc-pVDZ computations on pNA are also presented.[183]

A4. TD-DFT Computations

Table A2: Energies (E) in nm with values in parenthesis given in eV and oscillator strengths (f) for the first three excited states of the nitroaniline isomers calculated with different functionals and the 6-311+G(d,p) basis set in the gas phase. Values correspond to the untuned RSH functionals.

		1st Excited State		**2nd Excited State**		**3rd Excited State**	
		E	**f**	**E**	**f**	**E**	**f**
pNA	B3LYP	323 (3.84)	0	315 (3.94)	0.3316	281 (4.42)	0.0004
	CAMB3LYP	312 (3.97)	0	284 (4.36)	0.3837	273 (4.54)	0.0005
	LC-BLYP	305 (4.07)	0	268 (4.63)	0.0005	263 (4.72)	0.4122
	ωB97	306 (4.05)	0	268 (4.62)	0.0005	264 (4.70)	0.4077
	ωB97XD	312 (3.98)	0	280 (4.43)	0.3872	273 (4.54)	0.0004
oNA	B3LYP	369 (3.36)	0.0925	320 (3.87)	0	277 (4.47)	0.0005
	CAMB3LYP	331 (3.74)	0.1338	309 (4.01)	0	269 (4.61)	0.0005
	LC-BLYP	302 (4.10)	0	302 (4.10)	0.1688	264 (4.70)	0.0005
	ωB97	306 (4.05)	0.1613	304 (4.08)	0	265 (4.68)	0.0006
	ωB97XD	330 (3.76)	0.1344	309 (4.01)	0	269 (4.60)	0.0005
mNA	B3LYP	388 (3.20)	0.0289	328 (3.78)	0	286 (4.34)	0.0003
	CAMB3LYP	323 (3.84)	0.0465	317 (3.92)	0	278 (4.46)	0.0004
	LC-BLYP	310 (4.00)	0	285 (4.35)	0.0640	273 (4.55)	0.0005
	ωB97	311 (3.99)	0	288 (4.30)	0.0606	273 (4.54)	0.0005
	ωB97XD	319 (3.88)	0.0467	316 (3.92)	0.0002	278 (4.46)	0.0004

Table A3: Energies, transition dipole moment, excited and ground state dipole moments in au, computed with CAM-B3LYP/6-311+G(d,p) in the gas phase.

	pNA	**oNA**	**mNA**
E	0.1604	0.1376	0.1411
μ_{eg}	3.589	1.4583	0.4942
μ_{e}	5.08	3.27	4.79
μ_{g}	2.84	1.99	2.30

A5. Damped Two-State Model Versus Damped Response Theory

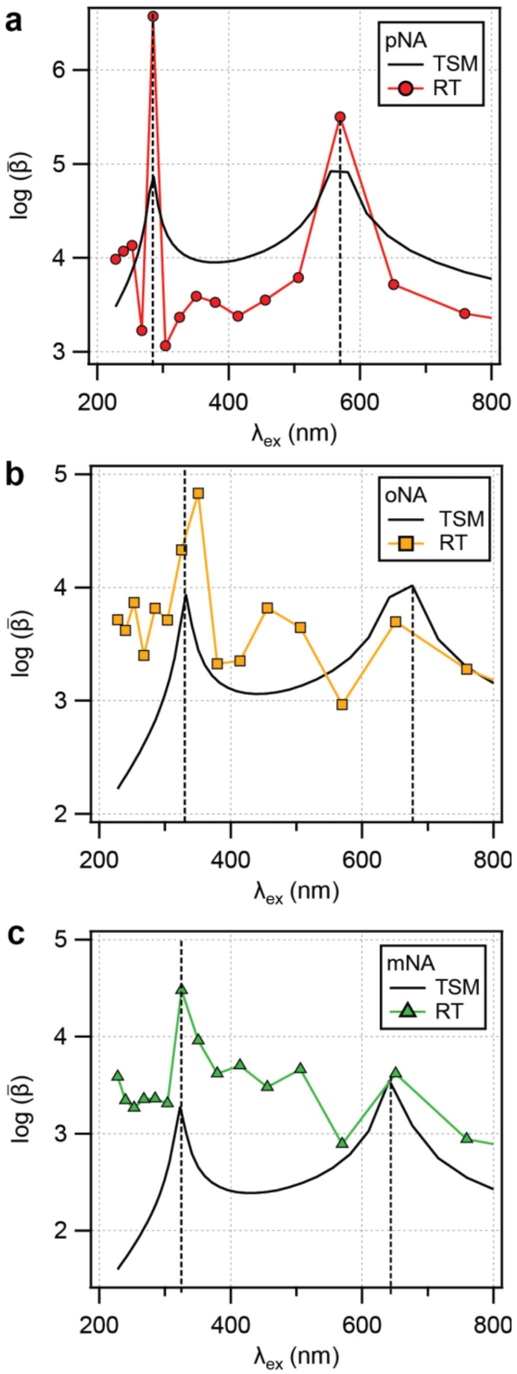

Figure A3: Hyperpolarizabilities of nitroaniline isomers computed with damped two-state model and damped response theory (damping parameter= 500 cm^{-1}). All results were determined with the CAM-B3LYP/6-311+G (d,p) in the gas phase. Dashed lines indicate pole positions.

A6. Variation of the Hyperpolarizabilities of pNA and mNA with Respect to the Range Separation Parameter in the Gas Phase

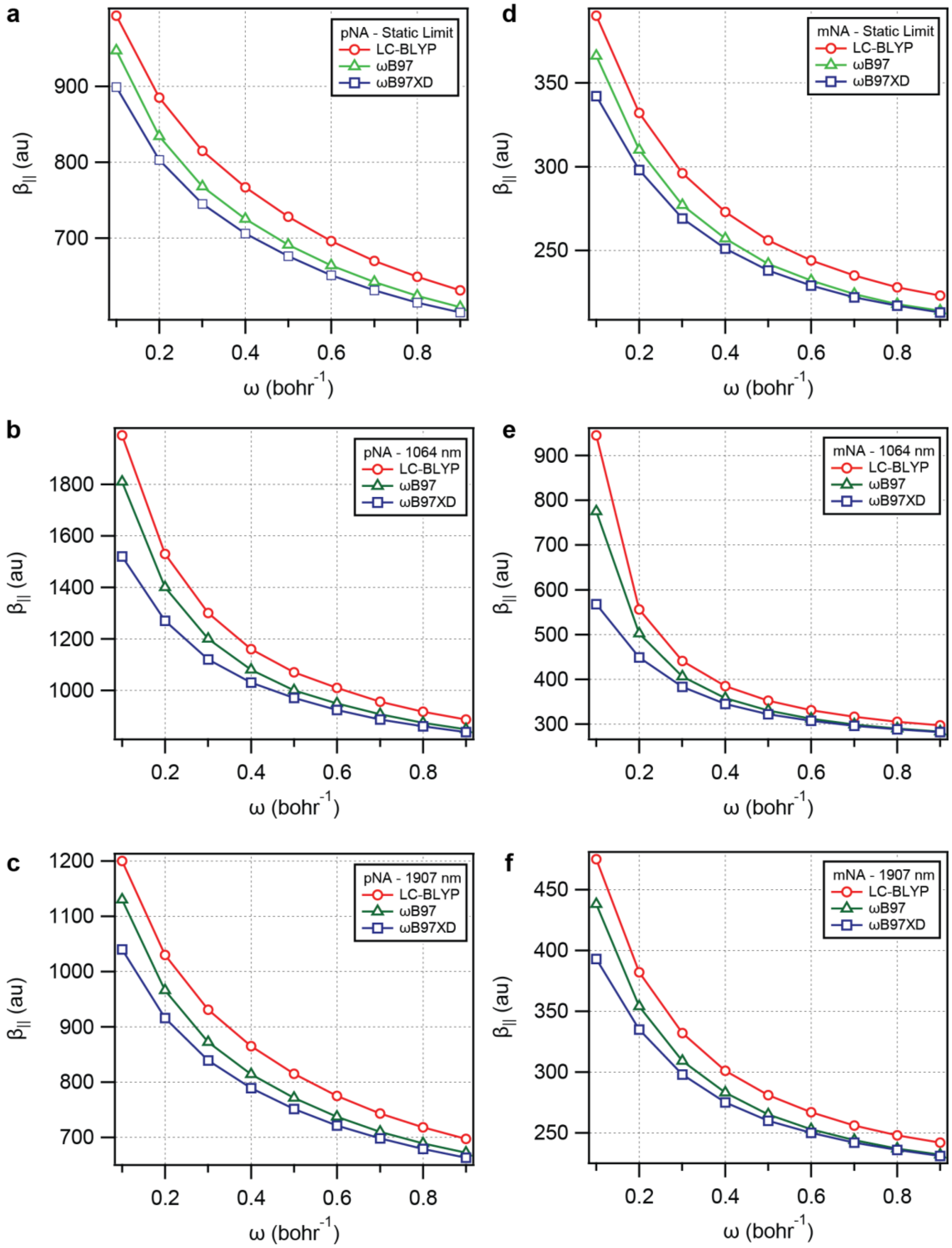

Figure A4: Variation of hyperpolarizabilities, of pNA and mNA with respect to the range separation parameter for RSH functionals at (a) the static limit (b) 1064 nm, and (c) 1907 nm computed in the gas phase. All results were determined in the gas phase with the 6-311+G (d,p) basis set.

A7. Variation of the Hyperpolarizabilities of pNA, oNA, and mNA with Respect to the Range Separation Parameter in 1,4 dioxane

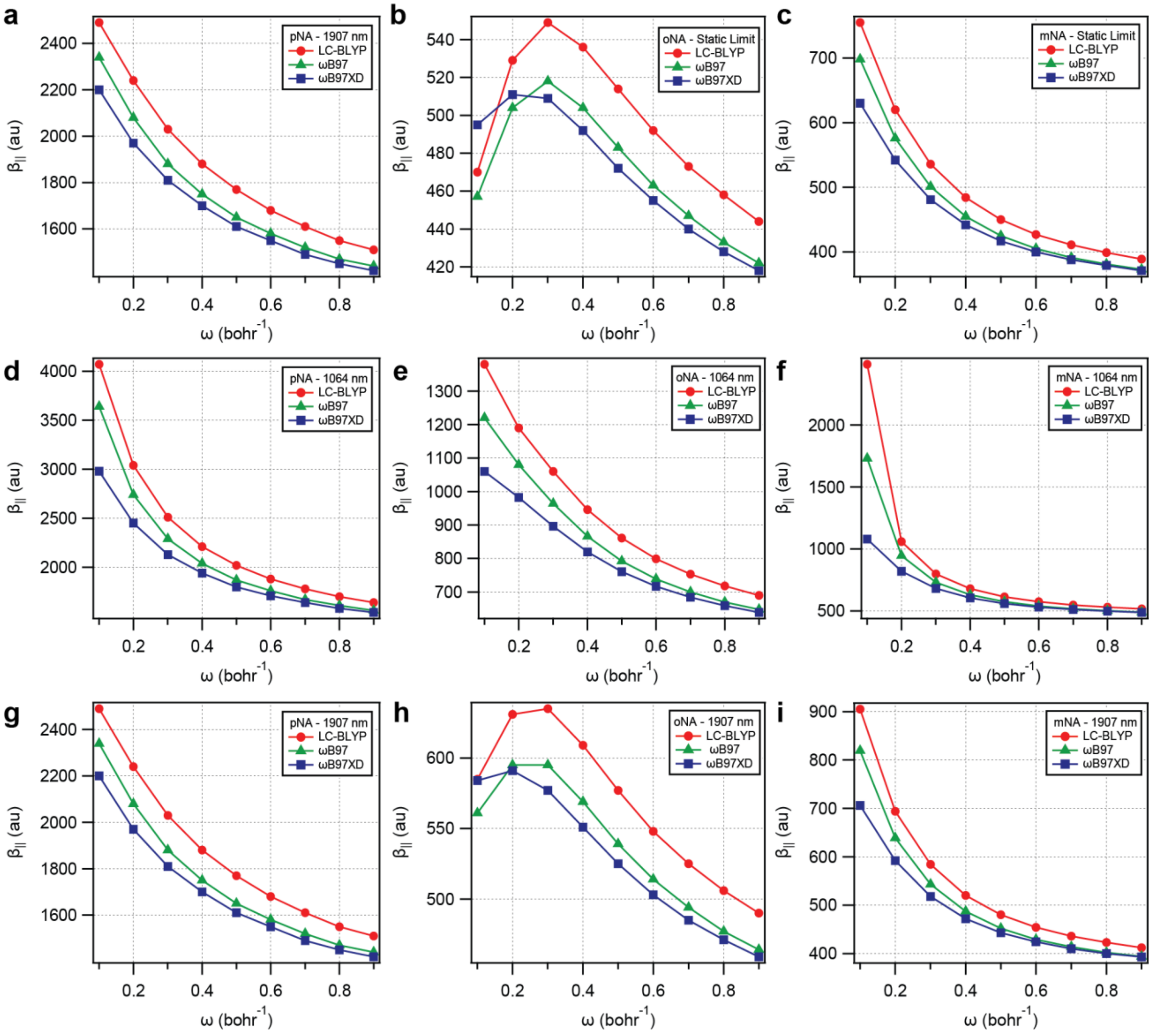

Figure A5: Variation of the hyperpolarizabilities of the nitroaniline isomers with respect to the range separation parameter for RSH functionals at (a-c) the static limit (d-f) 1064 nm, and (g-i) 1907 nm in 1,4 dioxane. All results were determined with the 6-311+G (d,p) basis set.

A8. Coordinates of Ground State Geometries

Ground state geometries as optimized with CAMB3LYP/6-31+G(d,p) in the gas phase. Values are in Å.

pNA
C,6.56862726,1.29901959,0.0006117665
C,6.56862726,2.5102427668,-0.7153267594
C,6.56862726,2.5107968909,-2.0965220832
C,6.56862726,1.29901959,-2.7812313572
C,6.56862726,0.0872422891,-2.0965220832
C,6.56862726,0.0877964132,-0.7153267594
H,6.56862726,3.4377834584,-2.6560879557
H,6.56862726,-0.8397442784,-2.6560879557
H,6.56862726,-0.8540148444,-0.1754939019
N,6.56862726,1.29901959,1.3680124912
H,6.56862726,2.1598765911,1.8873316078
H,6.56862726,0.4381625889,1.8873316078
H,6.56862726,3.4520540244,-0.1754939019
N,6.56862726,1.29901959,-4.2339976593
O,6.56862726,0.2160098761,-4.8099155282
O,6.56862726,2.3820293039,-4.8099155282
oNA
C,0,-0.4368689,1.00100399,0.
C,0,0.22767801,-0.25911406,0.
C,0,-0.49535707,-1.46414201,0.
C,0,-1.87594107,-1.46111491,0.
C,0,-2.55178399,-0.22781686,0.
C,0,-1.85568291,0.96425509,0.
H,0,-3.63774599,-0.20520879,0.
N,0,0.20324918,2.19544594,0.
H,0,1.21259018,2.20209887,0.
H,0,-0.33002776,3.04812898,0.
H,0,-2.42673314,-2.39486687,0.
H,0,-2.39066384,1.90996412,0.
H,0,0.07163686,-2.38607805,0.
N,0,1.672481,-0.35988116,0.
O,0,2.18675892,-1.47936219,0.
O,0,2.35056208,0.68668479,0.
mNA
C,-1.9054089928,0.9513910394,0.0339480155
C,-1.4694726506,-0.3693826477,0.0379236179
C,-0.1003293101,-0.5841292303,-0.0033615549
C,0.8301450154,0.4415639433,-0.0468867123
C,0.3796501515,1.7644645495,-0.0499787299
C,-1.001469903,2.0039484583,-0.0098804304
H,1.8860070953,0.2032062671,-0.0822533335

H,-1.3642772207,3.0276112063,-0.0185310006
H,-2.1536393924,-1.2059026026,0.0719311706
H,-2.9686921049,1.1637652241,0.0653627226
N,1.2802289536,2.8146847034,-0.1417785431
H,0.9588082747,3.7221340291,0.1583310642
H,2.2377567119,2.6210061938,0.1088101968
N,0.3985223673,-1.9694065882,0.0025052296
O,-0.425467278,-2.8718244818,0.0382725101
O,1.6095314529,-2.1417783837,-0.0281043625

Appendix B.

Appendix to Chapter 3

B1. Correction for Local Field Effects at the Silica/HOD Interface

A more detailed version of the correction of the local field effects at the silica/water interface can be found in our previous work.[44,69] For the silica/HOD interface, we use the same approach with the main difference lying in the refractive indices of HOD in D_2O, where the refractive indices are calculated as the weighted average of the H_2O and D_2O refractive indices based on values reported by Max and Chapados[292]. The effect of correcting the SSP vSFG spectra for local field effects is shown in Figure B1. Local field corrections were not done for the PPP spectra as in addition to the $\chi^{(2)}_{XXZ}$, they require knowledge of the $\chi^{(2)}_{ZXX}$ and $\chi^{(2)}_{XZX}$ the tensor elements.

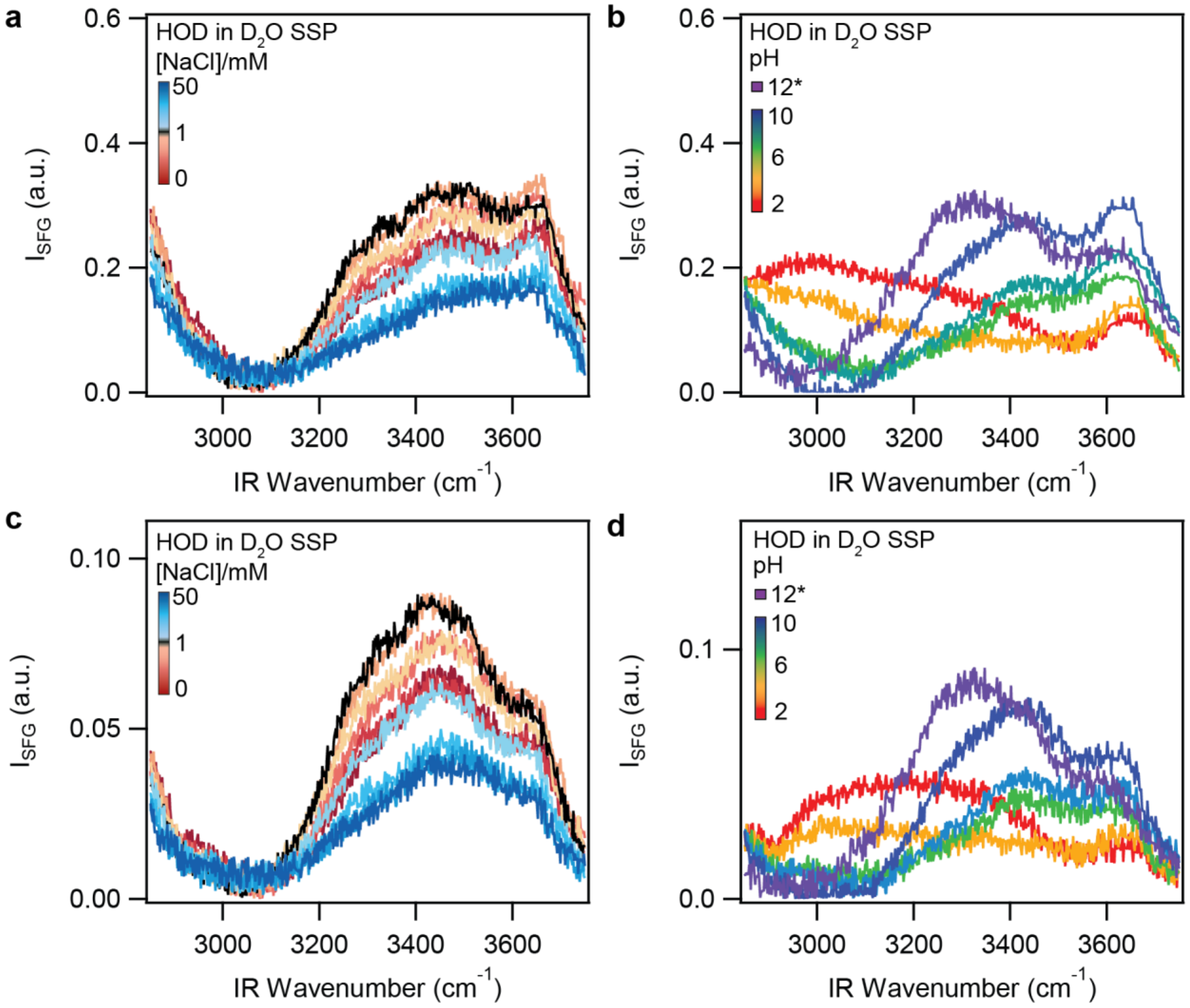

Figure B1: Representative vSFG spectra of the silica/HOD interface with varying (a and c) ionic strength and (b and d) pH: (a and b) before and (c and d) after local field corrections. The spectra are normalized to the intensity at 3200 cm^{-1} measured at the silica/10 mM NaCl water interface for the same sample on the same day.

B2. Ionic strength Dependent PPP spectra of H_2O and HOD

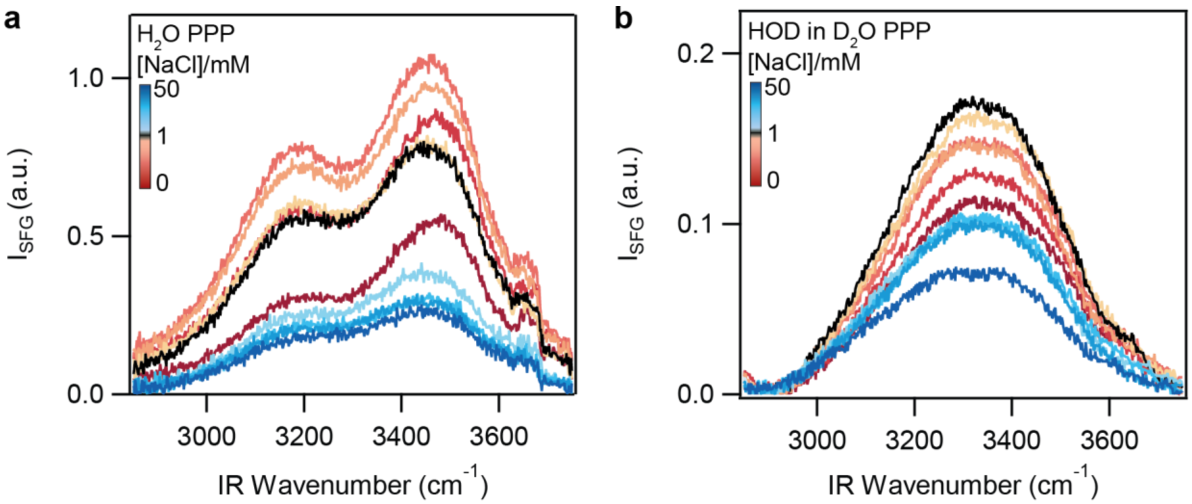

Figure B2: Representative PPP intensity spectra of (a) H_2O and (b) HOD in D_2O collected as the ionic strength was varied.

B3. Electrokinetic Charge Densities

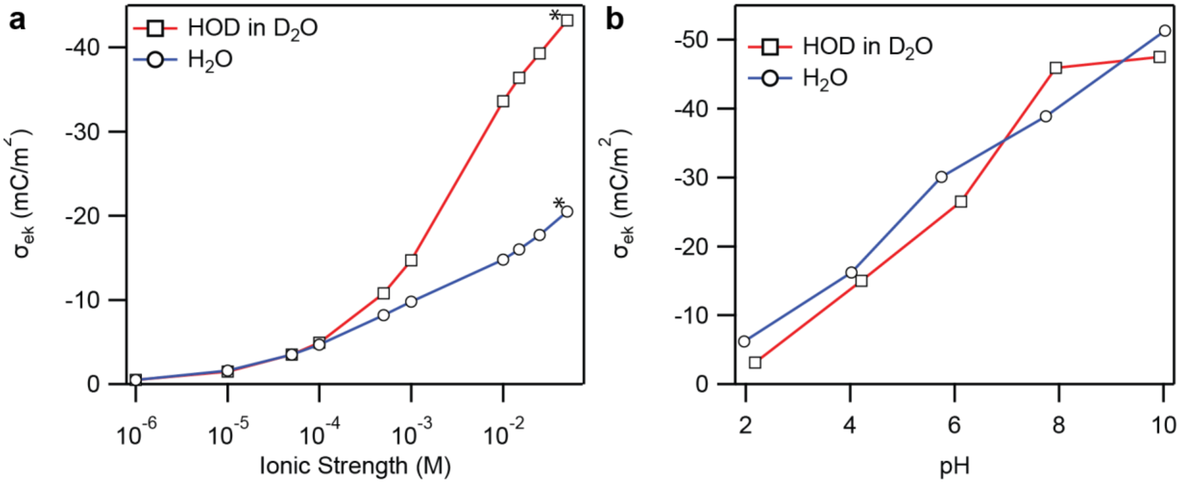

Figure B3: Electrokinetic charge densities computed with the Grahame equation for the silica/H_2O and HOD as a function of (a) ionic strength and (b) pH with a background salt concentration of 50 mM NaCl. The asterisk (*) in (a) indicates the electrokinetic charge density in the presence of 50 mM NaCl, where we observed intrinsic differences in the natural pH. Specifically, we measured a pH of ~7.12 (after the 0.32 adjustment) for HOD with 50 mM NaCl and a pH of ~5.7 for H_2O with 50 mM NaCl. We tentatively attribute this difference to the differences in all the equilibrium constants that influence the pH (Henry's constant of CO_2 in H_2O vs D_2O, formation of carbonic acid in H_2O vs D_2O, K_{a1} and K_{a2} of H_2CO_3 and D_2CO_3).

B4. Error and True Phase from Phase Sensitive vSFG spectra

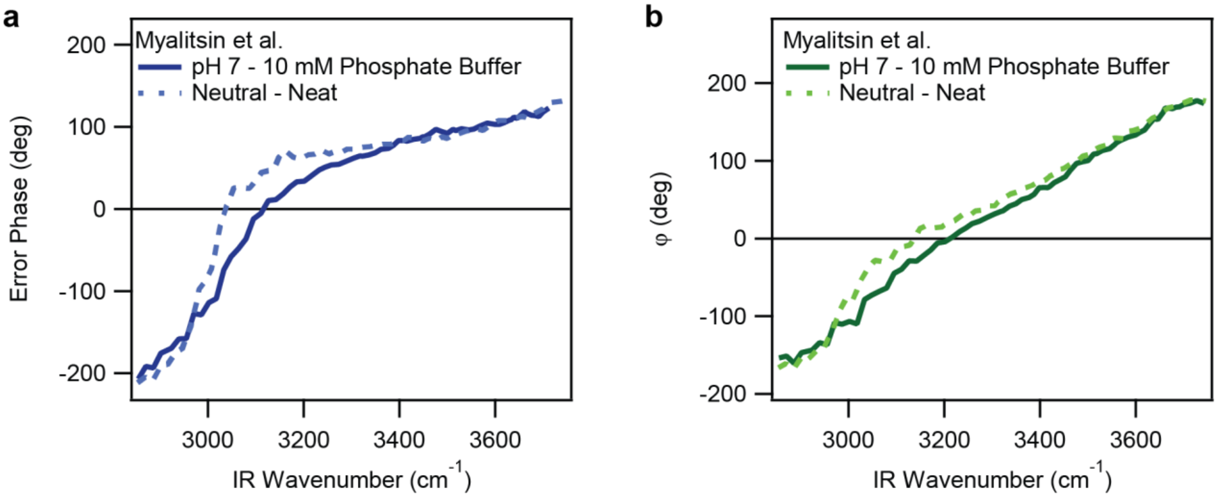

Figure B4: (a) Error and (b) true or absolute phase (φ) derived from the phase sensitive vSFG spectra reported by Myalitsin et al.[78] at natural pH (neat~pH 7.5) and pH 7 (10 mM phosphate buffer solution). The error phase was determined by performing MEM analysis on their corresponding intensity spectra and subtracting the resultant MEM phase from the absolute phase (φ) determined from their complex spectra.

B5. Prediction of the Complex Spectra of HOD Over the Ionic Strength.

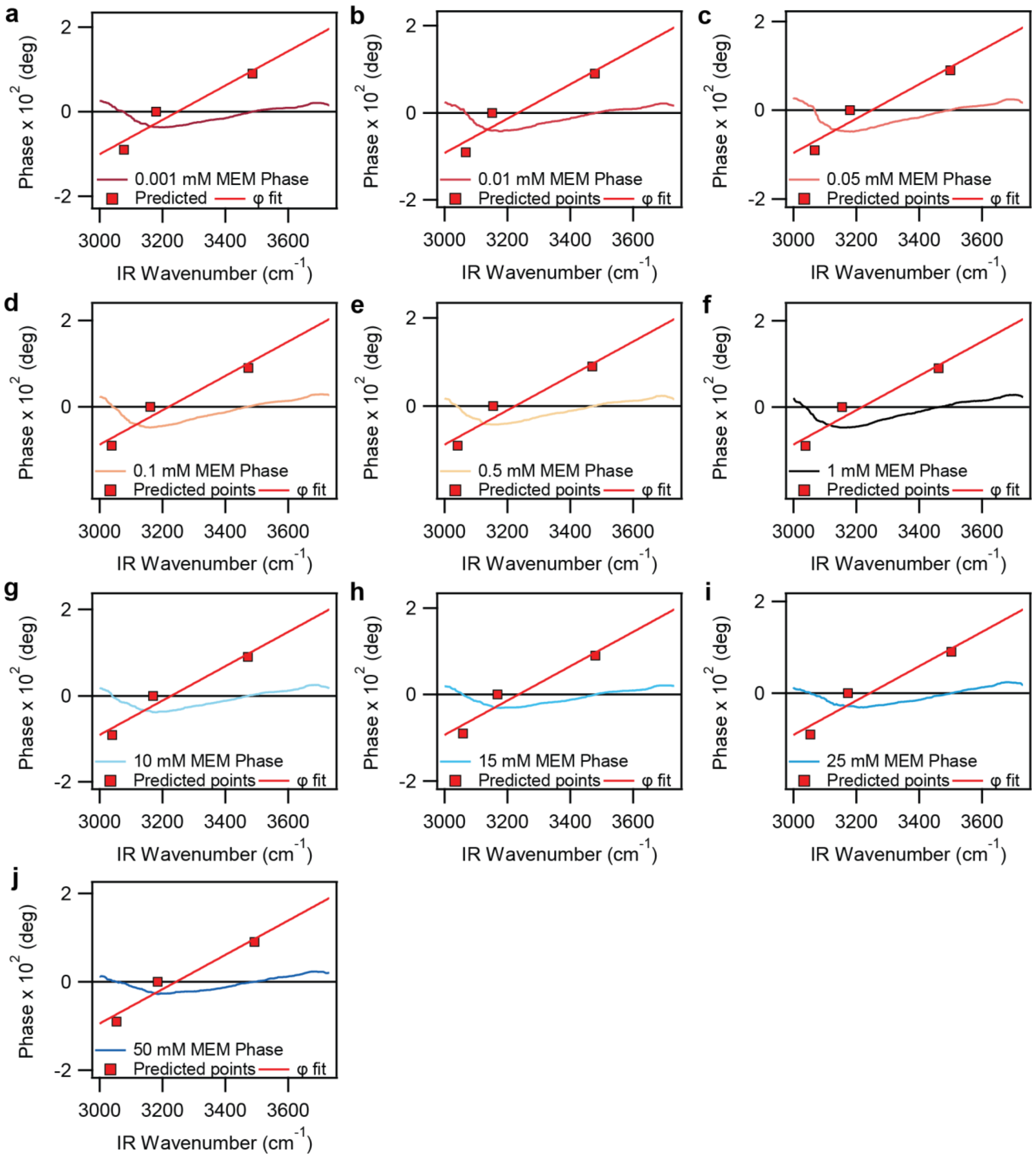

Figure B5: Representative MEM phase and predicted absolute phase over a varied ionic strength range.

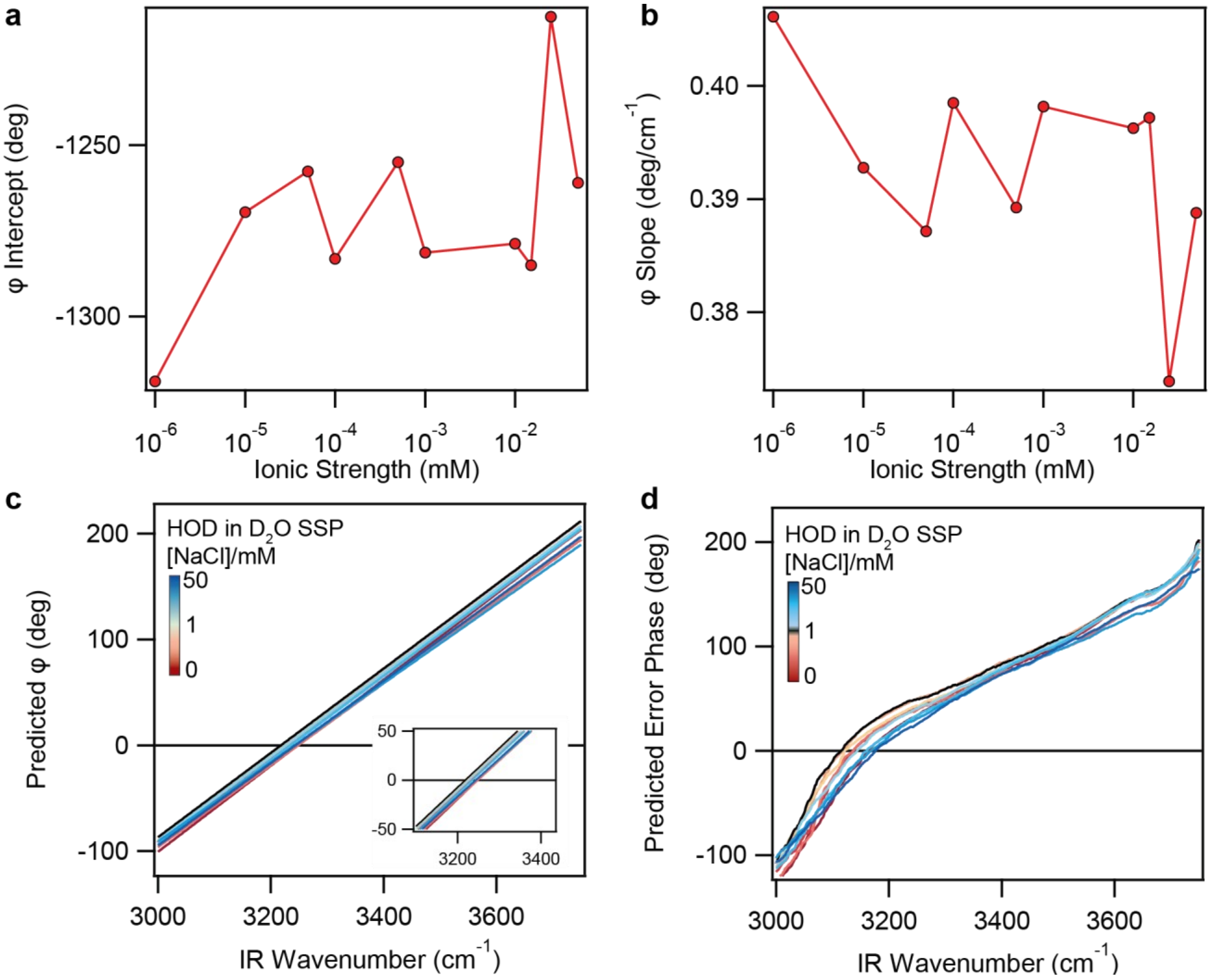

Figure B6: Representative (a) intercept (b) slope (c) predicted absolute phase (φ) (d) error phase over the ionic strength range.

B6. Real Component of HOD Determined by MEM Analysis

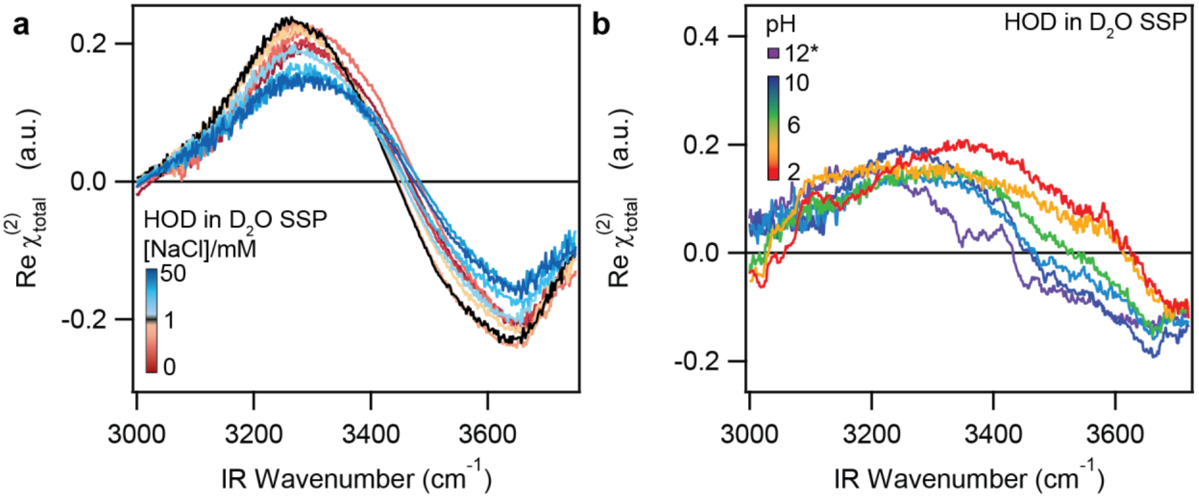

Figure B7: The representative real spectra over the (a) ionic strength and (b) pH ranges covered in this work.

B7. Determination of the Diffuse and Stern Layer Spectra

The g_3 term is determined according to the treatment described by Hore and Tyrode[67], whereby g_3 is defined as

$$g_3 = \int_0^\infty E_0(z)e^{i\Delta kz}dz = \Phi_0 - \frac{4ik_bT\Delta k}{e}\sum_{n=1}^{\infty}\frac{\xi^{2n-1}}{(2n-1)(i\Delta k-\kappa(2n-1))} . \tag{B1}$$

Here $\xi = tanh(\frac{e\Phi_0}{4k_bT})$, and k_b, e, T, κ, Φ_0, Δk are the Boltzmann constant, elementary charge, inverse Debye length, surface potential, and the wavevector mismatch of the sum frequency, visible, and infrared electric fields. In our modified approach,[69,293] we utilize the zeta potential (ζ) determined from electrokinetic measurements in place of Φ_0.

Wen et al.[64] calculated the described the $\chi^{(2)}_{\text{total}}$ as,

$$\chi^{(2)}_{\text{total}} = \chi^{(2)}_s + \chi^{(3)}g_3 . \tag{B2}$$

If $\Delta\chi_s^{(2)} = 0$ for spectra from two adjacent NaCl concentrations, $\chi^{(3)}$ can be determined according to

$$\chi^{(3)} = \Delta\chi_{\text{total}}^{(2)}/\Delta g_3 \,. \tag{B3}$$

We calculated all possible $\chi^{(3)}$ spectra assuming unchanging $\chi_s^{(2)}$ between adjacent salt concentrations. Our final choice of the $\chi^{(3)}$ spectrum was based on the line shape that most closely matched the $\chi^{(3)}g_3$ spectrum reported by Urashima et al.[92], which was found from the different complex spectrum for two adjacent salt concentrations centered at 10 mM NaCl. The $\chi^{(3)}$ spectrum presented is an average from the analysis of two vSFG experiments.

The determined complex $\chi^{(3)}$ spectrum permits the calculation of the $\chi_s^{(2)}$ term by rearranging Equation B2 to yield,

$$\chi_s^{(2)} = \chi_{\text{total}}^{(2)} - \chi^{(3)}g_3 \,. \tag{B4}$$

Since $\chi_{\text{total}}^{(2)}$ is complex in nature, it requires both the real and imaginary components to be known.

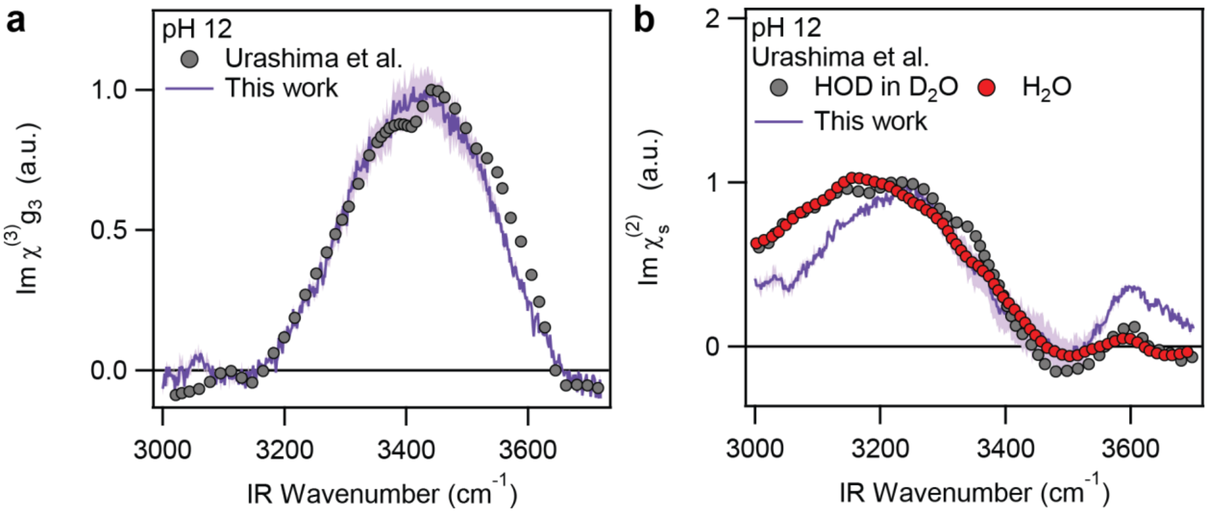

Figure B8: Comparison of the imaginary component of the (a) diffuse and (b) Stern layer resulting from our total complex spectra and our $\chi^{(3)}$ complex spectra at pH 12 compared with the HOD and H_2O spectra reported by Urashima et al.[92]

Appendix C.

Appendix to Chapter 4

C1. pH-Dependent vSFG Measurements and Spectral Fits

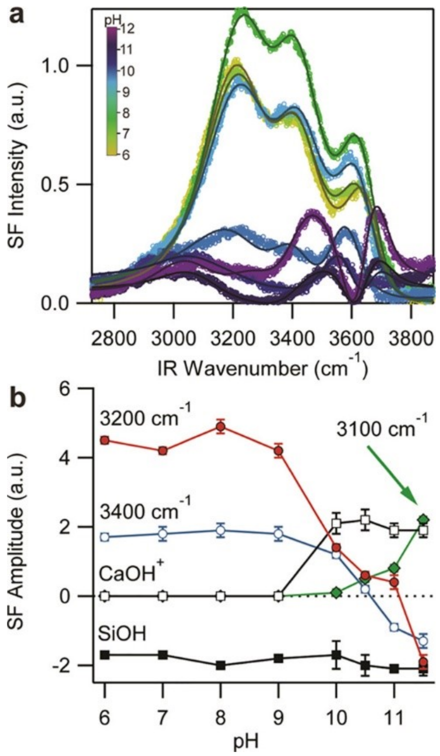

Figure C1: (a) Spectra presented by Rashwan et al.[275] and (b) the corresponding amplitude determined by spectral fitting.

C2. Constant Silica Response Scenarios

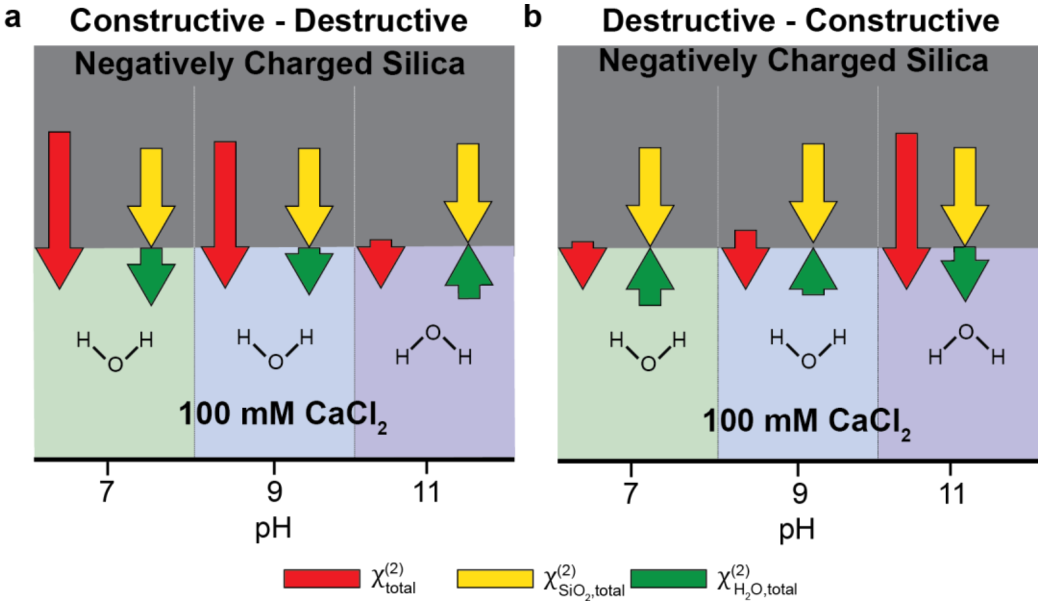

Figure C2: Two scenarios (a) Constructive interference and (b) destructive interference when considering a constant silica contribution in the presence of 100 mM $CaCl_2$ in the aqueous phase. Both scenarios cannot account for the pH-dependent trends observed in the presence of 100 mM $CaCl_2$.

C3. Coordinates for Ground State Geometries for the Models

Ground state geometries utilized for hyperpolarizability computations CAMB3LYP/6-31+G(d,p) in the gas phase. Values are in Å.

Model 1 (Optimized)

Si, 0., 0., 0.
O, 0., 0., 1.64171
O, 1.57614, 0.,-0.45943
H, 2.20391, 0.47421, 0.09465
O, -0.88687, 1.30291,-0.45952
H, -1.26771, 1.29579,-1.3432
O, -0.68923,-1.303, -0.72283
H, -0.1458, -2.08827,-0.84133

Model 2 (Optimized)

Si,0.,0.,0.
O, 0.,0.,1.64956
O, 1.55044,0.,-0.44955
Si,3.01637,-0.23298, 0.25806
O, 3.42192,-1.78604,-0.06775
H, 4.35295,-2.02154,-0.01299
O, 4.18827, 0.71273,-0.38809
H, 4.27819, 1.60402,-0.03641
O, 2.88366, 0.12728, 1.85196
H, 1.98863, 0.08902, 2.22298
O,-0.74758,-1.36583,-0.54449
Si, -2.25453,-1.93528,-0.34416
O,-2.7019, -1.38729, 1.14224
H,-3.63546,-1.36436, 1.37628
O,-3.34879,-1.31746,-1.42144
H,-3.53725,-1.85454,-2.1999
O,-2.29017,-3.55541,-0.55432
H,-1.50389,-4.06838,-0.34069
O,-0.78167, 1.27155,-0.61992
Si,-2.08228, 2.23101,-0.84758
O,-1.68688, 3.67956,-1.50059
H,-1.66642, 3.73803,-2.46093
O,-3.1346,1.5088, -1.87076
H,-3.30041, 0.55586,-1.77291

O,-2.67725, 2.49509, 0.66071
H,-3.29254, 3.22582, 0.77442

Model 3 (Unoptimized)

Si, 0.,0.,0.
O, 0.,0.,1.6226
H, 4.4538, 0., -1.85657
O, -0.53498, 1.40812,-0.69456
O, 2.49613, 1.89136,-1.78452
O, -0.93291,-1.25272,-0.50915
O, 1.55887,-0.18618,-0.46519
O, 3.66467,-0.47005,-2.14832
O, 1.22047,-0.24037,-3.05902
H, -0.66906, 3.03382,-0.84134
Si, 2.23809, 0.27231,-1.88276
H, -0.1255, -0.69354,-3.84457
H, 2.0297,,3.45014,-1.98924
H, -1.9509, -1.61105,-1.7365

C4. Hyperpolarizability Computations

Table C1: Hyperpolarizability parameters (in atomic units) computed with CAM-B3LYP/6-31+G(d,p) in the gas phase for the neutral and anionic species shown in Figure 4.6. The hyperpolarizability ratio of anion/neutral is also given.

	Model 1			**Model 2**			**Model 3**		
	Neutral	**Anion**	**Ratio**	**Neutral**	**Anion**	**Ratio**	**Neutral**	**Anion**	**Ratio**
$\boldsymbol{\beta_{zzz}}$	-18	-277	15	-39	-228	6	-408	-2027	5
$\boldsymbol{\beta_{tot}}$	0.04	2569	64225	151	2130	14	2720	39813	15
$\boldsymbol{\beta}_{\|\|}$	0.01	514	51400	30	426	14	544	7963	15